

AD-A279 012



NEOSR-TR- 94 0267

Approved for public release;
distribution unlimited.

2

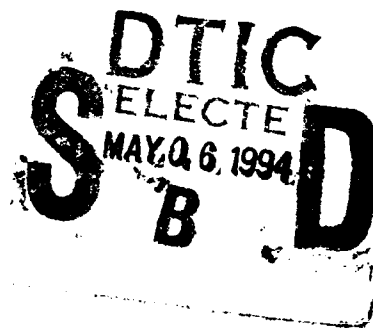
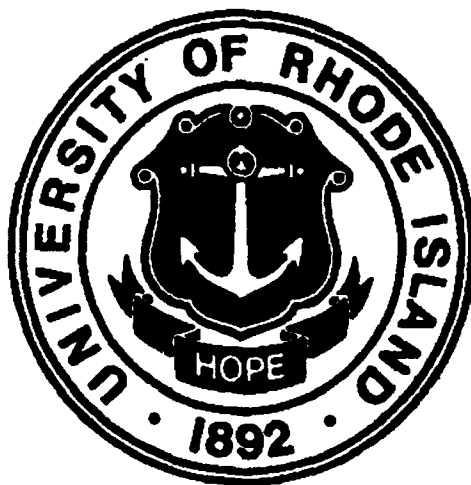
**STUDIES OF THE EFFECT OF MICROSTRUCTURE ON THE
DYNAMIC BEHAVIOR OF GRANULAR AND PARTICULATE MEDIA**

(FIRST YEAR REPORT)

by

Arun Shukla and Martin H. Sadd

**Prepared for U.S. Air Force Office of Scientific Research
Under Contract No. F49620-93-1-0209
Bolling Air Force Base**



**Department of Mechanical Engineering & Applied Mechanics
University of Rhode Island
Kingston, RI 02881**

March 1994

94-13584



DTIC QUALITY INSPECTED 1

94 0 05 062

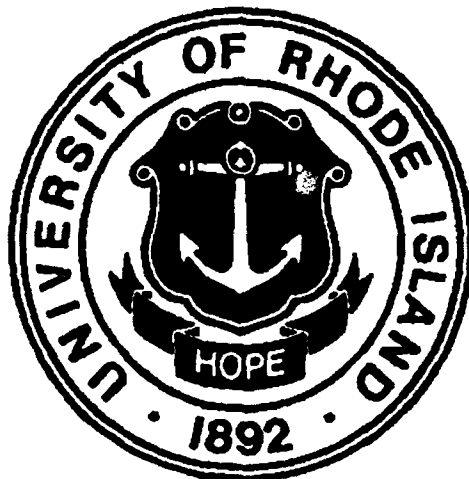
**STUDIES OF THE EFFECT OF MICROSTRUCTURE ON THE
DYNAMIC BEHAVIOR OF GRANULAR AND PARTICULATE MEDIA**

(FIRST YEAR REPORT)

by

Arun Shukla and Martin H. Sadd

**Prepared for U.S. Air Force Office of Scientific Research
Under Contract No. F49620-93-1-0209
Bolling Air Force Base**



**Department of Mechanical Engineering & Applied Mechanics
University of Rhode Island
Kingston, RI 02881**

March 1994

The views and conclusions contained in this document are those of the authors and should not be interpreted as necessarily representing the official policies or endorsements, either expressed or implied, of the Air Force Office of Scientific Research or the U.S. Government.

REPORT DOCUMENTATION PAGE			Form Approved OMB No. 0704-0188	
Public reporting burden for this collection of information is estimated to average 1 hour per response, including the time for reviewing instructions, searching existing data sources, gathering and maintaining the data needed, and completing and reviewing the collection of information. Send comments regarding this burden estimate or any other aspect of this collection of information, including suggestions for reducing this burden, to Washington Headquarters Services, Directorate for Information Operations and Reports, 1215 Jefferson Davis Highway, Suite 1204, Arlington, VA 22202-4302, and to the Office of Management and Budget, Paperwork Reduction Project (0704-0188), Washington, DC 20503.				
1. AGENCY USE ONLY (Leave blank)		2. REPORT DATE March 1994	3. REPORT TYPE AND DATES COVERED Annual, March 93 to February 94	
4. TITLE AND SUBTITLE Studies of the Effect of Microstructure on the Dynamic Behavior of Granular and Particulate Materials			5. FUNDING NUMBERS F49620-93-1-0209 2302/C.S	
6. AUTHOR(S) Arun Shukla Martin H. Sadd				
7. PERFORMING ORGANIZATION NAME(S) AND ADDRESS(ES) Department of Mechanical Engineering & Applied Mechanics University of Rhode Island Kingston, RI 02881			8. PERFORMING ORGANIZATION REPORT NUMBER AEOSR-TR- 94 0267 AEOSR-TR- 94 0267	
9. SPONSORING/MONITORING AGENCY NAME(S) AND ADDRESS(ES) Air Force Office of Scientific Research Particulate Mechanics Program Bolling Air Force Base Washington, DC 20332			10. SPONSORING/MONITORING AGENCY REPORT NUMBER F49620-93 - 1-0209	
11. SUPPLEMENTARY NOTES				
12a. DISTRIBUTION/AVAILABILITY STATEMENT Approved for Public Release: Distribution is unlimited			12b. DISTRIBUTION CODE	
13. ABSTRACT (Maximum 200 words) A combined experimental-numerical investigation is being conducted to study dynamic load transfer in particulate materials due to explosive loadings. The primary emphasis in the study is to relate the microstructural features of the particulate media to the load transfer process. The experimental technique of dynamic photoelasticity is used to investigate the effect of cementation and of the particle shape on the local contact stress fields. The stiffness of the cement relative to that of the particle controls the location of the peak contact stresses. Strong cementation increases the load transfer velocity and also promotes fracture of the particles. The particle shapes as presently studied in this research program seem to have little influence on the load transfer process. The applicability of the fiber optic sensors and the speckle techniques to contact stress measurements is evaluated. Fiber optic sensors show promise of future applications to three dimensional problems. Discrete element numerical wave simulation has been conducted for saturated granular materials through the introduction of a new contact law using elastohydrodynamic theory. Pore fluid acts to decrease the wave speed and increase the attenuation. Future numerical studies will focus on additional changes of the interparticle contact response through cementation and particle shape effects.				
14. SUBJECT TERMS Wave propagation, dynamic contact load, dynamic photoelasticity, fiber optic sensor, speckle photography, discrete element method, wave velocity, explosive loading			15. NUMBER OF PAGES 151	
			16. PRICE CODE	
17. SECURITY CLASSIFICATION OF REPORT Unclassified	18. SECURITY CLASSIFICATION OF THIS PAGE Unclassified	19. SECURITY CLASSIFICATION OF ABSTRACT Unclassified	20. LIMITATION OF ABSTRACT SAR	

Table of Contents

	Page
Acknowledgement	iii
Abstract	iv
Statement of Work	1
Status of the Research Effort	1
1. The Relationship of Granular Fabric with Wave Propagational Behaviors	2
2. Evaluation of a Fiber Optic Sensor for Strain Measurement and Preliminary Applications to Contact Mechanics	31
3. Application of White Light Speckle Photography to Measure Rigid Body Displacements and Deformations	60
4. Preliminary Study of the Effect of Cementation on the Dynamic Load Transfer Phenomenon	72
5. Hybrid Theoretical/Experimental Determination of Contact Loadings Between Cemented Disk Particles	94
6. Preliminary Studies of Dynamic Load Transfer Through Saturated Granular Media	107
7. Influence of Particle Shape on the Dynamic Load Transfer Process	124
Bibliography	145
Professional Personnel Associated with the Project	148
Technical Publications	149
Interactions (Coupling Activities)	150

Accession For	
NTIS GRA&I	<input checked="" type="checkbox"/>
DTIC TAB	<input type="checkbox"/>
Unannounced	<input type="checkbox"/>
Justification	
By	
Distribution/	
Availability Codes	
Dist	Avail and/or Special

Acknowledgement

The authors would like to acknowledge the support of the Air Force Office of Scientific Research, Bolling Air Force Base, Washington D.C., under grant No. F49620-93-1-0209 and Major Martin Lewis for his support and encouragement.

The efforts of the graduate students Mr. Harry Zervas, Dr. Q. M. Tai, Mr. Y. Zhu, Mr. R. P. Singh, Mr. A. Gautam, Mr. Z. Zhang, Mr. V. Subramaniam, and Mr. F. Sienkiewicz in conducting this research are greatly acknowledged.

The authors would also like to thank our electronics technician, Mr. Ray McLaughlin, and our machinist, Mr. Kevin Donovan for their valuable assistance in this project.

The support of the College of Engineering and the Engineering Computer Lab is also acknowledged.

Abstract

A combined experimental-numerical investigation is being conducted to study dynamic load transfer in particulate materials due to explosive loadings. The primary emphasis in the study is to relate the microstructural features of the particulate media to the load transfer process. The experimental technique of dynamic photoelasticity is used to investigate the effect of cementation and of the particle shape on the local contact stress fields. The stiffness of the cement relative to that of the particle controls the location of the peak contact stresses. Strong cementation increases the load transfer velocity and also promotes fracture of the particles. The particle shapes as presently studied in this research program seem to have little influence on the load transfer process. The applicability of the fiber optic sensors and the speckle techniques to contact stress measurements is evaluated. Fiber optic sensors show promise of future applications to three dimensional problems. Discrete element numerical wave simulation has been conducted for saturated granular materials through the introduction of a new contact law using elastohydrodynamic theory. Pore fluid acts to decrease the wave speed and increase the attenuation. Future numerical studies will focus on additional changes of the interparticle contact response through cementation and particle shape effects.

Statement of Work

The primary objective of this investigation is to study the role of microstructure on the dynamic behaviour of a variety of particulate materials. In particular, attention is directed towards relating microstructural features including packing fabric, contact behaviors, and particle shape and size, to wave propagation characteristics of wave speed, amplitude attenuation, and dispersion.

Status of the Research Effort

In the past year we initiated several different studies and these include: (1) Relating granular fabric to wave propagational behaviours, (2) Evaluating fiber optic sensor and applying it to contact strain measurement, (3) Applying white light speckle photography to displacement measurements, (4) Studying the effect of cementation on the load transfer phenomenon, (6) Looking at the influence of particle shape on the wave propagation process. The details of these efforts are presented in the following chapters.

CHAPTER 1

THE RELATIONSHIP OF GRANULAR FABRIC WITH WAVE PROPAGATIONAL BEHAVIORS

1.1 Introduction

Because wave propagation in granular materials is locally transmitted through and across contact regions between adjacent particles, material microstructure or fabric will be related to the propagational characteristics of wave speed and amplitude attenuation. Fabric of granular materials can be described as the spatial arrangement of the solid particles and associated voids. Over the past several years, many fabric measures have been proposed for granular media, but no unique choice of fabric description has been universally accepted which can adequately describe the mechanical response of such media.

Some research has categorized fabric into two types: *orientation fabric* (orientation of individual particles) and *packing fabric* (mutual relation of individual particles to the others). Orientation fabric may be quantitatively defined by a vector mean direction and a vector magnitude to characterize orientation of non-spherical or non-circular particles. This fabric measure is commonly represented by an angular measure (with respect to a reference direction) of the long axes of individual particles. Packing fabric measures have included *branch vectors*, *normal contact vectors*, *coordination or contact numbers*, *void characteristics*, etc. Examples of these fabric measures are illustrated schematically in Fig. 1.1. Some of these fabric measures are *kinematical* in nature, determined primarily by the particle shape and packing geometry. Other measures such as those related to the contact conditions are *kinetic*, and are determined by the particle material and shape properties and also by the contact surface conditions.

Fig. 1.2 shows a photograph of the dynamic photoelastic fringe patterns associated with an actual wave moving through a model particulate medium containing some of these

fabric structures. It has been observed for both static and dynamic loading conditions that particulate materials transmit mechanical loadings along a series of complex discrete paths. These discrete paths are established, in relation to the loading direction, by many of the microstructural variables mentioned, and therefore local wave propagation is determined by granular fabric through the creation of local wave guides.

This section outlines our research which examines the relationship of granular fabric with the wave propagational variables. The model granular materials under study will be large random assemblies of circular particles which have been created using one or more of our random media generator codes. This study focussed primarily on the effects of packing fabric, including *branch vector distributions* (which for circular particles coincide with normal contact vectors), *path fabric*, and *void polygon fabric*.

1.2 Branch Vector Fabric

Branch vectors have been used as fabric measures in several previous static investigations of granular media, and this measure also looks appropriate for wave propagation problems since dynamic loads are transmitted primarily through contact points which lie along branch vectors. Thus it seems reasonable to assume that branch vector distributions could be related to the wave propagational behaviors in such media.

To investigate such relationships, several of the large random assembly generators previously discussed in an earlier AFOSR report (Shukla and Sadd, 1992) were used to construct six assemblies with different microstructures. These assemblies are named as S-1, M-1, M-2, W-1, W-2, and W-3. Shown in Fig. 1.3, assembly S-1 was generated by the strongly anisotropic generator. Assemblies M-1 and M-2, displayed in Figs. 1.4 and 1.5, were constructed by the moderately anisotropic generator. Finally, the weakly anisotropic generator was used to construct assemblies W-1, W-2, and W-3, and they are shown in Figs 1.6 - 1.8. The total numbers of particles for each of the six assemblies are listed in Table 1.1. The void ratio (volume of void / volume of particle) and average coordination

number \bar{N} (average contact number per particle) are also calculated and are given in Table 1.1 for the six assemblies. Assemblies S-1 has the highest void ratio of 0.43 and lowest coordinate number of 2.87, while W-3 has the lowest void ratio of 0.22 and the highest coordinate number of 4.30.

The branch vectors of these assemblies were then calculated and normalized to construct unit vectors. To find a load preferred direction, the x-component b_x and y-component b_y of each branch vector b were determined and summed over the entire assembly. Denoting F^b as the ratio of the summed y-components over the x-components gives

$$F^b = \frac{\sum |n_y|}{\sum |n_x|}. \quad (1.1)$$

The values of F^b for the six assemblies are listed in Table 1.1. The branch vector angular distributions (rose diagrams) of the six assemblies are shown in Figs. 1.9 - 1.14. For assembly S-1 (see Fig. 1.9), all branch vectors are concentrated in the region defined by approximately $\pm 30^\circ$ from the vertical direction. No branch vector is found along the horizontal direction, and F^b is 2.06 for this assembly. The branch vector distributions for M-1 and M-2 are shown in Fig. 1.10 and Fig. 1.11, respectively. The branch vectors lie mainly in vertical and horizontal directions with preference in vertical direction, and both assemblies have the same F^b ratio of 1.19. Figs. 1.12 - 1.14 show the branch vector distributions for assemblies W-1, W-2, and W-3. The weakly anisotropic assemblies do not show any significant preferred branch vector distributions. The F^b ratios for these cases are 1.01, 0.9, and 1.01, respectively. Using the discrete element method with a nonlinear hysteretic contact law, our wave propagation code **WAPRIPM** (Wave Propagation in Particulate Media) was used to simulate the wave propagational behaviors (wave speed and amplitude attenuation) in the six assemblies under study. The simulations involved the comparison of the propagation of plane type waves moving along

orthogonal directions (horizontal and vertical) in the generated assemblies. The transient input loading was modeled using a triangular pulse with a peak value of 1000 N and a period of 60 μ s. To represent a planar input wave, the time-dependent pulses were simultaneously applied to particles along one of the horizontal or vertical boundaries of the assemblies under study. To calculate the transmitted or output wave pulse, an imaginary horizontal or vertical line was drawn near the boundary opposite to where the input loadings were applied. If a branch vector of a pair of particles in contact or potential contact is intercepted by this imaginary line, the normal contact load component perpendicular to the imaginary line, i.e. either F_x or F_y , was recorded. In this fashion, the contribution of the individual particle contacts could be determined, and these recorded loads were then summed and normalized with respect to the sum of the peak values of the input loadings. These normalized contact loads are given by

$$\begin{aligned} F_{xx}(t) &= \frac{\sum F_x(t)}{\sum F_{peak,input}} \\ F_{yy}(t) &= \frac{\sum F_y(t)}{\sum F_{peak,input}} \end{aligned} \quad (1.2)$$

where the summation in the numerator is over the number of branch vectors intercepted by the imaginary line, while the summation in the denominator is over the number of input loadings.

Fig. 1.15 shows this wave propagation simulation for the media model S-1. The normalized normal contact load component profiles $F_{xx}(t)$ and $F_{yy}(t)$ correspond to vertical and horizontal input loadings respectively, and the ratios of the peak values of the profiles, denoted by

$$F_{yx} = \frac{(F_{yy}(t))_{peak}}{(F_{xx}(t))_{peak}}, \quad (1.3)$$

are given in Table 1.1.

For assembly S-1, F_{yx} is 200.68. It is obvious that a wave propagating along the vertical direction has much less attenuation than one traveling along the horizontal direction. Also note that the wave speed as determined by the arrival time of the averaged profile is different for the two propagational directions, and the ratio of vertical wave speed over horizontal wave speed is approximately 3. Note that results for the horizontal wave are not visible because of the scale used in Fig. 1.15. These results follow qualitatively from the local branch vector distribution diagram in Fig. 1.9. Since most branch vectors lie along the vertical direction, the load transfer paths in that direction are rather continuous and straight, while just the opposite would be true for load transfer paths along the horizontal direction. Therefore, assembly S-1 is an anisotropic medium, and demonstrates high directionally dependent wave propagation.

The normalized normal contact load profiles for model assemblies M-1 and M-2 are shown in Figs. 1.16 and 1.17. For these assemblies, the discrete element simulations indicate that the vertical wave attenuation is still smaller than horizontal wave, but these differences are not as pronounced as in assembly S-1. The wave traveling along vertical direction was faster than the horizontal wave, but differences between the two wave velocities is not as large as that for the S-1 assembly. Therefore, the degree of anisotropy is larger in assembly S-1 than in M-1 or M-2, which agrees with their respective F^b values. However, the F^b ratio fails to correlate with the anisotropic wave propagational behaviors of assemblies M-1 and M-2. The ratios of the peak values of the profiles F_{peak} are 33.33 and 100.02 for M-1 and M-2, respectively, and the ratio of vertical wave speed to horizontal wave speed for M-2 (1.60) is greater than that for M-1 (1.52). All of these results indicate that assembly M-2 has higher wave propagational anisotropy, but unfortunately the fabric measure F^b of M-2 has the same value as M-1. The vertical wave profile in Fig. 1.17 has a small precursor pulse before the main profile. The reason for this is that the anisotropy within whole assembly is not uniform, and a small portion of the

total wave will propagate along short paths and will thus arrive slightly ahead of the main signal. The simulation results for the weakly anisotropic assemblies are shown in Figs. 1.18 - 1.20. The F_{yx} ratios for these assemblies are much smaller than for assemblies M-1 and M-2. They are 1.76 for W-1, 0.94 for W-2, and 1.23 for W-3. Compared with the S- and M-assemblies previously discussed, differences between vertical and horizontal wave speeds are relatively small for the W-assemblies. This agrees with the local branch vector distribution diagrams which show that the W-assemblies are weakly anisotropic. Again, the ratio F^b fails to provide a correlation with fabric and wave behaviors for the W-assemblies.

1.3 Path Fabric

When waves propagate through granular media, the local or micro-dynamic loads are never uniformly transmitted across a sample, but rather are transferred through specific chains of particles linked through contact. Fig. 1.21 illustrates the contact load distribution (the thickness of the lines scaled to the current maximum force) in a particle bed due to particle impact at the top (Thornton and Randall, 1988). Between these special chains, particles may carry little or no load. It appears that, by chance, some sequences of particles offer contiguous paths through the assembly that are straighter than other possible paths. It is these paths that carry most of the load transfer rather than their more tortuous neighbors. Thus, within an assembly, if in one direction there are more contiguous and straight paths than in other directions, the wave should propagate more easily in the former direction. This section describes a study of this path fabric effect on wave propagation.

A path is defined as a set of continuous branch vectors of particles in contact, and it was observed experimentally by Shukla et.al. (1988) that dynamic load can be transferred along the path only when every pair of neighboring branch vectors b_i and b_j in the path satisfy the relationship

$$b_i \cdot b_j > 0, \quad (1.4)$$

which means that the *branch angle* φ shown in Fig. 1.22 is less than 90° . Therefore, a *transferable* or *propagator* load path can be defined as a series of particles which are in contact with each other, such that the dot product of any pair of neighboring branch vectors is positive.

Within this section, two different methods of constructing a path fabric measure, based on the straightness of the path, will be discussed. In one method, the dot products of all adjacent branch vectors in a given path are calculated, and they are used as basic units to build a path fabric measure. For example, a path fabric between two arbitrary particles can be expressed as

$$F^p = \sum \frac{1}{\sum \frac{1}{b_i \cdot b_j}}, \quad (1.5)$$

where inner summation is over a path connecting the particles and outer summation is over all of the possible paths. For the straight chain case, there exists only one path between the two particles, and equation (1.5) gives $F^p = \frac{1}{N-1}$, where N is the total number of particles in the path. On the other hand, if there is only a single path between two particles in a two dimensional assembly, and if any branch angle in this path equals 90° , equation (1.5) gives $F^p = 0$. The path will thus become a *non-propagator* if $b_i \cdot b_j \leq 0$, and in the following sections, only propagator paths will be included in the investigation.

A second method to build a path fabric measure uses x and y branch vector components instead of the dot product used in equation (1.5). One fabric measure between two points can be written as

$$F_x^p = \frac{\sum \sum |b_i|_x}{\sum \sum 1} \quad (1.6)$$

$$F_y^p = \frac{\sum \sum |b_i|_y}{\sum \sum 1}$$

where outer summations are over all possible paths between the two points, and inner summations are over individual paths. Equations (1.6)₁ and (1.6)₂ are used to describe the path fabric along the x and y directions, respectively. For granular media simulated by circular disks of the same size, the value of equations (1.6)₁ and (1.6)₂ will not be larger than the disk diameter, and will equal to the diameter only when the path is a straight chain along the x or y direction.

Using the first proposed path fabric measure to analyze the microstructure of an assembly, it is required to find every path between each pair of boundary particles, of which the input loading is applied at one and output contact load is recorded at the other. Since two paths are defined as different if one path includes any particle the other does not, the number of the paths across an assembly will be very large. Theoretically, all different paths can be found and $\sum \frac{1}{b_i \cdot b_j}$ can be calculated for each path. However, for large assemblies the total number of paths between two boundary points approach 10^7 - 10^8 , and considerable CPU time and large memory space will be needed to account for each path. For example, to calculate the path fabric measure F^p between two points which lie on opposite boundaries of assembly W-1, takes more than 1 hour of CPU time (VAXstation 3100). Therefore it appears impractical to use equation 1.5).

One solution to this problem is to divide the whole assembly into several subregions and use the fabric measure of equation (1.6). Using this scheme a general assembly

can be divided into subparts, and Fig. 1.23 shows four such subregions for the calculation of vertical paths. In this figure, dots stand for the contact points, and the solid polygon line represents one of many paths, which start at point A', go through points B', C', and D', and end at point E'. Equation (1.6) for the vertical paths from A' to E' can be written as

$$\begin{aligned} F_x^p &= \frac{\sum [\overline{A'E'}]_x}{\sum \sum 1} \\ F_y^p &= \frac{\sum [\overline{A'E'}]_y}{\sum \sum 1} \end{aligned} \quad (1.7)$$

where $[\overline{A'E'}]$ is the vector from A' to E'. The summation in the numerator is over all possible paths from A' to E'. The equation can be further rewritten as

$$\begin{aligned} F_x^p &= \frac{N_{path-A'E'}}{\sum_{path-A'E'} N_{particle}} [\overline{A'E'}]_x \\ F_y^p &= \frac{N_{path-A'E'}}{\sum_{path-A'E'} N_{particle}} [\overline{A'E'}]_y \end{aligned} \quad (1.8)$$

where $N_{path-A'E'}$ is the total number of paths between A' and E', and $N_{particle}$ is the total number of particles along a path. If the paths are restricted through points B', C', and D', the total number of paths is given by

$$N_{path-A'E'} = N_{path-A'B'} \cdot N_{path-B'C'} \cdot N_{path-C'D'} \cdot N_{path-D'E'}, \quad (1.9)$$

and the total number of particles equals

$$\begin{aligned}
N_{particle-A'E'} = & \left(\sum_{path-A'B'} N_{particle} \right) \cdot N_{path-B'C'} \cdot N_{path-C'D'} \cdot N_{path-D'E'} \\
& + \left(\sum_{path-B'C'} N_{particle} \right) \cdot N_{path-A'B'} \cdot N_{path-C'D'} \cdot N_{path-D'E'} \\
& + \left(\sum_{path-C'D'} N_{particle} \right) \cdot N_{path-A'B'} \cdot N_{path-B'C'} \cdot N_{path-D'E'} \\
& + \left(\sum_{path-D'E'} N_{particle} \right) \cdot N_{path-A'B'} \cdot N_{path-B'C'} \cdot N_{path-C'D'}
\end{aligned} \tag{1.10}$$

In Fig. 1.23, taking the bottom subregion as an example, all vertical paths from A' to B' can be found, and the particle numbers of all the paths are summed. The above procedure is repeated for the other three regions, and equation (1.8)₂ gives the path fabric measure for all the paths between A' and E' which pass through B', C', and D'. Now let B' take all points on level B-B, C' take all points on level C - C, and D' take all points on level D - D, then equation (1.8)₂ gives the fabric measure for all paths from A' to E'. The path fabric measure for the whole assembly can then be obtained by summing the values given by equation (1.8)₂ for all the paths between boundaries A- A and E - E. Similarly, the horizontal value can be calculated from equation (1.8)₁. It should be pointed out that when a vertical path is under consideration, the path will be discarded if it runs beyond a vertical zone of fixed width centered at the initiating particle within a subregion. This is reasonable since a highly zigzagged path will transmit negligible load, and by discarding these paths a reduction of computational effort will result.

Using equation (1.8), the vertical and horizontal path fabrics are computed for the six assemblies discussed in the previous section. The ratios of the summation of vertical fabric to the summation of horizontal fabric

$$F^P = \frac{\sum_{vertical} F_y^P}{\sum_{horizontal} F_x^P} \tag{1.11}$$

are given in table 1.1. For the strongly anisotropic assembly S-1, there is no contiguous path along horizontal direction and this gives a ratio of infinity, which correlates with the discrete element results which show that the horizontal wave is almost blocked. The F^p ratio has the values of 5.88 and 2.08 for the two moderately anisotropic assemblies M-1 and M-2. Thus, there are more paths along the vertical direction rather than the horizontal direction, and waves prefer to propagate along the vertical direction in these assemblies as predicted by discrete element analysis. However, as with the branch vector case, the path fabric also fails to indicate the stronger anisotropy of assembly M-2 over M-1. The reason for this lack of correlation may be due to gap closing, which can change the path fabric significantly. Taking assembly M-2 as an example, during the process of vertical wave propagation, it appears that more than 40 new contacts have been created. The F^p ratios of the weakly anisotropic assemblies W-1, W-2, and W-3 are 0.95, 1.00, and 1.16, respectively, which indicates that these assemblies are indeed weakly anisotropic. However, the F^p ratio fails to provide a correlation with path fabric and wave behaviors for the W-assemblies.

1.4 Void Polygon Vector Fabric

In the previous two sections, fabric measures associated with particles were discussed. However, besides the solid particle phase, a granular material also consists of a void phase, and thus it would seem reasonable that a fabric measure based on voids could be useful to correlate with wave propagation.

To describe a void with N curved segments, a polygon is used as shown in Fig. 1.24. The polygon consists of the branch vectors linking the particles around a void, and thus a *void polygon* represents the relations of this special group branch vectors. Assuming that a void surrounded by N particles has N branch vectors b_1, b_2, \dots, b_N , a tensor can be defined (similar to Konishi and Naruse, 1988) as

$$p_{ij} = \sum_{k=1}^N b_{ki} b_{kj} \quad (1.12)$$

where b_{ki} and b_{kj} are x and y components of b_k respectively. The principal values of p_{ij} are

$$p_1, p_2 = \frac{1}{2} \sum_{k=1}^N b_k^2 \pm \sqrt{\left(\sum_{k=1}^N b_k^2 \cos 2\theta_k \right)^2 + \left(\sum_{k=1}^N b_k^2 \sin 2\theta_k \right)^2} \quad (1.13)$$

The difference between the principal values is denoted by

$$H = p_1 - p_2 \quad (1.14)$$

and the major principal direction is calculated as

$$\theta_p = \frac{1}{2} \arctan \left(\frac{\sum_{k=1}^N b_k^2 \sin 2\theta_k}{\sum_{k=1}^N b_k^2 \cos 2\theta_k} \right) \quad (1.15)$$

Now the void can be described by p_1, p_2 , and θ_p : $H = p_1 - p_2$ is related to the anisotropy of the void, $S = p_1 p_2$ represents the void area, and θ_p gives the void direction.

Konishi and Naruse (1988) constructed a *local void vector* \mathbf{p} whose value is H and direction is given by θ_p . In this study, the local void vector \mathbf{p} is defined as a vector whose magnitude is HS . The reason for including S in the void vector definition is that when waves propagate through a granular material, the possibility of voids and gaps closing is related to void size. The void vector direction will also use the measure θ_p . Therefore, voids within a granular mass can be found and the void vectors may be constructed for each of them.

Using this scheme of local void vectors, a rose diagram similar to the branch vector plots in Figs. 1.9 - 1.14 can be plotted. Figs. 1.25 - 1.30 show void vector distributions for the six assemblies discussed in the previous sections. An examination of these plots along with the corresponding branch vector diagrams reveals that void vector reflects the microstructure more clearly than branch vectors. In the void vector

distribution diagram for assembly S-1, all the void vectors lie in vertical direction to block horizontal wave paths, while the corresponding branch vector diagram fails to demonstrate this. For assemblies M-1 and M-2, void vector rose diagrams show an overwhelming majority of void vectors lying in the vertical direction. This agrees with the numerical simulations, while the corresponding branch vector diagrams only show slightly more branch vectors in vertical direction than in the horizontal. The void vector rose diagrams for the W-assemblies also indicate preferred wave propagation directions, which was not apparent in the branch vector diagrams.

The summation of all void vector x and y components can be given by $\sum p_x$ and $\sum p_y$, respectively, and thus we can define a ratio

$$F^v = \frac{\sum p_y}{\sum p_x} \quad (1.16)$$

which can be used to measure the anisotropy of a medium. The values of F^v for the six assemblies are given in Table 1.1. This ratio increases with the degree of assembly anisotropy except for assemblies W-2 and W-3, and it obtains a maximum value of 85.08 in assembly S-1, indicating a strongly anisotropic medium. For moderately anisotropic assemblies M-1 and M-2, the ratio decreases to 2.44 and 2.55 respectively, which successfully predicts a stronger anisotropy for assembly M-2 over M-1. The values of F^v for the weakly anisotropic assemblies W-1, W-2 and W-3 are 1.12, 1.05, and 1.00, respectively. F^v correctly indicates that the degrees of anisotropy in W-2 and W-3 are weaker than in W-1, but as with the other fabric measures it fails to point out W-3 has the smallest degree of anisotropy among the W-assemblies. Thus, it can be concluded that the void fabric measure correlates with the wave propagational behaviors of particulate materials better than the branch vector or/and path fabric schemes discussed in the previous sections.

Assembly	Particle Number	Void Ratio	\bar{N}	F_{yz}	F^b	F^p	F^v
S - 1	822	0.43	2.87	200.68	2.06	no x-path	85.08
M - 1	778	0.28	3.43	33.33	1.19	5.88	2.44
M - 2	854	0.28	3.41	100.02	1.19	2.08	2.58
W - 1	1042	0.25	4.17	1.76	1.01	0.95	1.12
W - 2	1296	0.25	4.04	0.94	0.99	1.00	1.05
W - 3	1338	0.22	4.30	1.23	1.01	1.16	1.00

Table 1.1 Various Fabric Measures with Density and Coordinate Number for Six Assemblies

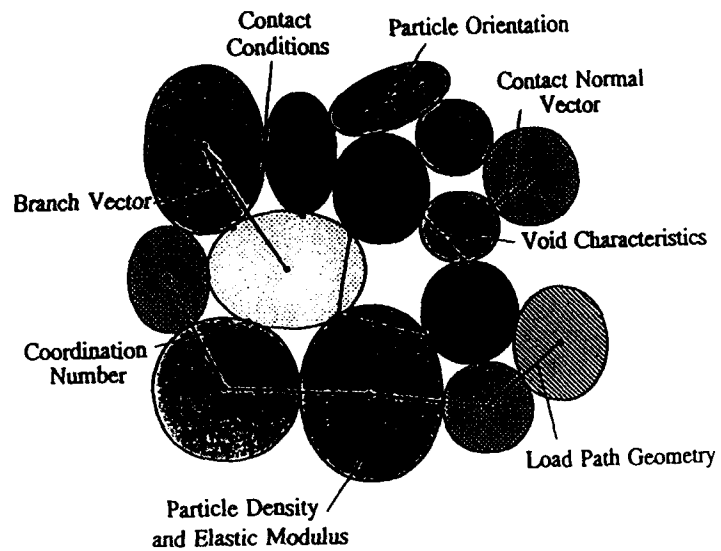


Fig. 1.1 Common Fabric Measures for Granular Materials

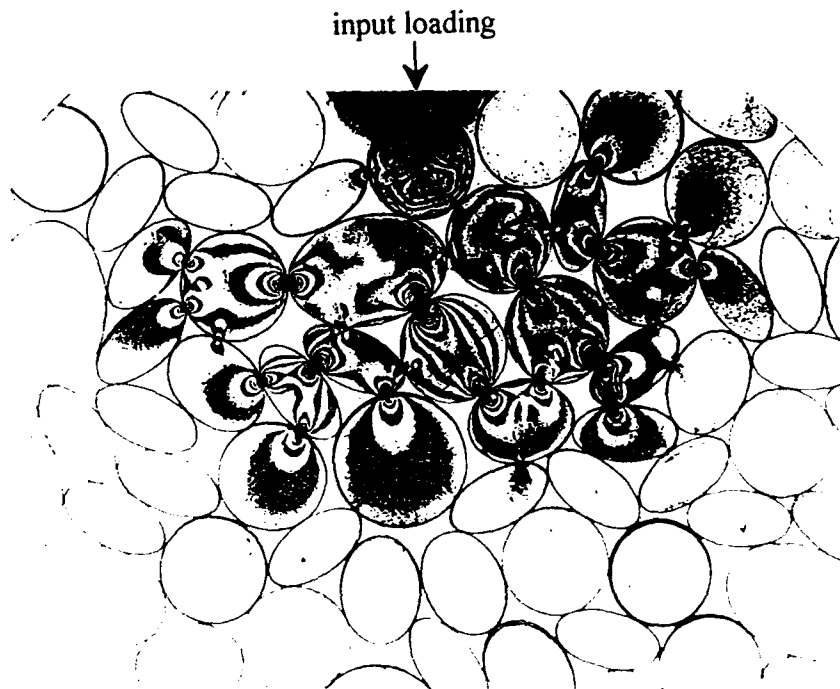


Fig. 1.2 Photoelastic Fringe Patterns of Wave Propagation in a Model Particulate Media

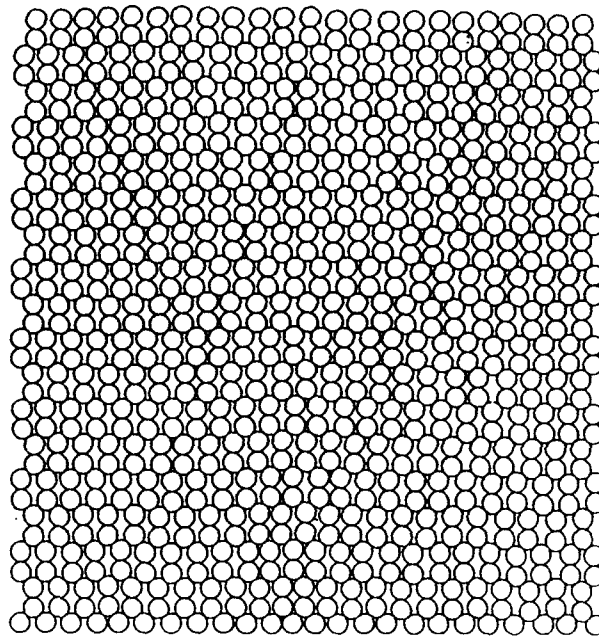


Fig. 1.3 A Strongly Anisotropic Granular Assembly (S-1)

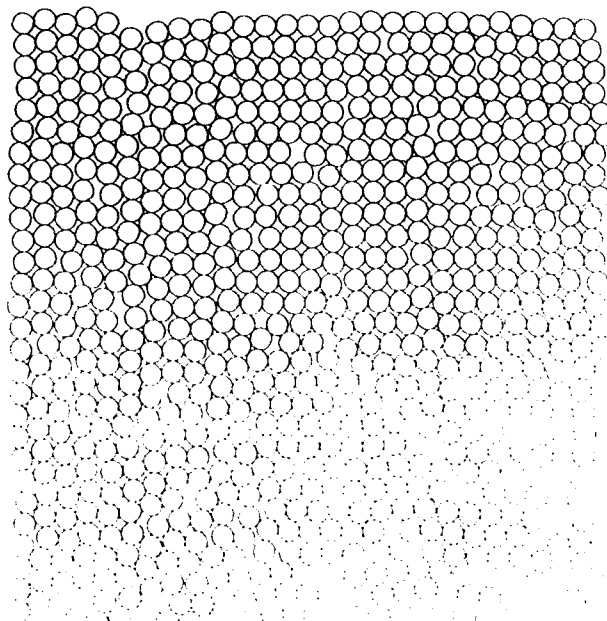


Fig. 1.4 A Moderately Anisotropic Granular Assembly (M-1)

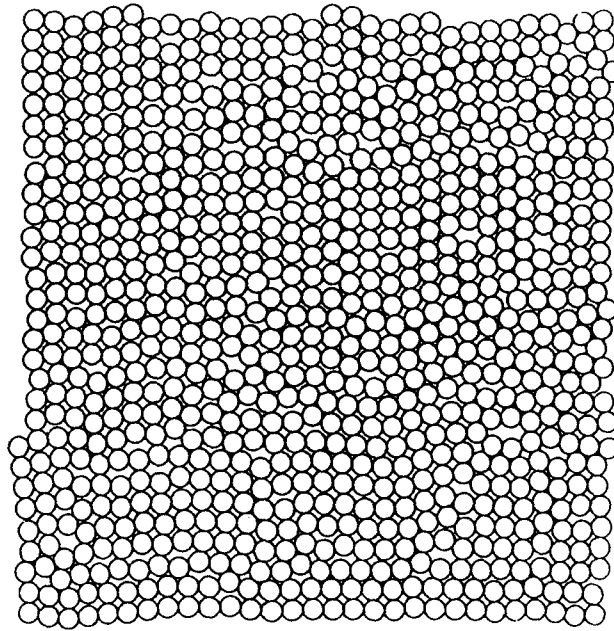


Fig. 1.5 A Moderately Anisotropic Granular Assembly (M-2)

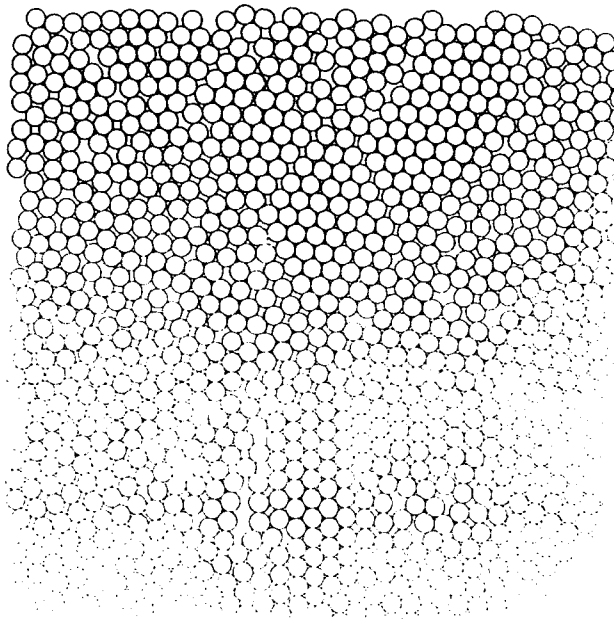


Fig. 1.6 A Weakly Anisotropic Granular Assembly (W-1)

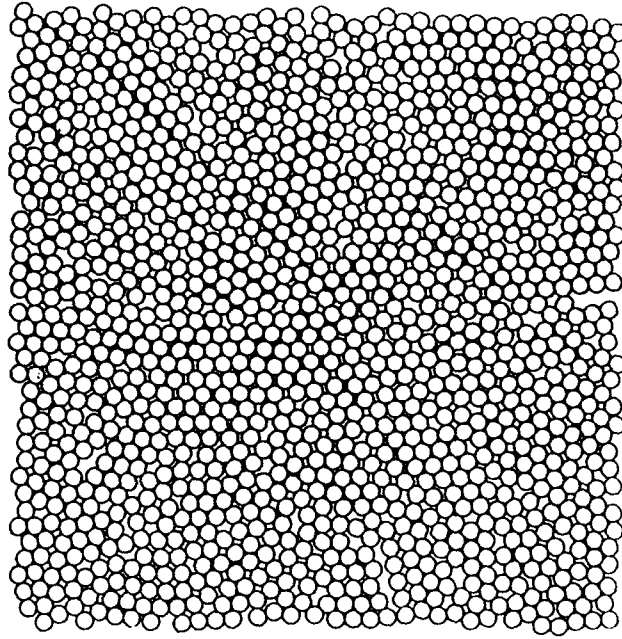


Fig. 1.7 A Weakly Anisotropic Granular Assembly (W-2)

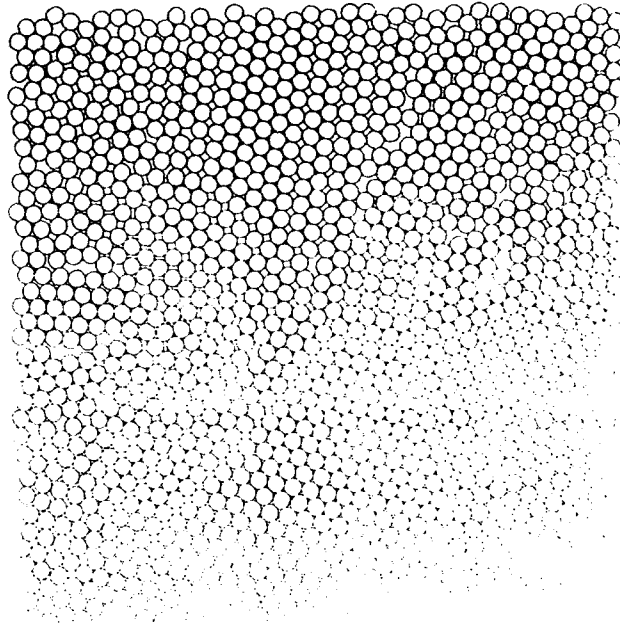


Fig. 1.8 A Weakly Anisotropic Granular Assembly (W-3)

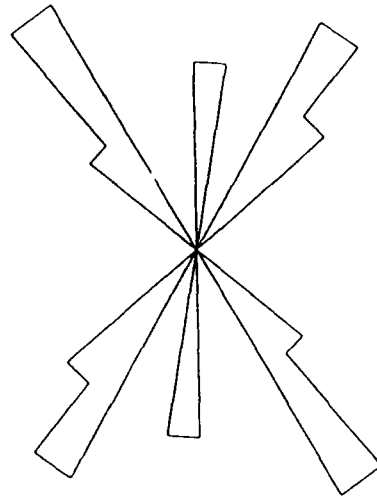


Fig. 1.9 Branch Vector Distribution of Assembly S-1

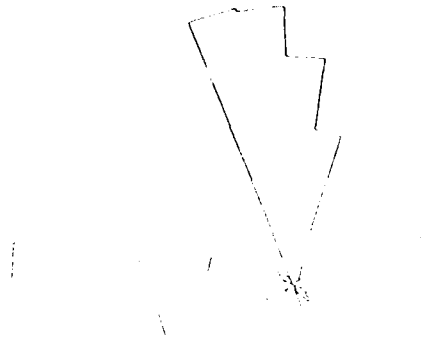


Fig. 1.10 Branch Vector Distribution of Assembly 2

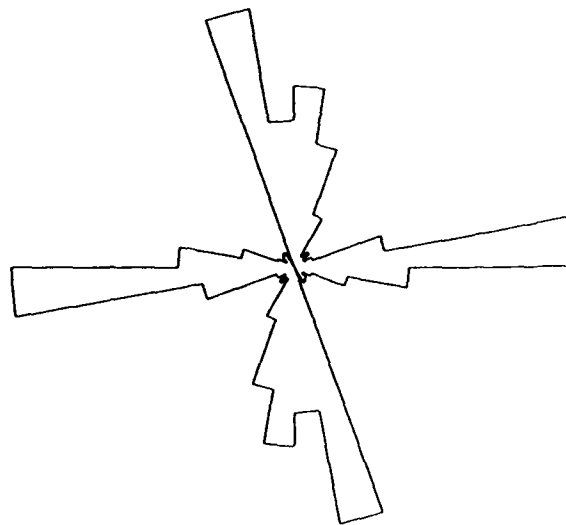


Fig. 1.11 Branch Vector Distribution of Assembly M-2

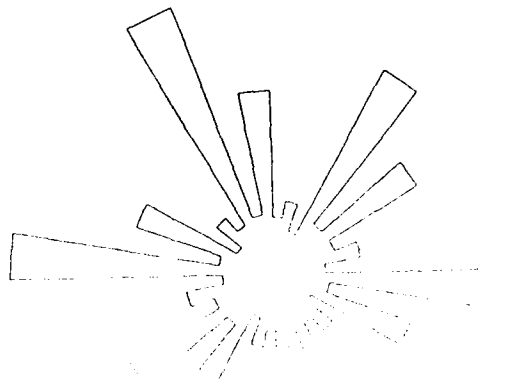


Fig. 1.12 Branch Vector Distribution of Assembly W-1

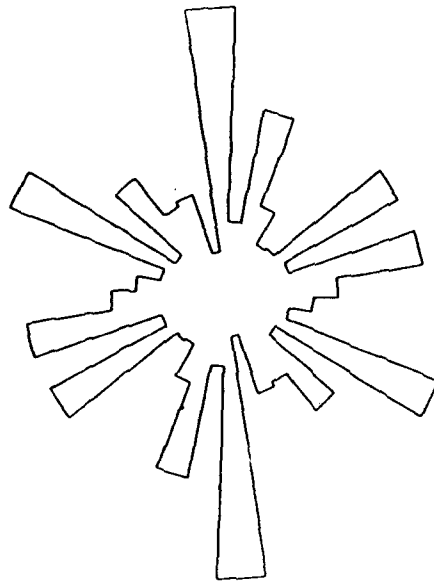


Fig. 1.13 Branch Vector Distribution of Assembly W-2

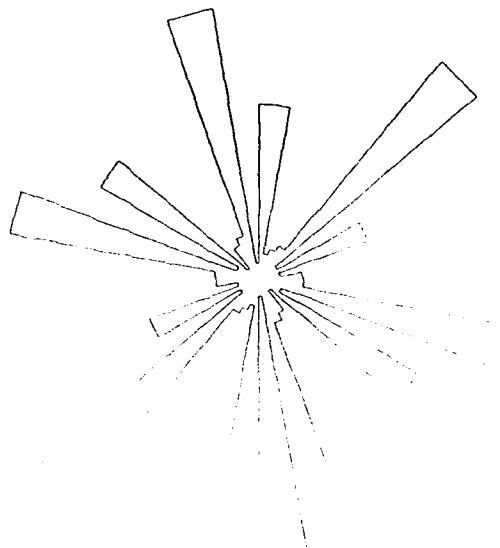


Fig. 1.14 Branch Vector Distribution of Assembly W-3

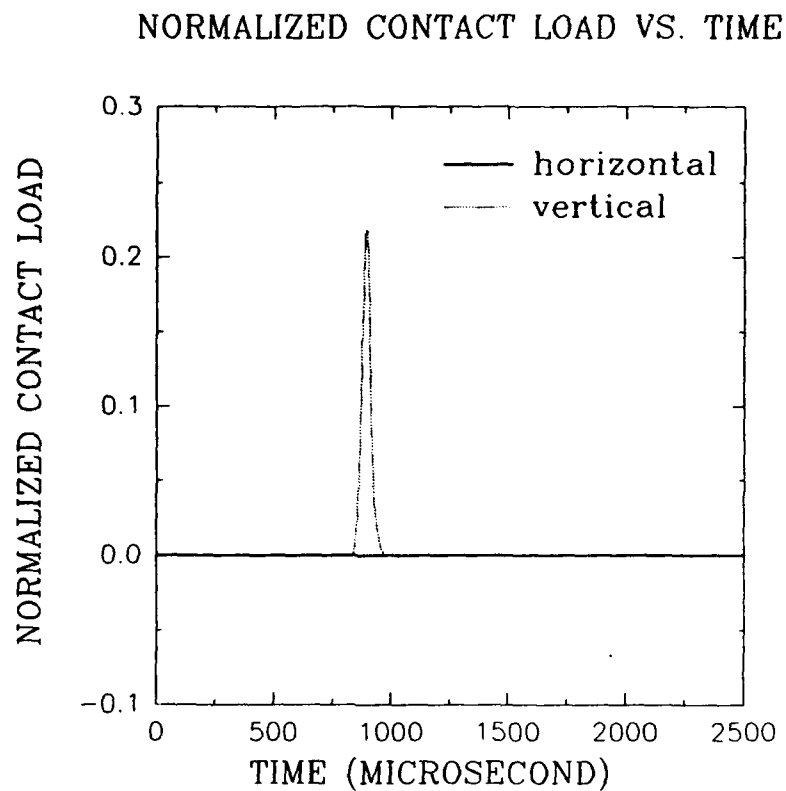


Fig. 1.15 Normalized Contact Load vs Time for the Assembly Shown in Fig. 1.3

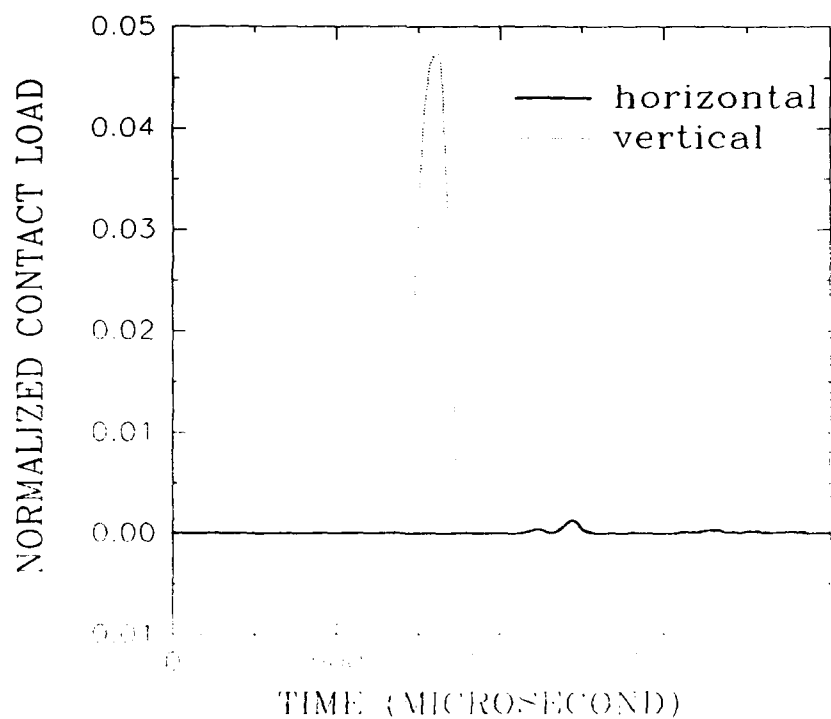


Fig. 1.16 Normalized Contact Load vs Time for the Assembly Shown in Fig. 1.4

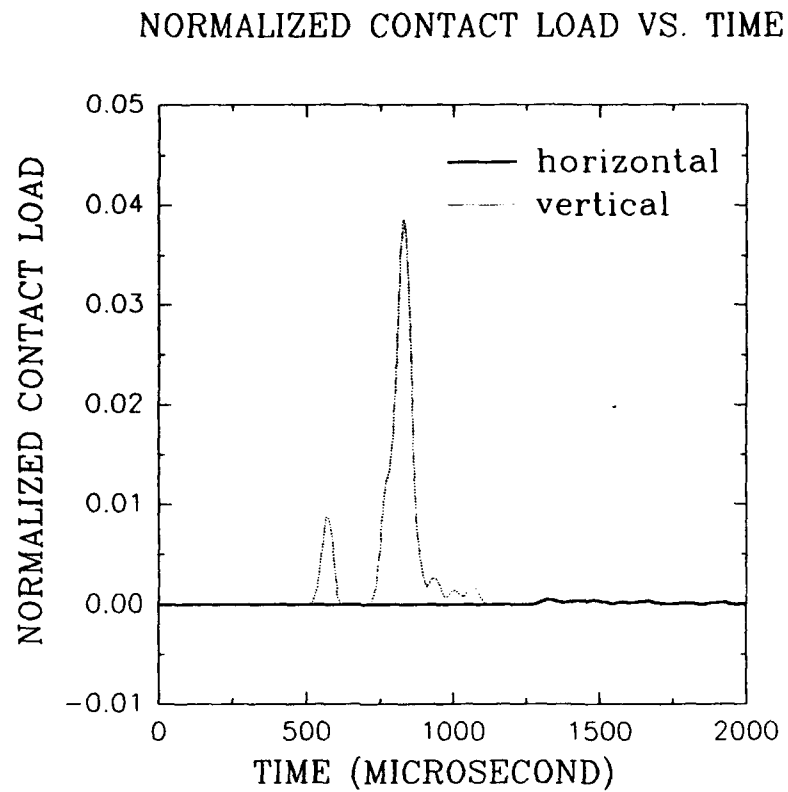


Fig. 1.17 Normalized Contact Load vs Time for the Assembly Shown in Fig. 1.5

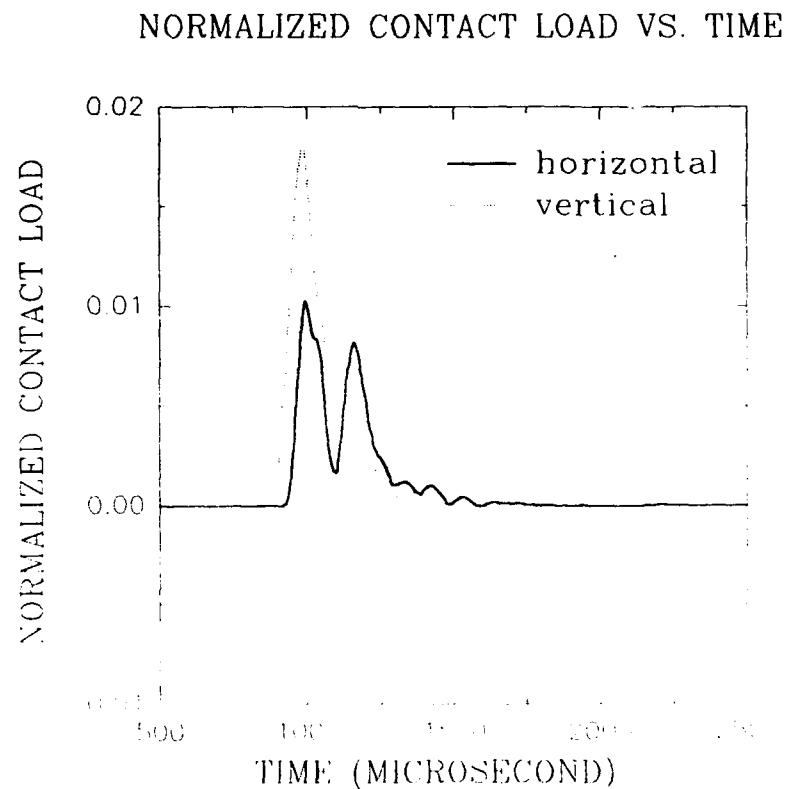


Fig. 1.18 Normalized Contact Load vs Time for the Assembly Shown in Fig. 1.6

NORMALIZED CONTACT LOAD VS. TIME

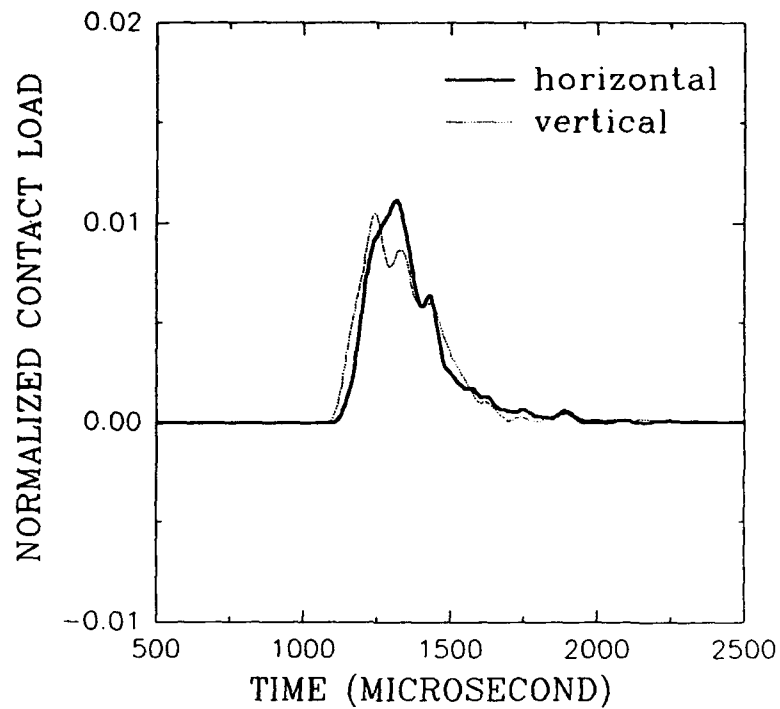


Fig. 1.19 Normalized Contact Load vs Time for the Assembly Shown in Fig. 1.7

NORMALIZED CONTACT LOAD VS. TIME

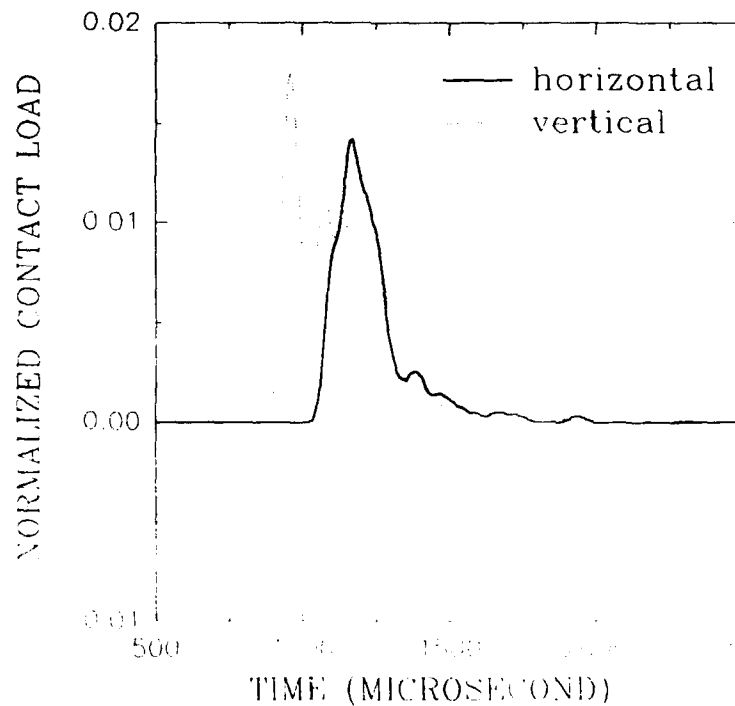


Fig. 1.20 Normalized Contact Load vs Time for the Assembly Shown in Fig. 1.8

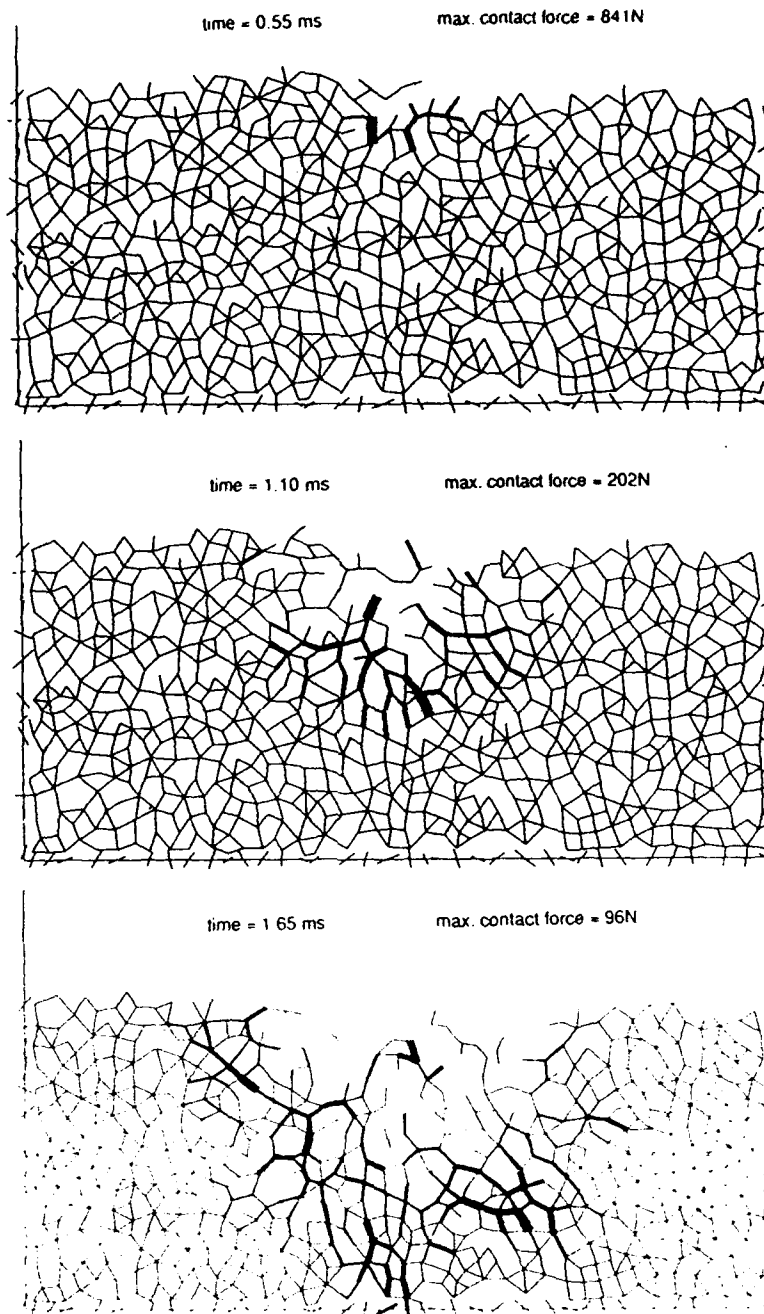


Fig. 1.21 Dynamic Load Transfer Paths (Thornton and Randall, 1988)

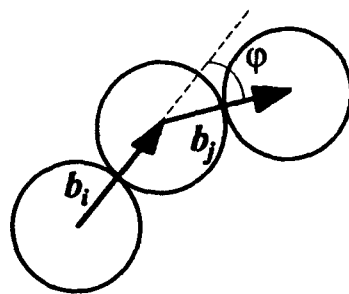


Fig. 1.22 Definiton of Branch Angle ϕ

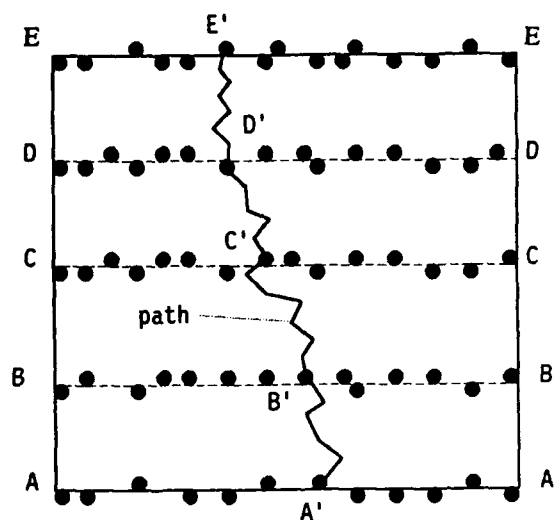


Fig. 1.23 Subregions Of An Assembly

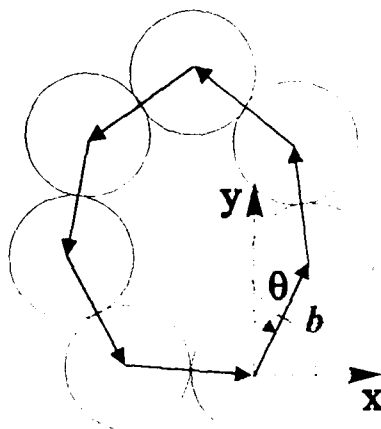


Fig. 1.24 A Void With Associated Particles And A Replaced Polygon



Fig. 1.25 Void Vector Distribution of Assembly S-1



Fig. 1.26 Void Vector Distribution of Assembly M-1

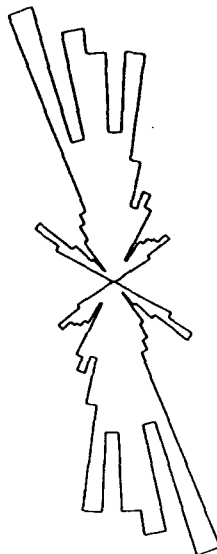


Fig. 1.27 Void Vector Distribution of Assembly M-2



Fig. 1.28 Void Vector Distribution of Assembly W-1

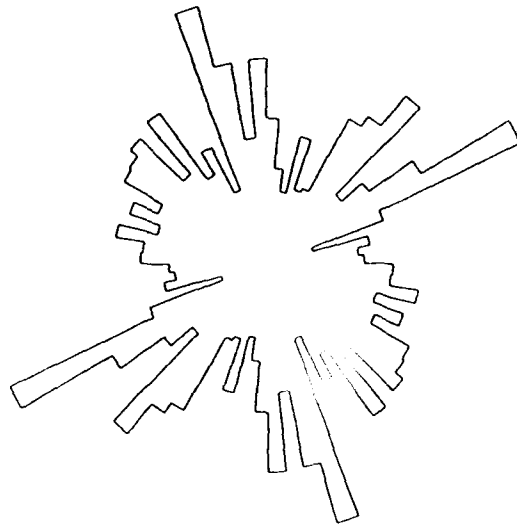


Fig. 1.29 Void Vector Distribution of Assembly W-2

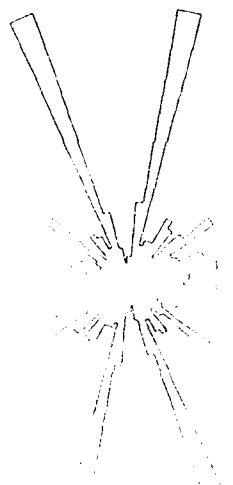


Fig. 1.30 Void Vector Distribution of Assembly W-3

CHAPTER 2

EVALUATION OF A FIBER OPTIC SENSOR FOR STRAIN MEASUREMENT AND PRELIMINARY APPLICATIONS TO CONTACT MECHANICS

2.1 Introduction

In this chapter, an attempt has been made to study the applicability of both attached and embedded fiber optic sensors to measure in plane and out of plane strain due to contact loadings. Both two and three dimensional experiments have been conducted. Prior to applying fiber optic sensors to contact mechanics problems, they were evaluated to determine the maximum strains that could be measured reliably. In the past, resistive foil strain gages have been used successfully to evaluate contacts in both static and dynamic problems (Xu and Shukla, 1993). However, strain gages are limited in their use to surface strain measurements. Also, they cannot be easily bonded to certain kinds of materials like rock and concrete. Fiber optic sensors on the other hand can be used for both surface (Sirkis and Taylor, 1988) and interior strain measurements (Murphy *et. al.*, 1989). Fiber optic sensors have also been shown to be applicable for use in electrically noisy environments (Griffiths, 1991), and in high temperature areas (Wang, 1992). The ultimate aim of the study is to accurately predict local strains at any point in a three dimensional body for both static and dynamic loading.

2.2 Sensor Construction

2.2.1 Mach-Zehnder Interferometer

Construction of a Mach-Zehnder sensor is quite simple, and a schematic of the setup is shown in Fig. 2.1. A laser beam is split with a beam splitter and the two resulting beams are then coupled into two separate single mode optical fibers. One of the fibers is chosen as the reference path and the other fiber becomes the sensing arm. The two separate beams are then recombined and the resulting interference pattern is projected onto a photodiode. The interference fringes produced can be related to the axial strain seen by the sensor.

In operation, the fringe pattern remains stationary when the sensor undergoes no strain and the output from the photodiode is constant. When the sensor experiences axial strain, the fringe pattern shifts across the face of the photodiode resulting in a sinusoidal type output. It is this sinusoidal output that can be related to the applied strain.

Care must be taken with the *Mach-Zehnder interferometer* because all of the fiber in the setup has the potential to affect the light propagating through it. In other words, the entire length of fiber, in either arm, can be the sensing element. Care must be taken to ensure that only the desired measurand is affecting the output signal. This is one of the drawbacks to the sensor and therefore, it is not easily applicable to field applications.

2.2.2 Fabry-Perot Interferometer

Fig. 2.2 shows a schematic of an extrinsic Fabry-Perot sensor. The experimental setup is almost the same as that for the Mach-Zehnder and is shown in Fig. 2.3. The schematic of the actual sensor, Fig. 2.2, shows two pieces of optical fiber that are bonded into a glass tube. The fiber ends are partially mirrored to provide the necessary reflections for a low finesse Fabry-Perot cavity. Fiber diameter that is used in the laboratory is 125

microns due to the availability of the appropriate couplers and equipment for this size fiber. Purchasing ready made sensors is quite expensive and since the sensors may become damaged during experiments, a simple method to manufacture them was needed.

Since this sensor is an interferometric sensor, a single mode fiber rated to carry the particular input wavelength is used. A helium-neon laser is used in the laboratory so the single mode fiber is purchased to support the 633 nm wavelength. Approximately 0.5 m of single mode fiber is cleaved for the sensor. The completed sensor is later coupled to the experimental setup using Norland Lab Splices. The fiber that provides the opposite mirrored surface is a multimode fiber because of its lower cost. This fiber only needs to be long enough to insert into the glass tube but is generally cut to approximately 50 mm for ease of handling.

The mirroring is done with sputtering equipment and aluminum is used to create the mirrors. The fibers are first carefully cleaved and cleaned to provide a flat surface upon which to sputter the aluminum. Sputtering times may vary with equipment so a glass slide is first placed in the sputterer to determine an appropriate time. Reflectivity should be approximately 25% on the single mode fiber and from 25% to 100% on the multimode fiber.

After the fibers were coated, the glass tube was prepared. A short length of glass tubing, approximately 25 mm, was cut and one end cleaved flat. The tubing measured 135 microns on the inside diameter and 190 microns on the outside diameter. Both the prepared tubing and one of the coated fibers were placed into a jig that was developed to allow alignment of the fiber and the tube under an optical microscope. The jig is shown in Fig. 2.4 and consists of an X-Y positioner with Z translation and a mirror

holder/positioner that is used to allow the fiber and the tube axes to be made parallel. This jig was angled, with respect to the horizontal, to allow viewing of the tube end while the fiber was being positioned for insertion. This open tube end always faces up and is located over the small white reflective surface to provide back-lighting.

The first fiber was inserted into the prepared end of the tube and bonded using a five minute epoxy. The fiber was inserted so as to achieve the desired gage length and to allow approximately 10-40 microns between coated fiber ends when the sensor was completed. After the epoxy was cured, the tube was cleaved again to the desired gage length, the second fiber was inserted and positioned for the correct gap, and the epoxy was applied to the second fiber. Once the epoxy has cured, an accurate measurement of the finished gage length is made under the microscope, and the sensor is ready for use.

2.3 Calibration

The principle of operation of a Mach-Zehnder interferometric fiber optic sensor was mentioned above. The axial strain, ϵ_x , is directly proportional to the number of fringes, N , moving past a fixed point and can be given as (Butter and Hocker, 1978)

$$\epsilon_x = DN \quad (2.1)$$

where D is the proportionality constant and can be written as

$$D = \left(\frac{\lambda}{nI} \right) \left[\frac{1}{1-c} \right] \quad (2.2)$$

where λ is the vacuum wavelength of the optical beam, I is the gage length of the sensor, n is the refractive index of the fiber, and c is a constant which depends on strain optic coefficients, the refractive index, and Poisson's ratio of the fiber. It is possible to

calculate D for pure silica, however, dopants are used to alter the refractive index of the core of the fiber to keep the light propagating in the fiber. Hence, the fiber has to be calibrated to determine the constant D.

The Mach-Zehnder sensor was calibrated using a cantilever beam setup as shown in Fig. 2.5. The fiber sensor was mounted to a cantilever beam, opposite a conventional strain gage. The beam was displaced and a plot of the axial strain recorded from the strain gage vs. the fringes was made for a particular gage length of the fiber. A straight line was fit through the data points. The slope of this straight line was the constant D as shown in Fig. 2.6. The strain required to cause one fringe to move across a fixed point is

$$\epsilon_x = \left(\frac{A}{L} \right) N \quad (2.3)$$

inversely proportional to the gage length of the sensor. In other words, equation (2.1) can be written as shown in equation (2.3) where A is the fringe strain sensitivity constant for the sensor. The fringe strain sensitivity can be defined as the strain required to cause one fringe to move across a given point for a unit gage length of the sensor. The experimentally obtained value for A was found to be $625 \mu\text{mm}/\text{mm fringe}^{-1} \text{ mm}$.

Strain is obtained from the Fabry-Perot sensor in much the same way as the Mach-Zehnder sensor. However, the relationship between the number of fringes passing and the strain is only dependant on the wavelength of the light propagating and the gage length of the sensor. Calibration of the sensor is not necessary. The relationship between the fringe shift and the axial strain is explicitly given by equation (2.4). Again, N is the number of fringes, λ is the wavelength of light, and L is the measured gage length of the

sensor.

$$\epsilon_x = \frac{\lambda N}{2I} \quad (2.4)$$

2.4 Evaluation of the Fiber Optic Sensor

2.4.1 Tension Testing

The Mach-Zehnder sensor was used for the initial evaluation of the fiber optic sensor. A single mode fiber with an outer diameter of 80 microns was stripped of its plastic jacket in the region that was to be bonded to the specimen. The plastic jacket must be stripped to ensure proper strain transfer between the specimen and the optical fiber. Also, the surface of the specimen must be treated in accordance with conventional strain gage techniques prior to attachment. Two pieces of tape were placed on the specimen leaving the desired gage length exposed between the tape pieces. These tape pieces serve as masks so that only the desired length of fiber will be bonded. The tape mask was then sliced along the direction that the fiber will run. This was done to allow the tape to be removed after the fiber is bonded. Fig. 2.7 shows the specimen with the tape mask in place. The fiber was then laid into the slice and bonded. After the adhesive cures, the tape is removed.

A simple tension test was used to characterize the fiber sensor under axial loading conditions. A schematic of the setup for the Mach-Zehnder interferometer was shown in Fig. 2.1. The specimen was a dog bone specimen with a resistance type strain gage bonded to one side of the specimen and the fiber-optic sensor bonded to the other side, directly opposite the strain gage. The experiments were designed for axial strain

measurements only. To standardize the bonding procedure, both sensors were bonded with M-Bond 200, a cyanoacrylate based adhesive, using the technique described in Measurements Group Bulletin 309A. Ambient conditions in the laboratory are maintained at 21°C , ± 3 , and 65% relative humidity, ± 5 .

The specimens were then loaded at a constant strain rate and the strain gage signal was recorded, along with the light intensity signal from the photodiode, with a Lecroy data acquisition system. In each experiment, loading was continued until failure of either the strain gage or the fiber-optic sensor.

Another series of experiments was conducted in which the specimen was loaded in incremental values from an unloaded condition to a failure condition. The specimen was unloaded and removed from the fixture at 500 microstrain increments and taken to an optical microscope for inspection. The specimen was examined and photographs were taken of any significant changes in the adhesive bond. After reconnecting the two sensors to the data acquisition equipment, the specimen was strained to the next incremental value and the procedure was repeated.

Fig. 2.8 shows typical output from the strain gage and the Mach-Zehnder sensor for the axial loading experiments. The strain data from both the strain gage and the fiber sensor is shown in Fig. 2.9.

It can be seen that the Mach-Zehnder sensor was linear and the sensor can be used for strain measurements. However, the fiber-optic sensor was found to fail at strain levels far below the levels at which conventional strain gages fail. Failure modes could be characterized in two ways:

- the fiber fractures and the sensing signal is lost.

- the fiber delaminates with matrix cracking, resulting in a change in effective sensor gage length.

Note that the delamination and matrix failure is related to the bonding of the fiber and does not represent a shortcoming of the glue. A separate experiment was conducted with only a thin layer of glue and the glue did not show cracking or failure during the experiment. The maximum value reached during this experiment was 2 percent strain.

The data presented in Fig. 2.9 shows failure by fracture of the fiber which resulted in loss of the sensing signal and therefore, loss of the interference fringes. Both modes of failure produced unusable data at values between 1.2-1.8 percent strain. Photographs taken during the incremental loading are shown in Fig. 2.10. Fig. 2.10(a) shows the fiber in an unstrained state and as it appears up until failure. The bright line running down the center of the fiber is the contact between the fiber and the specimen. Note that the glue does not cover the entire fiber but rather forms a bed under the fiber.

In Fig. 2.10(b), the delaminated region shows up as a wide, bright band. This is caused by the defracting of the microscope light from the air gap that opened up between the fiber and the specimen. Under actual observation the band appears as colored fringes. Note also that the glue matrix shows cracking. These cracks will always curve toward the portion of the fiber that is unattached and unstrained, and therefore show that delamination has occurred from left to right in the photograph. The right side of the photograph shows the portion of fiber that has not yet delaminated.

Fig. 2.10(c) represents an experiment in which the fiber fractured. There is a central crack in the matrix that is aligned with the fracture in the fiber. All other cracks curve toward the fracture area. This matrix cracking shows that subsequent delamination

of the fiber occurred after the fracture and ran outward from the fiber fracture in both directions.

Fig. 2.11 shows strain data obtained from the incremented experiment. The strain gage data was plotted using a linear regression curve fit. The data shows that the specimen remained linearly elastic throughout the experiment. The first run, represented by the circles, and the second run, represented by the inverted triangles, was made up to 1 and 1.5 percent strain, respectively. Following the second run, observation of the fiber sensor showed delamination, see Fig. 2.10.

Analysis of the raw data showed the effect of the delamination on the fiber sensor output. Fig. 2.12 shows an anomaly that occurred at approximately 13,200 microstrain, during the 2nd run. The fringes from the 1st run, where no anomaly was seen, and those that precede and follow the anomaly in the 2nd run, are regular and do not appear distorted.

Since the strain calculation, given in equation (2.1), is based on the gage length, the observed strain will be affected if a change in gage length is not accounted for. This affect can be seen in Fig. 2.11, runs 3 and 4. Runs 3 and 4 were made up to 1.6 and 1.7 percent strain, respectively. Fringes from both of these runs showed numerous anomalies.

From these observations, it is believed that the initial delamination occurred at the end of the second run and the damage grew during the 3rd and 4th runs. This damage growth is illustrated by the difference in strain observed in those runs.

From the initial failure experiments, it was determined that the fiber sensor typically failed at strains around 1.5%. The first strain level at which to stop was set at 1% strain, or 10,000 microstrain. In all experiments, the sensor showed no significant

changes before reaching this strain level. The 500 microstrain increment was then followed until failure.

From these characterization experiments it was determined that fiber optic sensors could be confidently used up to a strain level of 1.5 percent.

2.5 Experimental Procedures for Contact Strain Measurements

The first set of experiments was aimed at applying fiber optic sensors to measure strains due to a static load. Disks 32 mm in diameter were machined from 6 mm thick plexiglass sheets. A fiber-optic Fabry-Perot strain sensor was bonded to the surface of the disk, close to the point of the applied load. The disk was then loaded in compression and data was collected from a PCB load cell and a photodiode using a Lecroy data acquisition system. The disk was loaded to approximately 1000 N.

The second set of experiments were designed to measure out of plane strains in a disk using the same loading configuration as that used with the Fabry-Perot, however, a Mach-Zehnder sensor was used. A 2 mm hole was drilled through the thickness of the disk. The jacket on the fiber was removed and the fiber was embedded through the thickness using a chemical called Envirotex, whose mechanical properties are very similar to those of plexiglass.

Again, a piezoelectric load cell placed directly below the disk was used to acquire the loading data. From theory, strains can be calculated at any point on the disk if the load is known. As mentioned, the fiber was embedded on the loading axis and close to the contact point so that Hertz equations could be utilized for the analysis. A Lecroy data acquisition system was used to record both the fiber optic and load cell signals.

For the three dimensional experiments, 25.4 mm plexiglass spheres were embedded with a fiber, utilizing the Mach-Zehnder sensor, through a 2 mm hole. The experimental procedure was the same as that for the disks with the embedded fiber.

2.6 Theory

2.6.1 Two dimensional strains

The stress field equations for a disk are given in (2.5), (2.6), and (2.7) (Smith and Liu, 1953).

$$\sigma_{zz} = -\frac{b}{\pi\Delta} \left[z(b\phi_1 - x\phi_2) + \beta z^2\phi_2 \right] \quad (2.5)$$

$$\begin{aligned} \sigma_{xx} = -\frac{b}{\pi\Delta} \left[z \left(\frac{b^2 + 2z^2 + 2x^2}{b} \phi_1 - \frac{2\pi}{b} - 3x\phi_2 \right) \right. \\ \left. + \beta \left((2x^2 - 2b^2 - 3z^2)\phi_2 + \frac{2\pi x}{b} \right) \right. \\ \left. + 2(b^2 - x^2 - z^2) \frac{x}{b} \phi_2 \right] \end{aligned} \quad (2.6)$$

$$\begin{aligned} \sigma_{zx} = -\frac{b}{\pi\Delta} \left[z^2\phi_2 + \beta \left((b^2 + 2x^2 + 2z^2) \frac{z}{b} \phi_1 \right. \right. \\ \left. \left. - 2\pi \frac{z}{b} - 3xz\phi_2 \right) \right] \end{aligned} \quad (2.7)$$

The terms ϕ_1 and ϕ_2 are given by the following

$$\phi_1 = \frac{\pi(M + N)}{MN\sqrt{2MN + 2x^2 + 2z^2 - 2b^2}} \quad \phi_2 = \frac{\pi(M - N)}{MN\sqrt{2MN + 2x^2 + 2z^2 - 2b^2}}$$

$$M = \sqrt{(b + x)^2 + z^2}$$

$$N = \sqrt{(b - x)^2 + z^2}$$

The term Δ is a parameter that is dependant on the material elastic properties, E and ν ,

and the radii of curvature of the two objects in contact, and is given in equation (2.8).

$$\Delta = \frac{1}{\left(\frac{1}{2R_1}\right) + \left(\frac{1}{2R_2}\right)} \left(\frac{1-\nu_1^2}{E_1} + \frac{1-\nu_2^2}{E_2} \right) \quad (2.8)$$

The friction factor, β , is taken to be zero because there is no tangential load and the half contact width, b , is found using the load data and given by equation (2.9).

$$b = \sqrt{\frac{2P\Delta}{\pi h}} \quad (2.9)$$

The strain along the loading axis, ϵ_{zz} , is given by equation (2.10). The assumption of plane stress conditions, $\sigma_{yy}=0$, has been made due to the geometry of the disks and equation (2.10) reduces to equation (2.11).

$$\epsilon_{zz} = \frac{1}{E} (\sigma_{zz} - \nu (\sigma_{xx} + \sigma_{yy})) \quad (2.10)$$

$$\epsilon_{zz} = \frac{1}{E} (\sigma_{zz} - \nu (\sigma_{xx})) \quad (2.11)$$

Equation (2.11) is the theoretical strain on the surface of the disk given the geometrical conditions and the load.

From theory, the transverse strain, ϵ_{yy} , is given by equation (2.12).

$$\epsilon_{yy} = \frac{1}{E} (\sigma_{yy} - \nu (\sigma_{xx} + \sigma_{zz})) \quad (2.12)$$

Again, a plane stress assumption is made given the disk geometry and (2.12) is reduced to (2.13).

$$\epsilon_{yy} = -\frac{\nu}{E}(\sigma_{xx} + \sigma_{zz}) \quad (2.13)$$

To summarize, if the load is known and the geometry of the two bodies in contact is given, the surface strain, equation (2.11), and the transverse strain, equation (2.13), can be calculated.

If the fiber is far away from the diametrically opposite side, the effect of the load from the opposite side is relatively small and this has been shown in Fig. 2.13. This plots shows the percent error in the calculation of transverse strain, ϵ_{yy} , as a function of the normalized position of the sensor.

2.6.2 Stress in a sphere

Johnson (1985) presents equations for the stresses along the z-axis in a sphere. These equations are

$$\sigma_r = \sigma_\theta = p_0 \left(- (1+\nu) \left(1 - \frac{z}{a} \tan^{-1} \frac{a}{z} \right) + \frac{1}{2} \left(1 + \frac{z^2}{a^2} \right)^{-1} \right) \quad (2.14)$$

$$\sigma_z = -p_0 \left(1 + \frac{z^2}{a^2} \right)^{-1} \quad (2.15)$$

The terms in these expressions are given in the following equations.

$$a = \left(\frac{3PR}{4E^*} \right)^{1/3} \quad (2.16)$$

The effect of superposition from the diametrically opposite load was neglected for

$$\frac{1}{R} = \frac{1}{R_1} + \frac{1}{R_2} \quad (2.17)$$

$$\frac{1}{E^*} = \frac{1-\nu_1^2}{E_1} + \frac{1-\nu_2^2}{E_2} \quad (2.18)$$

$$p_o = \frac{3P}{2\pi a^2} \quad (2.19)$$

$$\epsilon_x = \frac{1}{E}(\sigma_x - \nu(\sigma_y + \sigma_z)) \quad (2.20)$$

the reasons stated above in the theoretical derivation for a disk under diametral compression.

2.7 Results and Discussion

From the results, it is seen that the Mach-Zehnder fiber optic sensor can be embedded in bodies and used to record strains. Fig. 2.14 and 2.15 are theoretical plots of expected strain values and expected number of fringes for varying loads and varying the position of the embedded sensor on the z-axis. Fig. 2.16 and 2.17 show a comparison of the experimental and theoretically obtained strain values for the disk experiments. Fig. 2.18 shows the typical outputs of the fiber optic sensor and the piezoelectric load cell. Fig. 2.19 is a plot of the experimental and theoretical half contact width vs. the contact load. A consistent deviation in the slope of the theoretical and experimental plot was observed in all the experiments using the Mach-Zehnder embedded in disks. A number of reasons for these errors were explored and are listed below:

- improper measurement of the gage length of the fiber. Due to the nature of embedding, the measured value of embedded length of fiber, or in other

words the gage length, might not be accurate because the effective load carrying length of the fiber is dependent upon the embedding technique.

- the equations used to compute the strain were based on infinite elastic half spaces with a Hertz contact area. An attempt to include the effect of the force being applied at the diametrically opposite side was made based on the work in Johnson(1985). A concentrated force was assumed for the opposite side and the superposition principle was applied. The theoretical plot of the expected error is shown in Fig. 2.13. The superposition of the opposite force did not contribute significantly to the strain computations.
- the Mach-Zehnder sensor yields an average value of the strain over the embedded length but the theoretical equations are valid for a point on the body. The development of an integral expression for strain along the embedded length might produce more accurate results. Another alternative would be to use a "point" sensor, such as a Fabry-Perot sensor, because of its ability to measure strain within a small gage length.
- the presence of air bubbles in the filling compound might have altered the effective gage length.

Fig. 2.20 shows the data obtained from the Fabry-Perot sensor attached to a disk under diametral compression. Again, the theoretical line was obtained using load data from the load cell and applying Hertz contact theory to calculate the strain at the sensor location. The plot shows agreement with the theoretical prediction within 14%.

Predicting stress and strain profiles in three dimensional bodies is an order of

magnitude more complicated. For the three dimensional experiments, a sphere, which is the most simple representation of a 3d body, was used as the specimen and a fiber was embedded using the same process as for the disks. To avoid numerical procedures, strains were computed for a point along the z-axis.

As was the case in disks, a very significant deviation in slope was observed between the theoretical and experimental values of strain. Once again, the experimentally obtained value of strain is the average value of strain along the embedded length where as the theoretically obtained values are for a point on the z-axis. In a sphere, the strain increases in magnitude from the free surface to a interior point on the z-axis(Johnson, 1985). Perhaps an arithmetic mean of the theoretical strain would afford better comparison with the experimentally obtained value of average strain along the embedded length.

Fig. 2.21 shows the characteristic fiber optic and load cell output for a sphere under compression. The theoretical equations are non linear and a slight amount of non linearity was observed in the strain vs. load plots as seen in Fig. 2.22.

2.8 Conclusion

The Mach-Zehnder fiber-optic sensor measured axial strains with acceptable accuracy and these strain measurements have been shown to be linear up until the failure point of the sensor. This failure point, using the technique described in this paper, has been shown to be much lower, typically 1.2-1.8 percent strain, than that taken to be accepted maximums for attached resistance type strain gages, 3-6 percent strain. Failure has been shown to be either due to fiber fracture or delamination and glue failure. For applications in our laboratory, this upper limit of measurement is above the strains

encountered. Experiments were also conducted in which the entire fiber was covered with glue. Covering the fiber entirely with glue produced fiber fracture only. The glue showed cracking at the fiber fracture point and the failure strains were comparable with the values presented in this paper.

The Mach-Zehnder sensor can be embedded through bodies to measure strains. The strains predicted by the sensor are an average over the gage length and can only approximate the actual strain value at a unique point. The technique used to embed the fibers is critical for accurate prediction of strain values. The experiments using the 32 mm diameter disks proved that transverse strains due to Poisson's ratio effect can be approximately predicted by these sensors. Sub surface strains in spherical bodies under diametral compression can also be predicted by Mach-Zehnder fiber optic sensors. However, the value of the strain predicted is an average strain over the embedded length of the sensor. This strain prediction is very large when compared to the theoretical strain at a point inside of the sphere. For comparison to the theory, a more suitable sensor would be the Fabry-Perot interferometric sensor.

Fabry-Perot sensors have been shown to be applicable for determining contact parameters. The sensor was within 14 percent agreement with the theoretical values.

The mechanisms of failure described for the Mach-Zehnder sensor are speculated to be indicative of those for the Fabry-Perot sensor. However, preliminary work has shown that there is a dependance of the failure strain on both the diameter and the material properties of the glass tube used in constructing the Fabry-Perot.

This chapter represents preliminary results of contact strain measurements using fiber optic sensors. The work will be continued in the coming year.

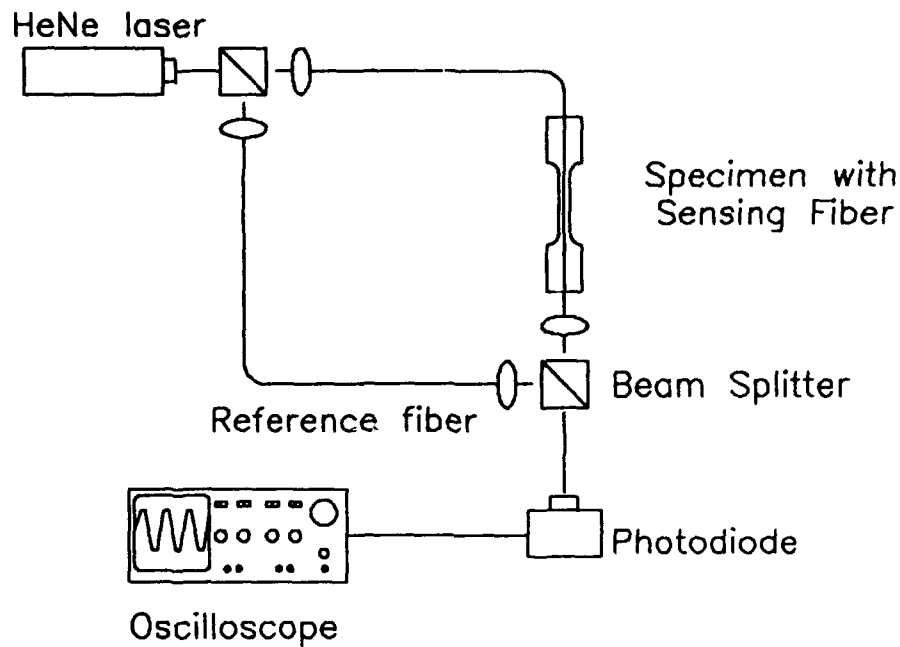


Figure 2.1. Schematic of the experimental setup for the Mach-Zehnder sensor.

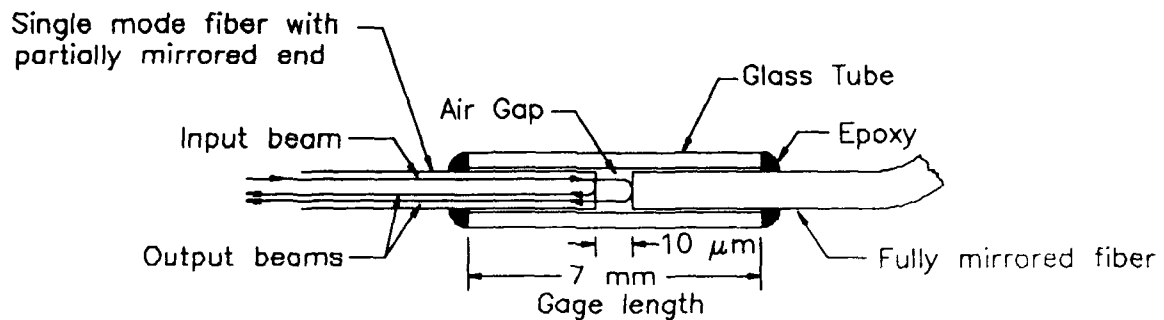


Figure 2.2. Schematic of the Fabry-Perot sensor.

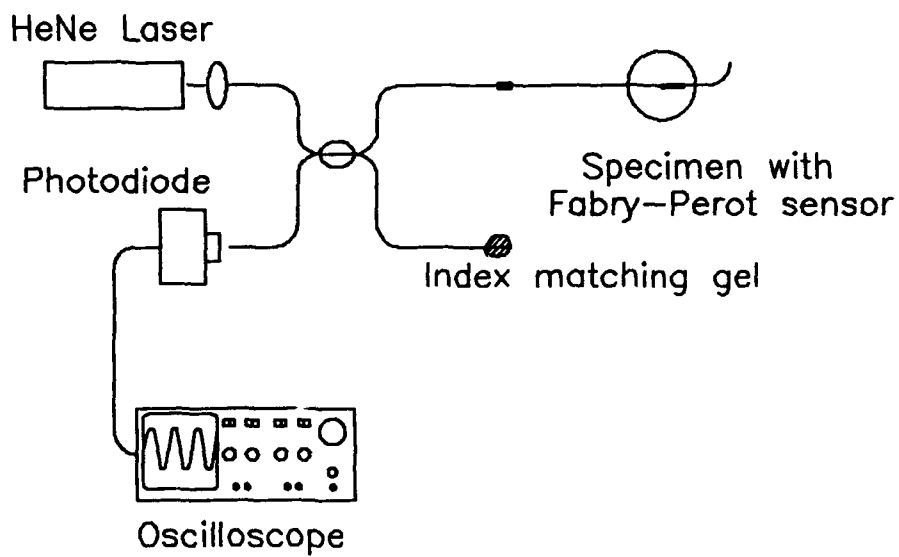


Figure 2.3. Schematic of the experimental setup for the Fabry-Perot sensor.

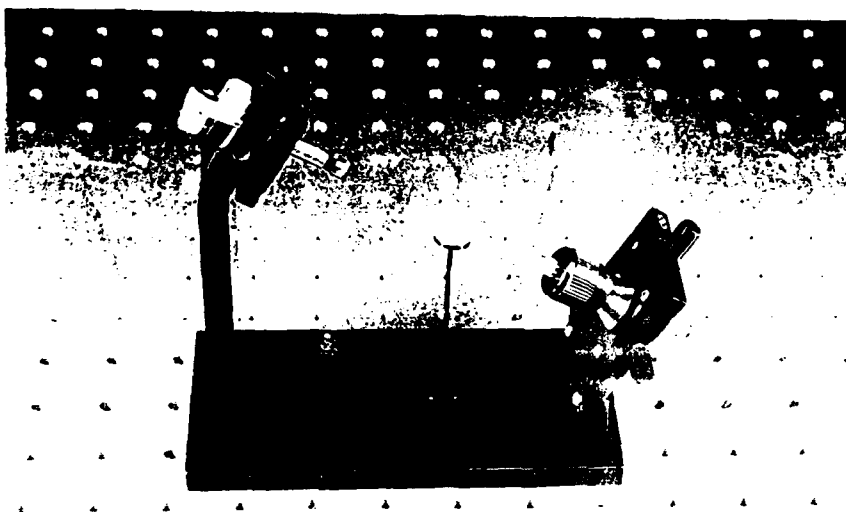


Figure 2.4. Jig for construction of Fabry-Perot sensor.

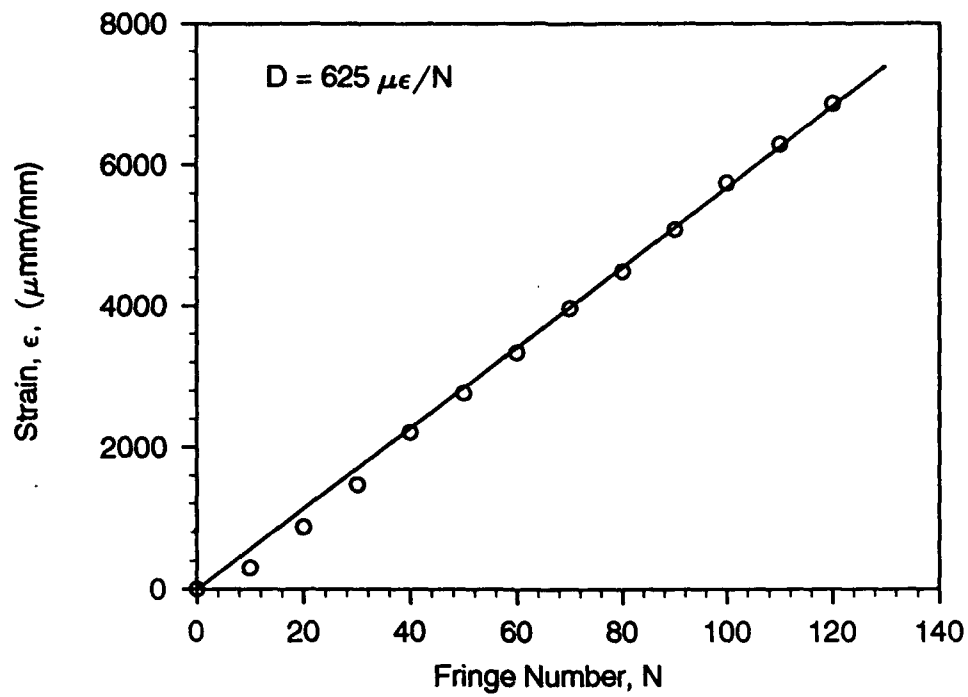


Figure 2.5. Calibration plot for the Mach-Zehnder sensor.

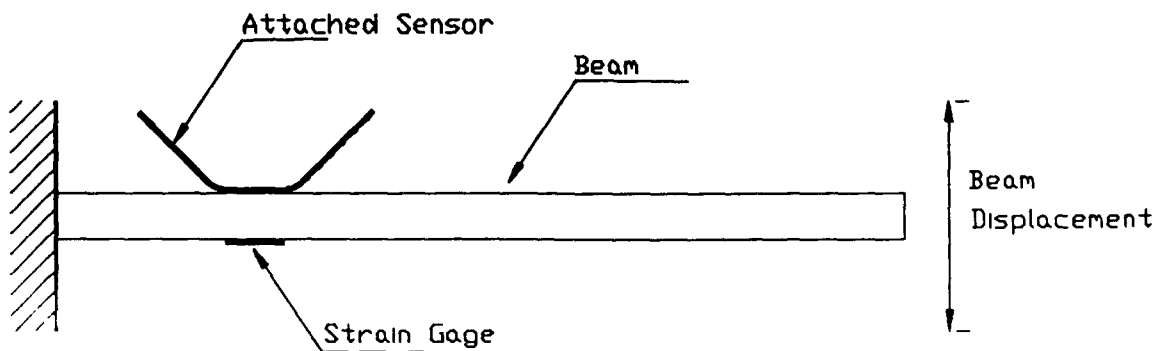


Figure 2.6. Schematic of cantilever beam for calibration of the Mach-Zehnder sensor.

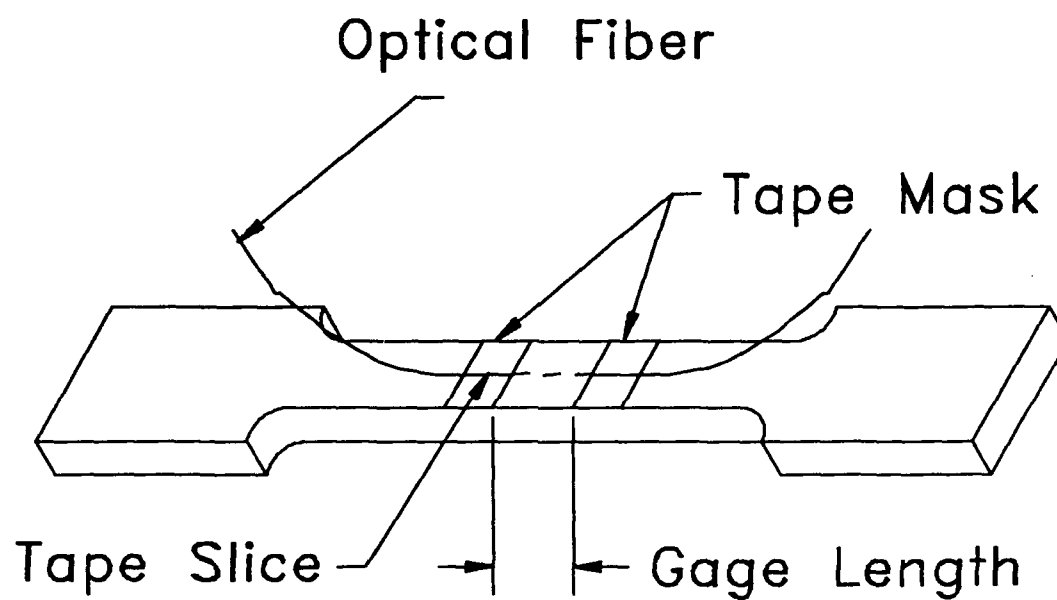


Figure 2.7. Typical specimen for tension testing showing masked area and exposed gage length.

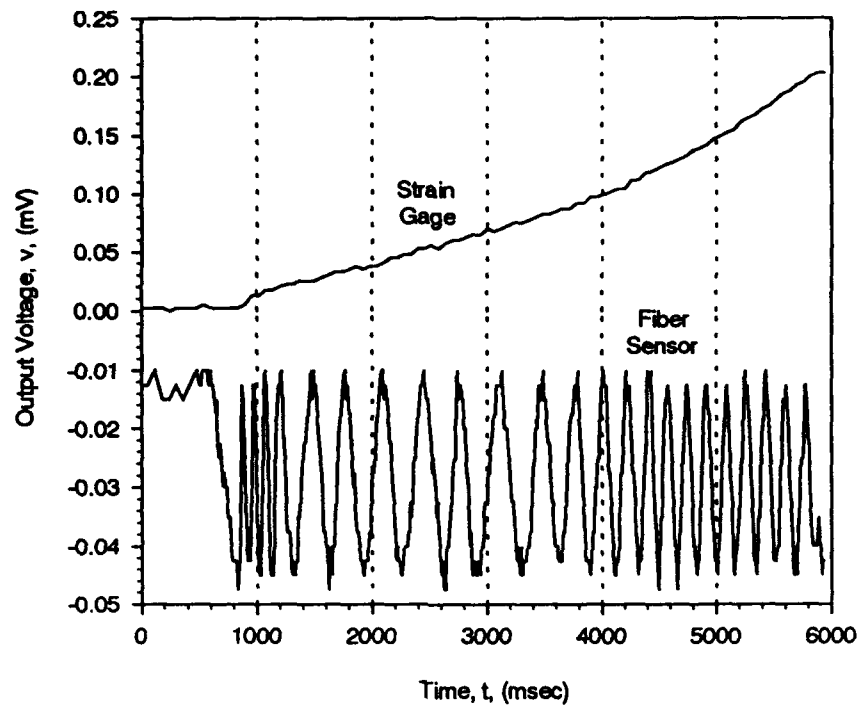


Figure 2.8. Typical output from the strain gage and the fiber optic sensor during tension testing.

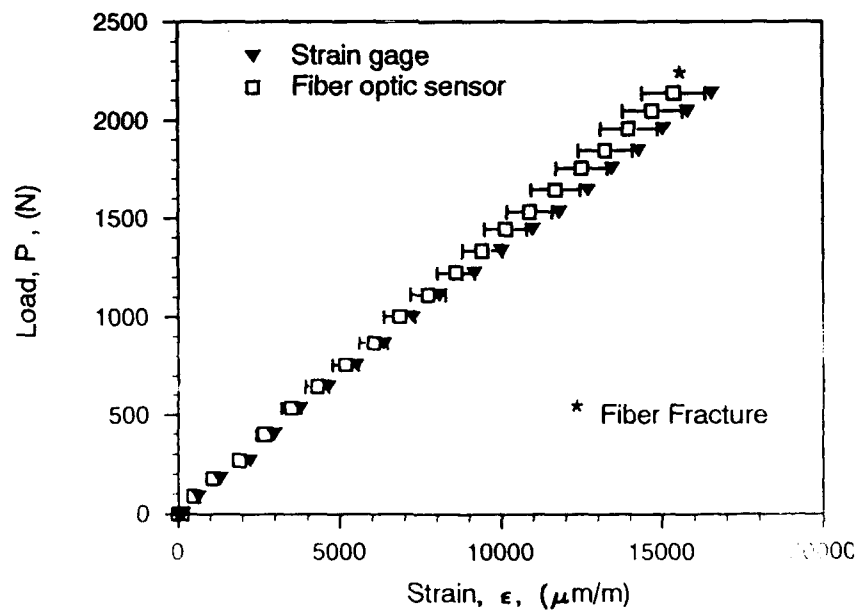


Figure 2.9. Typical strain data obtained from the strain gage and the fiber optic sensor.

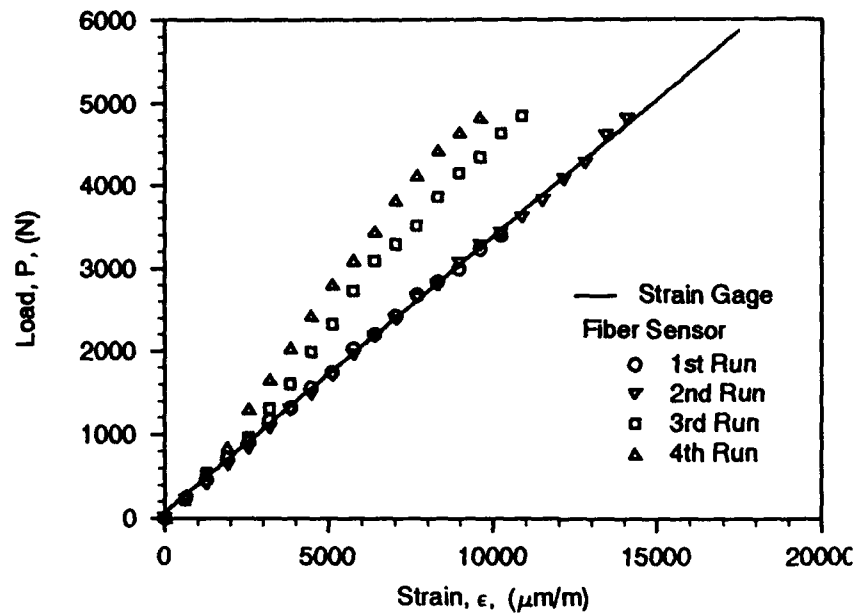


Figure 2.11. Strain gage and fiber sensor data from an incremented experiment showing the effect of fiber delamination.

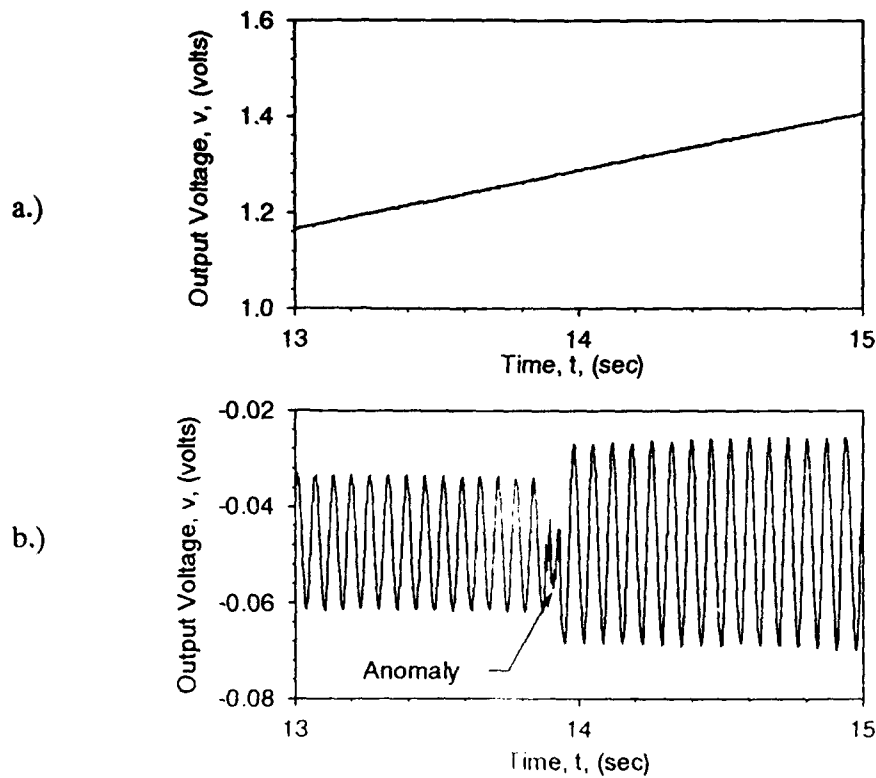


Figure 2.12. Output from both the a.) strain gage, and b.) the fiber sensor which has begun to delaminate (taken from 2nd run).

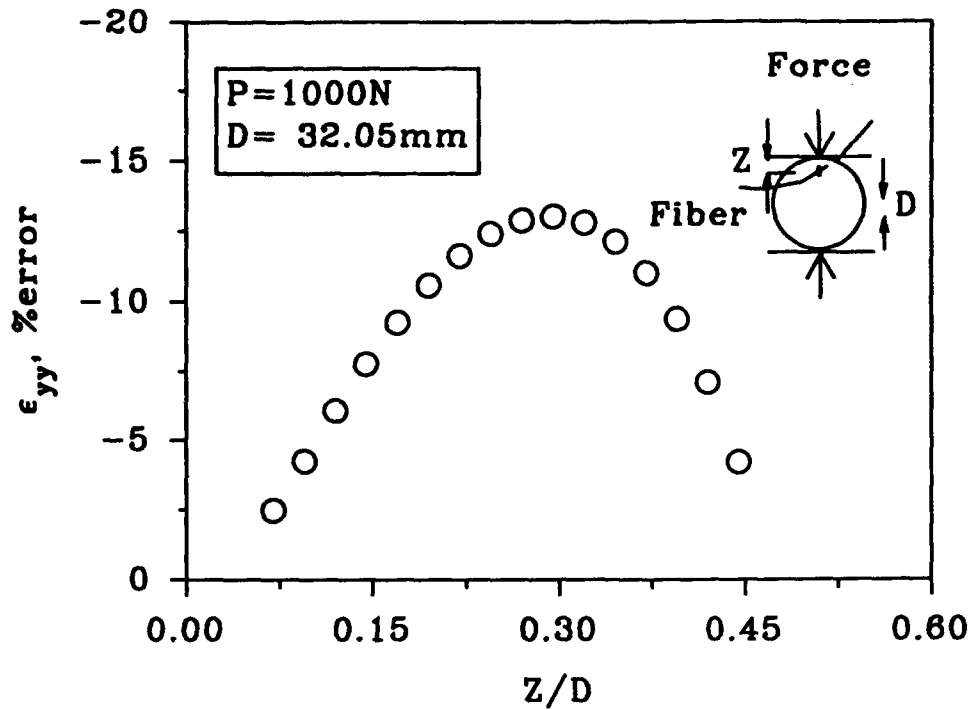


Figure 2.13. Plot of percent error in transverse strain as a function of sensor position and disk diameter due to the far field load.

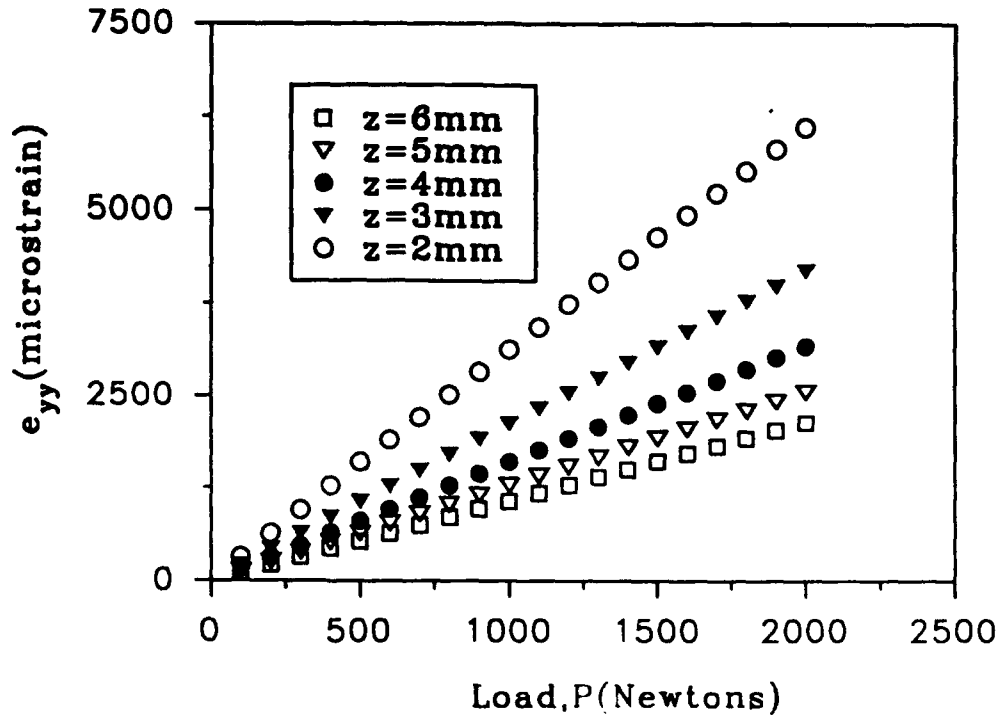


Figure 2.14. Plot of theoretical transverse strain vs. contact load for two 25.4 mm diameter Homalite 100 disks in contact.

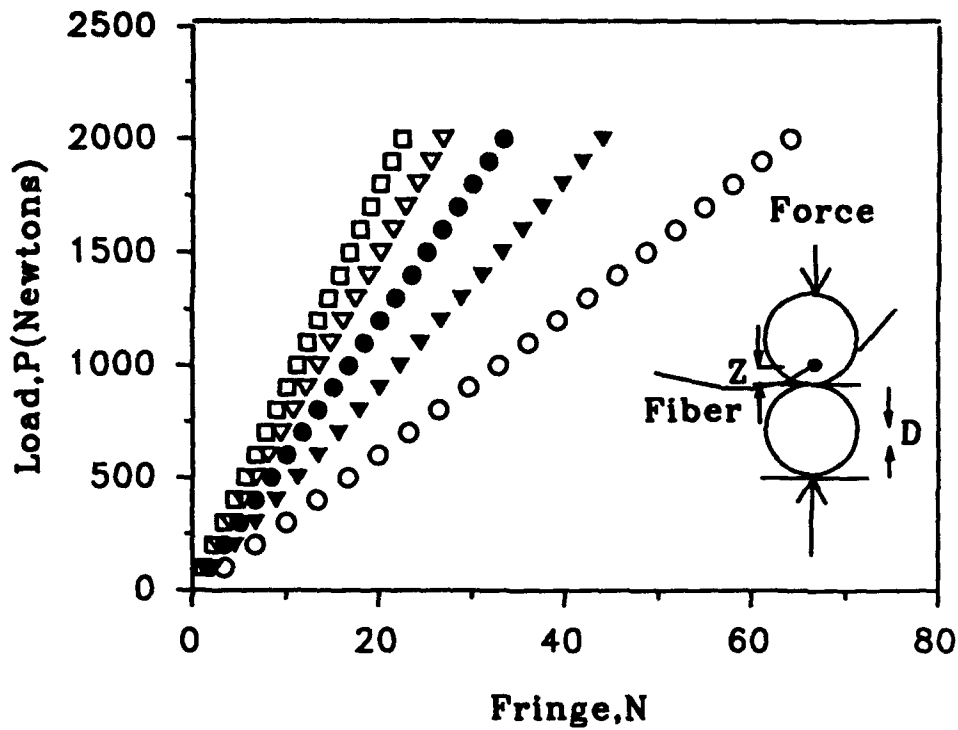


Figure 2.15. Plot of theoretical contact load vs. fiber optic sensor fringe number for two 25.4 mm diameter Homalite 100 disks in contact.

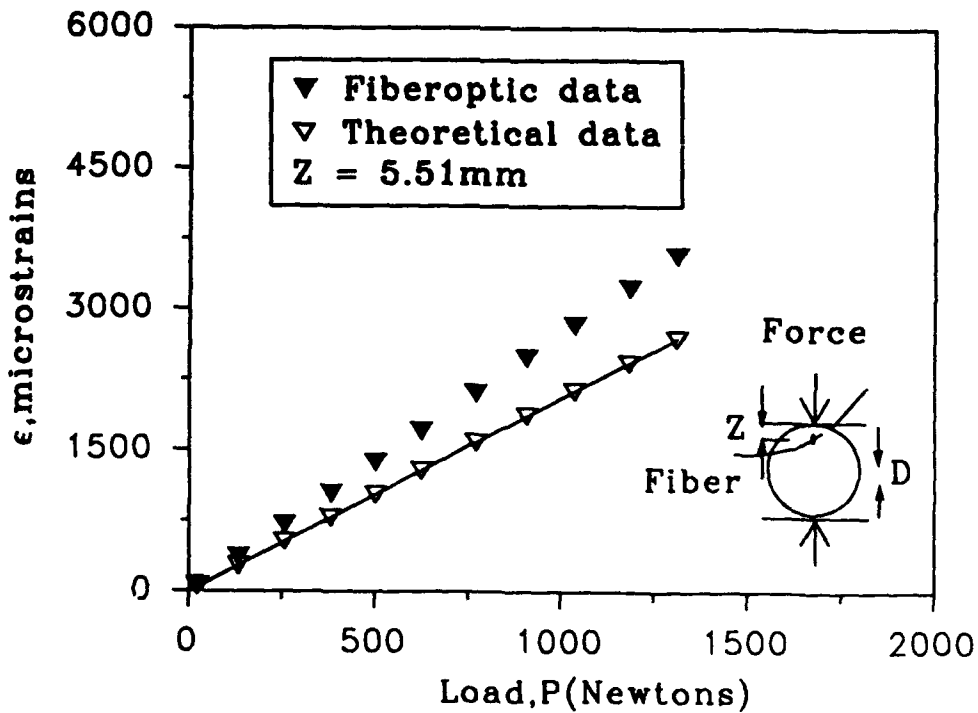


Figure 2.16. Plot of theoretical strain and strain from an embedded sensor vs. load for the disk under diametral compression.

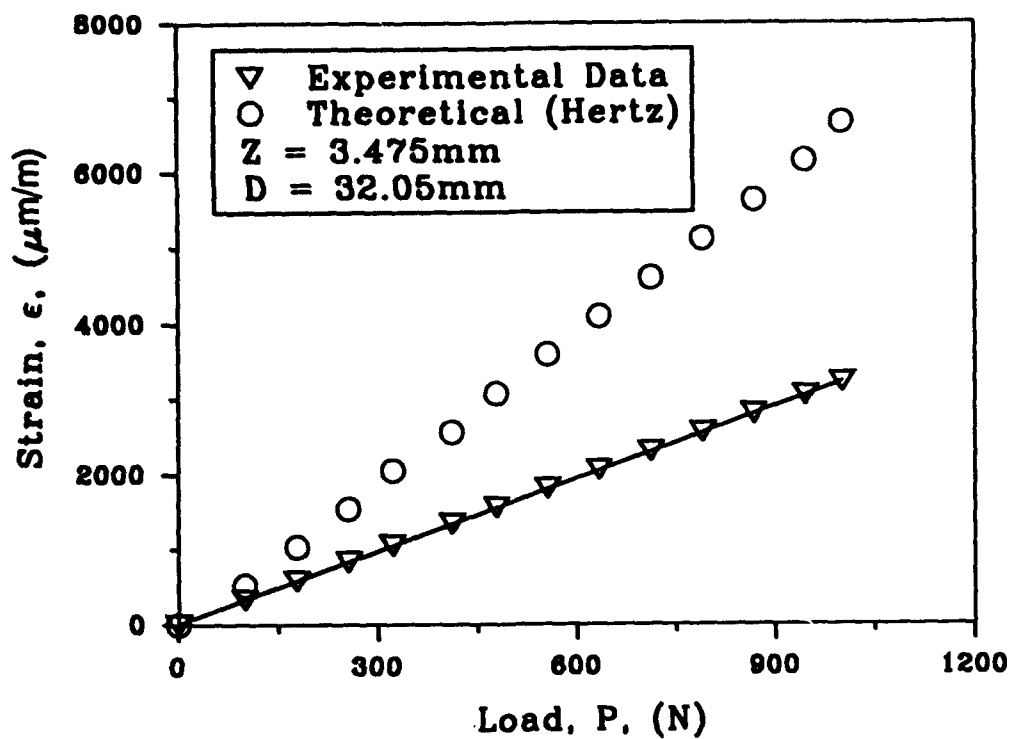


Figure 2.17. Plot of theoretical strain and experimental strain from a fiber optic sensor for a disk under diametral compression.

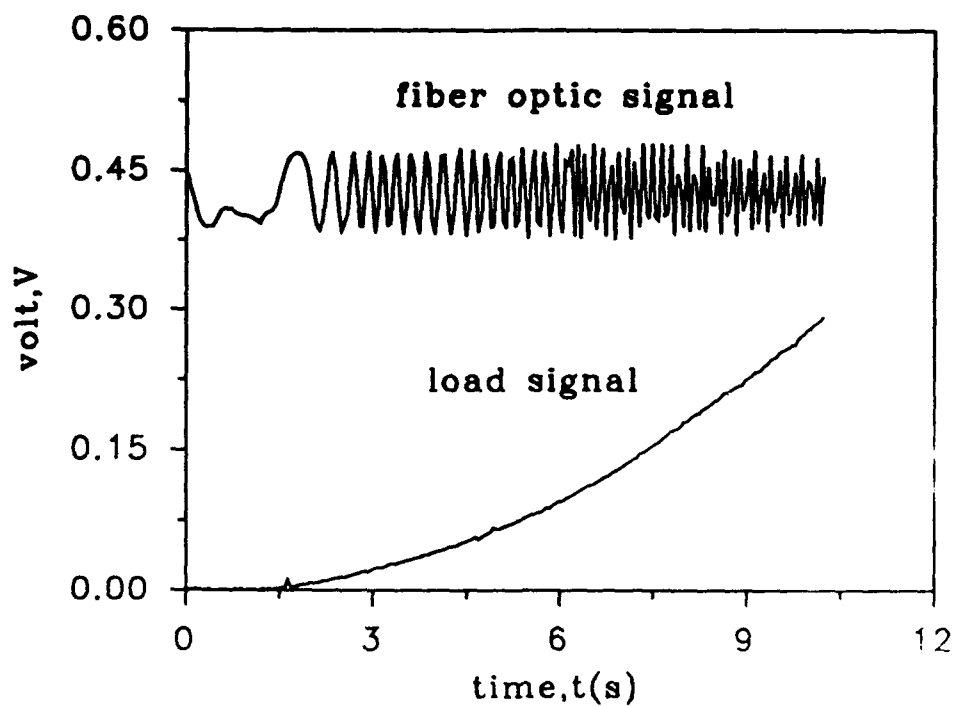


Figure 2.18. Typical output from the load cell and the fiber optic sensor for the disk under diametral compression.

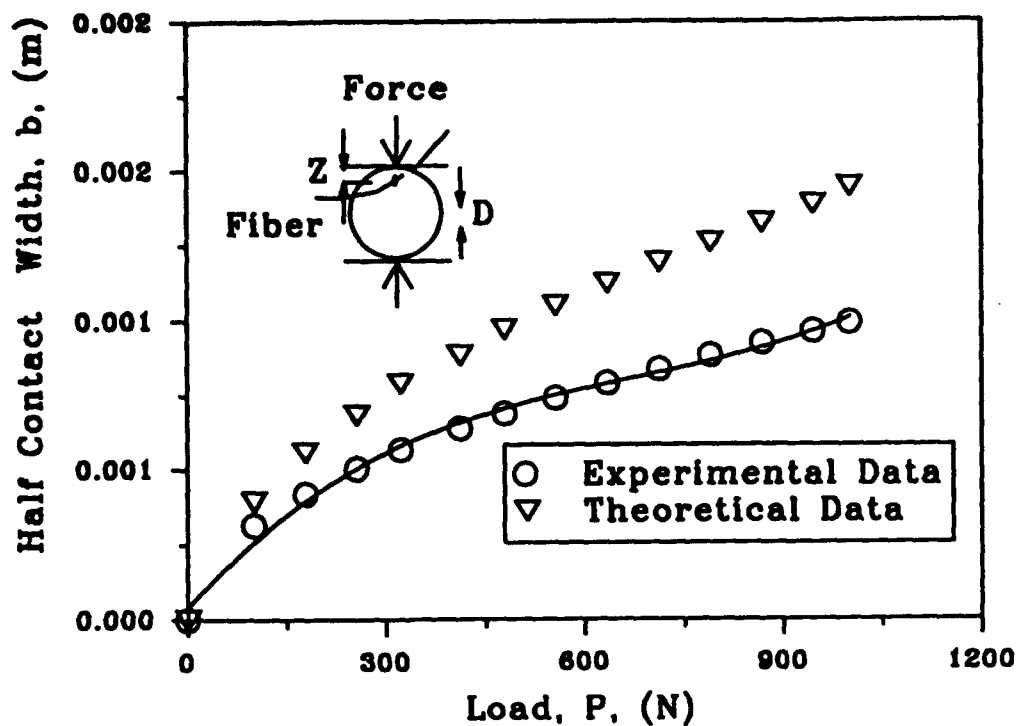


Figure 2.19. Plot of half contact width, b , vs. load for a Plexiglass[®] disk under diametral compression.

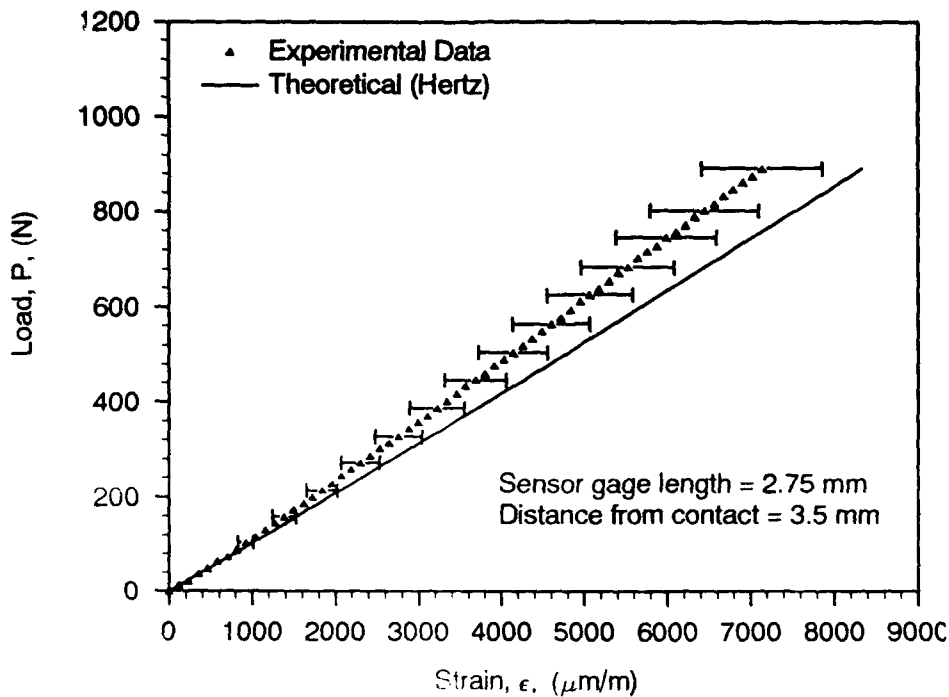


Figure 2.20. Typical data from the surface attached Fabry-Perot sensor as compared to theoretical values

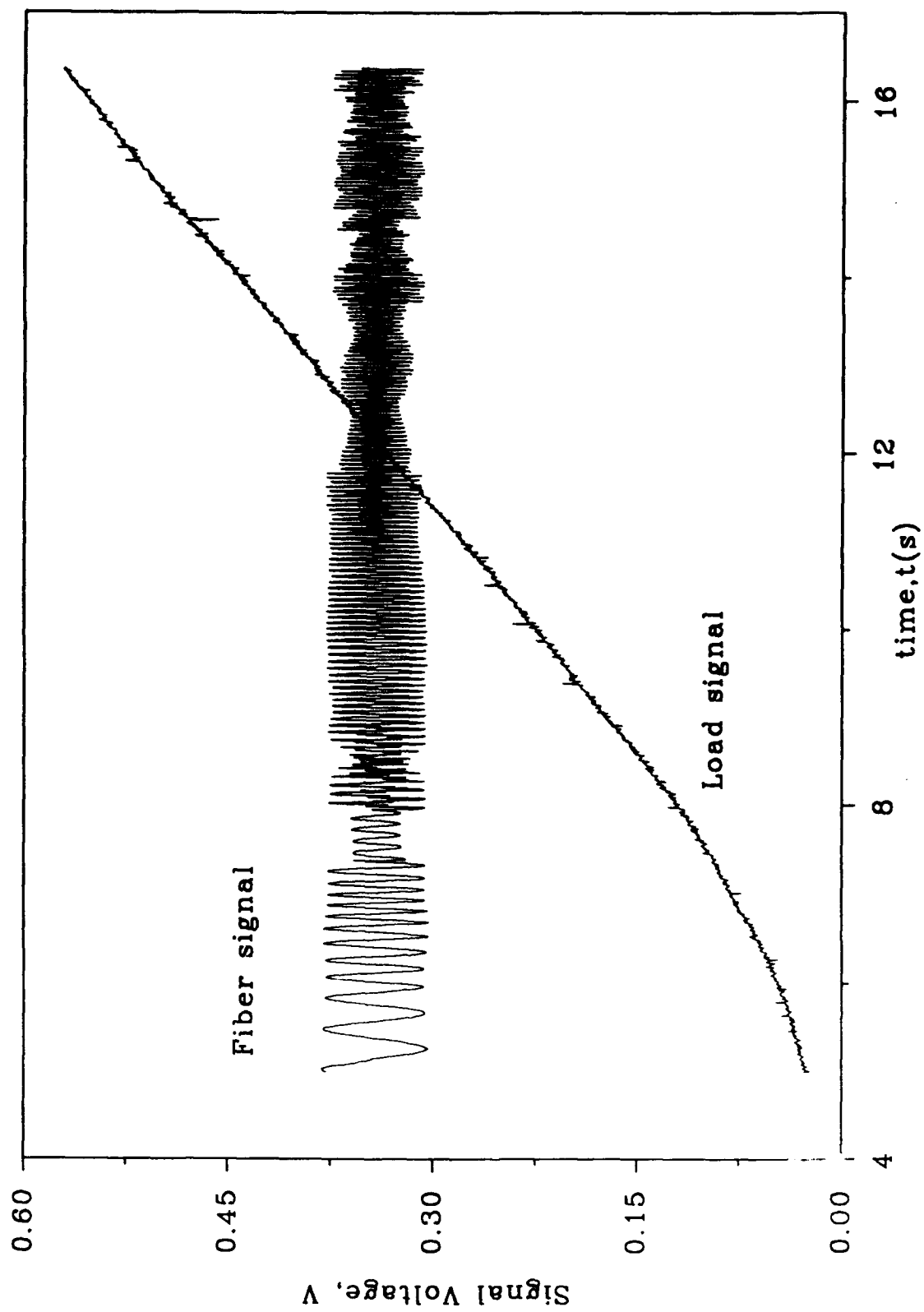


Figure 2.21. Typical output from the load cell and the fiber optic sensor for the sphere under diametral compression.

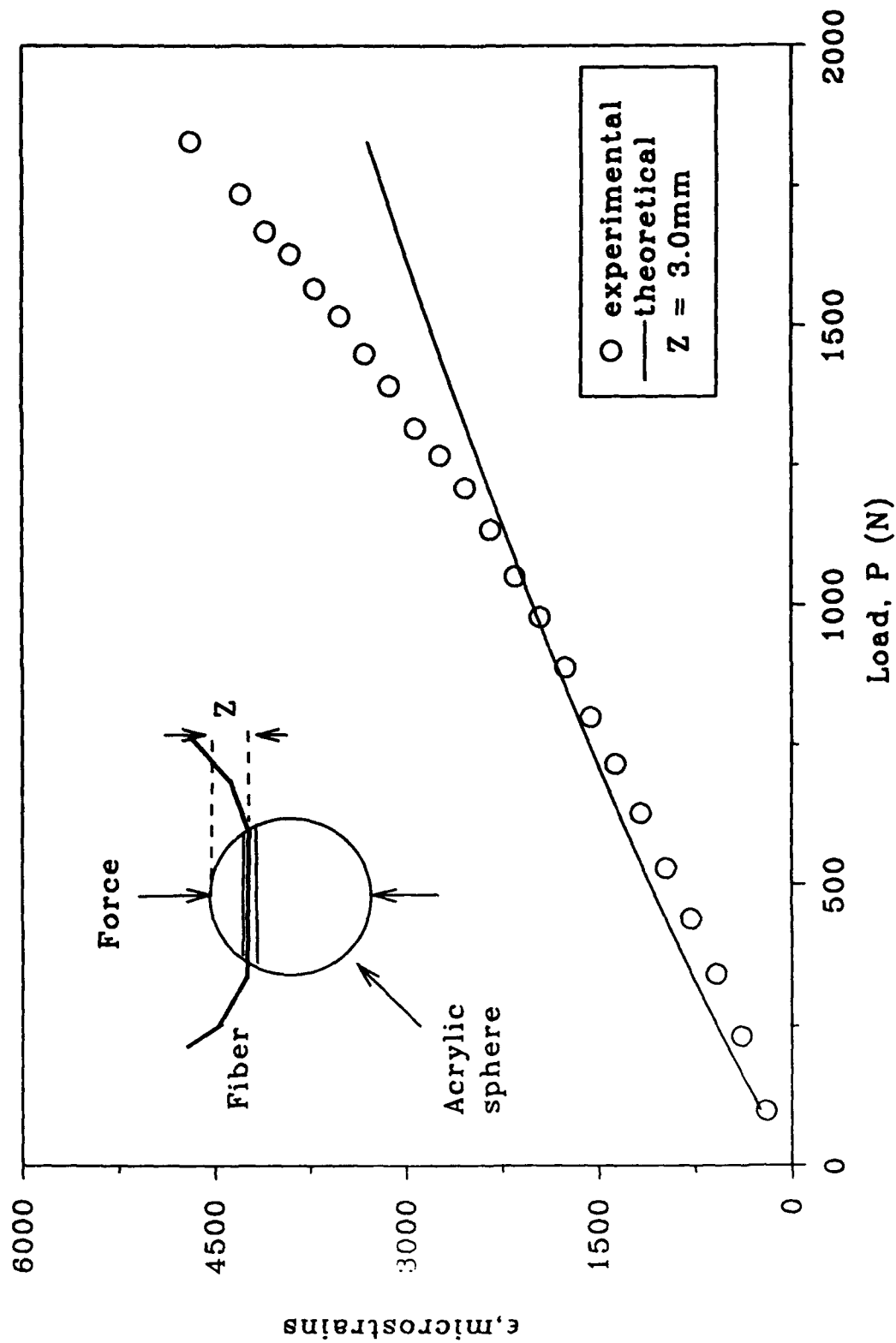


Figure 2.22. Plot of radial strain vs. compressive load for a 25.4 mm Plexiglass[®] sphere under diametral compression.

CHAPTER 3

APPLICATION OF WHITE LIGHT SPECKLE PHOTOGRAPHY TO MEASURE RIGID BODY DISPLACEMENTS AND DEFORMATIONS

This chapter presents the technique of white light speckle photography with the intention of using it to measure displacements around contacting particles. Results from preliminary experiments are also presented and discussed.

3.1 Introduction

3.1.1 History of Speckle like Phenomena

When a beam of light is passed through an isotropic transparent medium, light is scattered from each point along its path. This scattering process occurs because of inherent optical roughness, in other words, small particles in suspension inside the material. This scattering of light is very essential for the working of the speckle technique. The history of speckle like phenomena predated the laser but engineering application of speckle techniques started only after the development of the laser. The term 'speckle' originated as a result of holography when dark spots of destructive interference were observed in holograms. All the speckle techniques differ only in the nature of the speckle pattern generation. A double exposure of the speckle pattern, one before deformation and one after, is a common denominator to all speckle techniques. Leendertz (1970) established the foundation principles of speckle interferometry. Archbold and Ennos (1972) and later Duffy (1974) proposed a different technique known as speckle

photography which involved the use of a single divergent laser beam and recording double exposed photographs of the speckle patterns. Barker and Fourney (1976) showed the successful use of this technique for interior displacement measurements. Of late, speckle photography using ordinary whitelight has been developed by Chiang (1979, 1980, 1990) and Asundi (1982, 1983) which has opened a wide range of possibilities for the application of this technique.

3.2.2 Formation of 'Speckle'

When light from a coherent source such as a laser falls on an optically isotropic medium, scattering of the laser light occurs due to the optical roughness of the medium. This scattered light travels different paths and hence they interfere with each other forming bright and dark spots of constructive and destructive interference giving a speckle like appearance. These spots are called 'speckles'. This scattered light speckle pattern acts like a random grid and if the deformation is sufficient to cause a shift of the speckle pattern by at least one speckle diameter, the double exposed speckle pattern will behave like a complex diffraction grating. Speckle size can be calculated using the Rayleigh criterion. This gives an average diameter in the image plane of $s=1.2\lambda F$ (Barker and Fourney, 1976) where F is the aperture ratio of the lens. Corresponding speckle size in the object is given by

$$s=\frac{1.2\lambda F}{m} \quad (3.1)$$

where m is the magnification.

3.2 Speckle Techniques

3.2.1 Speckle Interferometry

When two optically interfering beams of light are used to generate a speckle pattern, the technique is called speckle interferometry. The two sources of optically interfering beams can be a laser in combination with an appropriately placed mirror which causes a phase difference necessary for interference.

3.2.2 Speckle Photography

Speckle photography uses a single beam of light to generate a speckle pattern. When a laser is used as the source of light, a speckle pattern is generated due interference between the scattered light inside the material. This technique is called laser speckle photography. When a speckle pattern is artificially created and ordinary light is used, it is called whitelight speckle photography.

3.3 Theory of Fringe Formation in Speckle Photography

Speckles are formed due to random interference of coherent light from different scattering sites within the propagating medium. The intensity of an individual speckle is independent of the intensity of the illuminating light and depends only on the relative phase of the light from each scattering site within a speckle cell. Hence, it is unimportant if the phase of the illuminating light or the light scattered from each speckle cell changes between exposures due to material birefringence or deformation of the body. The double exposed negative of the speckle pattern or specklegram, as it is called, behaves like a complex diffraction grating. When a laser light is passed through this grating, light is

scattered into a diffraction halo with intensity varying across the field. The diffraction pattern is due to the product of the diffraction halo of a single speckle pattern and the intensity distribution generated by two point sources spaced a distance apart equal to the image shift. Sensitivity is governed by the Rayleigh's criterion and the maximum displacement that can be measured is governed by speckle pattern correlation. Excessive deformation moves new scattering sites into and old scattering sites out of the illuminating light. Decorrelation can also occur due to a displacement gradient normal to illuminating sheet.

The basic optical configuration incorporating a single beam laser speckle method can be described as follows. An object surface is illuminated by a laser beam. The location of the light source is denoted as S and P is a point on the surface of the illuminated body. The recorded light intensity of the first exposure is (Kobayashi, 1987)

$$I_1 = B^2(x, y) \quad (3.2)$$

If the body is deformed between exposures, the image on the film plane will be shifted to new coordinates x' and y' . The light amplitude in the deformed configuration may be written as

$$I_2 = B^2(x', y') \quad (3.3)$$

The surface displacement vector PP' may be expressed as

Then the film plane displacement vector can be written as

$$PP' = u_p e_x + v_p e_y + w_p e_z \quad (3.4)$$

$$PP'_{film} = m[u_p e_x + v_p e_y] \quad (3.5)$$

where m is the magnification of the lens.

Coordinates of the film plane for the second exposure are $x' = x + u_f$ and $y = y + v_f$. Now the expression for the total intensity is expressed as

$$I_{total} = B^2(x, y) + B^2(x + u_f, y + v_f) \quad (3.6)$$

Interference fringes are obtained by taking optically the Fourier transform of the amplitude transmission function of the processed photographic negative. The amplitude transmission function $g(x, y)$ is assumed linear in the ranges of interest and may be expressed as

$$g(x, y) = a + bI_{total} \quad (3.7)$$

where a and b are constants.

It can be proved that the intensity in the transform plane can be written as

$$I(\omega_1, \omega_2) = C[(1 + \cos(\bar{\omega}u_p))] \quad (3.8)$$

where C is a constant and ω is the spatial frequency variable and is denoted as

$$\bar{\omega} = \omega_1 e_{xs} + \omega_2 e_{ys} \quad (3.9)$$

and

$$\omega_1 = \frac{KX_s}{d} \quad \omega_2 = \frac{KY_s}{d} \quad (3.10)$$

where X_s and Y_s are the coordinates in the transform plane and $K = 2\pi/\lambda$. Fringes will be

defined when $I(\omega_1, \omega_2) = 0$ i.e when $1 + \cos(\omega u_p) = 0$.

For a small region of illumination, the displacement is assumed constant and fringes are formed when

$$\overline{\omega} u_{pf} = (2n - 1)\pi \quad n = 1, 2, 3, \dots \quad (3.11)$$

In general, only the first fringe is observed i.e $n = 1$, therefore written as in equation (3.12), where d is the distance between the transform plane and the specklegram.

$$X_s u_{pf} + Y_s v_{pf} = \frac{\lambda d}{2} \quad (3.12)$$

To find the component of displacement along Y_s , we take $X_s = 0$ and we get $v_{pf} = \lambda d / 2Y_s$ and similarly $u_{pf} = \lambda d / 2X_s$. Now the magnitude of total displacement is given by

$$U = \sqrt{u_{pf}^2 + v_{pf}^2} \quad (3.13)$$

Substituting values of the components, we get U as equation (3.14),

$$U = \frac{\lambda d}{S} \quad (3.14)$$

where S can be calculated as shown in equation (3.15).

$$S = \frac{2X_s Y_s}{\sqrt{X_s^2 + Y_s^2}} \quad (3.15)$$

In case of a magnification while recording the specklegram, U should be written as

$$U = \frac{m \lambda d}{S} \quad (3.16)$$

3.4 Experimental Procedure and Data Analysis

In all speckle techniques, a double exposure of the speckle pattern is made, one before deformation and one after, on a special kind of film called the litho ortho type. These litho films are a go-nogo kind of film which means that beyond a certain intensity threshold, they will print as black and below the threshold, they do not print at all. In the case of laser speckle, a laser source is used to generate the speckle pattern. In the case of whitelight speckle, light from a Tungsten filament can be used to project on the artificial speckle pattern. Fig. 3.1 shows the schematic for recording a whitelight specklegram. These artificial speckle patterns can be a rough surface, white paint sprayed on a black base or a coating of retroreflective paint. For interior measurements, glass beads can be mixed while casting the material. A double exposure of this speckle pattern is recorded, one before deformation and one after deformation. This double exposed speckle pattern is called a specklegram. Data analysis can be done by applying either the pointwise filtering technique or the whole field filtering technique. When a laser beam is passed through any point inside this specklegram, Young's fringes are seen. This is the pointwise filtering technique. The spacing between the fringes is related to the displacement of the point of interest as shown before and is given by equation (3.14). Fig. 3.2 shows this analysis setup which is called the pointwise filtering technique. When an optical filter with a pin hole is used for analysis of the specklegram, whole field displacement information can be obtained. In this case, isothetic fringes or fringes of constant displacement are seen and the analysis is termed whole field filtering. The former technique, though tedious, is more precise and can be automated. A computer in combination with a digital filter and a CCD sensor can be used to filter the noisy speckle

data and give accurate displacement values at different points in the model (Chitsaz and Moslehy, 1989).

3.5 Results and Discussion

Experiments were done to measure the surface displacements at various points in a plexiglass disk of 63.2 mm diameter subjected to rigid body displacement. The disk was painted black and then sprayed white to give a speckle pattern with an average speckle size of around 100 μm . The disk was then mounted on a horizontal translator which in turn was mounted to an optical bench. 2X90 W Tungsten lamps were used to project light on the specimen. Double exposure of the speckle pattern was made on a Kodalith ortho type 3 film using a 4"X5" field view camera. In between the double exposures, a rigid body displacement of 400 μm was given to the specimen. The film was developed in Kodalith Super-RT developer. The specklegram was analyzed using the pointwise filtering technique. A 1 mW He-Ne laser was used for the analysis. Fig. 3.3 shows typical Young's fringes and Fig. 3.4 shows the displacements calculated at various points on the body. The calculated displacements compare well with the actual displacement of 400 μm . Most of the measured displacements lie within 10% accuracy. Accuracy could be improved considerably by increasing L, the distance between the laser/specklegram and the viewing screen, especially in the case of manual measurement of fringe spacing, S.

Experiments were also done using 25.4 mm diameter plexiglass disks under diametral compression using the crosshead of an Instron machine. The speckle generation was the same, but the fringe formation was extremely hazy and unclear making data acquisition virtually impossible.

Experiments were also done with embedded speckles. A three dimensional body was made out of a polymer resin with speckles casted inside using retroreflective paint. The experimental procedure was the same but the fringes again were very hazy and difficult to analyze.

Speckle techniques are powerful means for the non destructive evaluation and testing of critical components. They have been used quite extensively in the turbine industry. These techniques are especially suitable for measuring interior displacements which is a limitation of most techniques. For all its merits, the technique has its limitations too. Decorrelation of the speckle patterns is a inherent problem of laser generated speckle patterns. This can be avoided by using whitelight speckle photography. White light speckle technique makes it possible to measure displacements at any predetermined point of the body while avoiding speckle pattern where not required. The noisy speckle data, which is a inherent defect of all speckle technique can be analyzed accurately by using a digital filter. Moreover, changing the white light source to an ultra violet source might improve the fringe pattern as has been observed by some researchers.

3.6 Conclusion

The conclusions that were drawn from the speckle experiments can be summarized as follows:

- Laser speckle photography can be used to measure displacements on the surface of a body although decorrelation of speckle patterns is a problem.
- White light speckle photography is able to measure rigid body displacements on the surface of a body within 10% accuracy.

- Noisy speckle patterns were observed while analyzing speckle patterns of specimens subjected to deforming forces and embedded speckles. This problem might be solved by a digital filter and by changing the source of whitelight.

Currently, experiments are being designed using more powerful whitelight sources and digital filters to analyze the speckle data. The aim is to embed these speckles and gather displacement information at different interior points in the body.

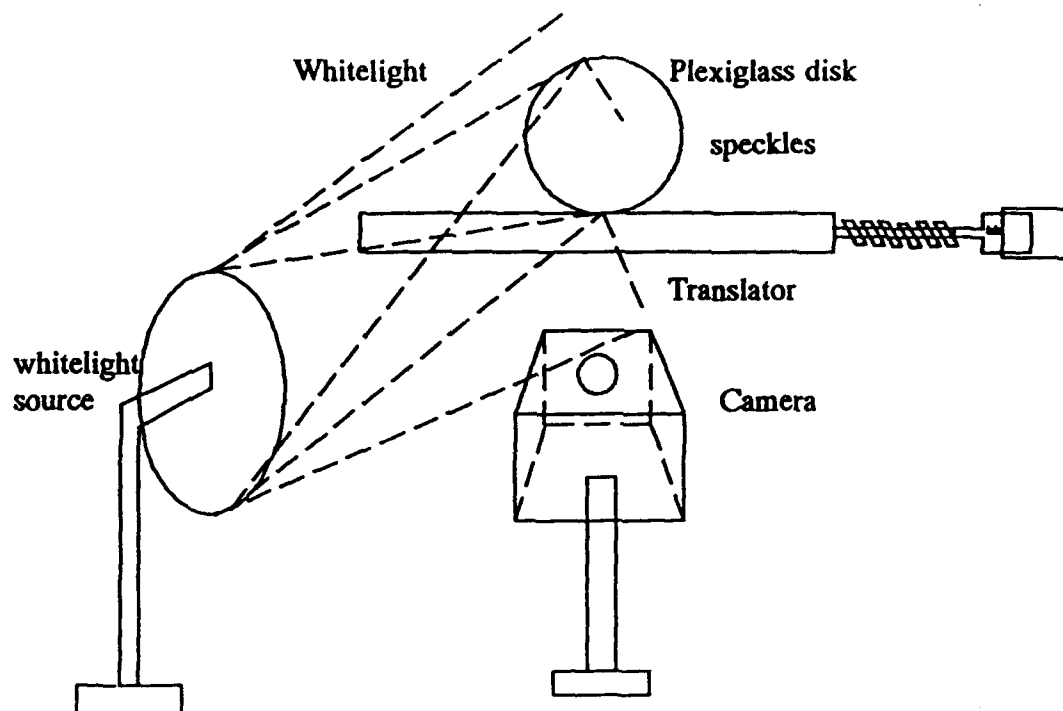


Fig. 3.1. Experimental setup for measuring rigid body displacement using white light speckle photography.

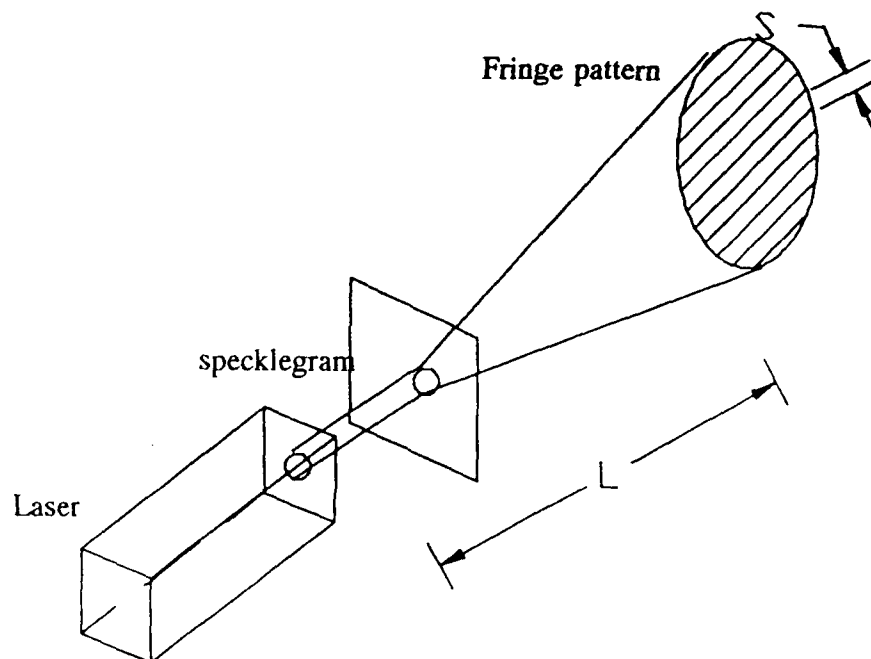


Fig. 3.2. Data analysis setup used to measure rigid body displacements in a plexiglass disk.

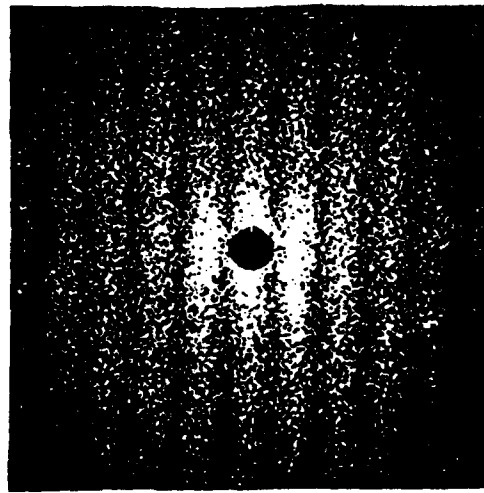


Fig. 3.3. Typical Young's fringes for a white light speckle photographic experiment.

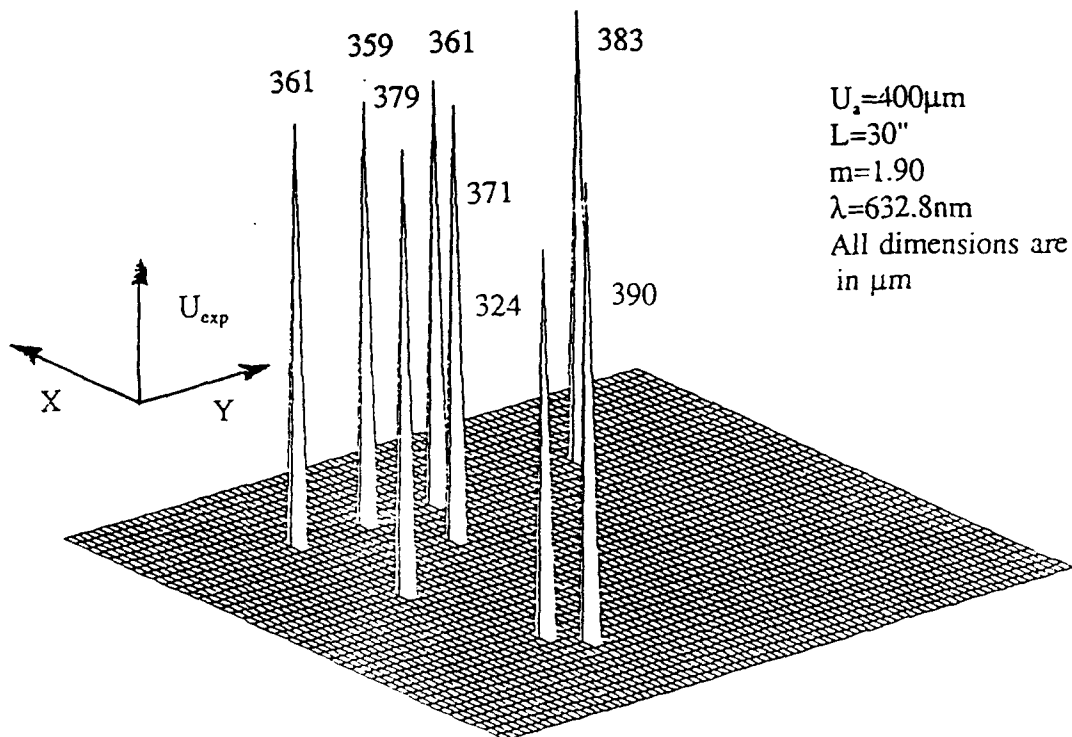


Fig. 3.4. Experimental white light speckle photographic data for a rigid body displacement of $400\mu\text{m}$.

CHAPTER 4

PRELIMINARY STUDY OF THE EFFECT OF CEMENTATION

ON

THE DYNAMIC LOAD TRANSFER PHENOMENON

4.1 Introduction

This chapter represents a preliminary attempt at studying the effect of cementation on the wave propagation phenomenon. Dynamic wave propagation has been studied in recent years for its importance in such diverse applications as dynamic compaction of powders, shock forming of modern composites, and in various shock absorbing and isolating applications. These studies have primarily looked at the particle to particle interaction of dry contacts. While this may apply to the fore-mentioned applications, the study of seismic phenomenon needs to account for other parameters. One of these parameters is cementation between particles.

Predominantly the studies to date have been based on the classical approach to solutions for normal compression of disks and spheres(Johnson, 1985). This approach addresses the problem by modeling the contact as that between two elastic bodies where the contact zone dimension varies with varying force. If cementation is considered, the most significant difference is that the contact zone dimension is fixed by the amount of cementation and does not vary during the application of force.

In nature there are many instances of cementation between particles. Probably the most common example of cementation occurring naturally is sedimentary rock. Man-made examples include such things as concrete and asphalt. By studying the effect of

cementation on the stress wave, we can gain a greater insight into seismological events and structural design. Experimental data and observations are needed as input parameters for numerical simulations of wave propagation in cemented particulate materials. Ultimately, safer design and construction will result.

4.2 Theoretical Analysis

The primary analysis technique utilized by this laboratory is an overdeterministic least square method to determine contact parameters from digitized photoelastic fringe pattern data. The theoretical equations are based on Hertz contact theory. The equations for the stresses were given in Chapter 2 but are expanded here to include the friction factor, β .

$$\sigma_{zz} = -\frac{b}{\pi\Delta} [z(b\phi_1 - x\phi_2) + \beta z^2\phi_2] \quad (4.1)$$

$$\begin{aligned} \sigma_{xx} = -\frac{b}{\pi\Delta} & \left[z \left(\frac{b^2 + 2z^2 + 2x^2}{b} \phi_1 - \frac{2\pi}{b} - 3x\phi_2 \right) \right. \\ & \left. + \beta \left((2x^2 - 2b^2 - 3z^2)\phi_2 + \frac{2\pi x}{b} + 2(b^2 - x^2 - z^2)\frac{x}{b}\phi_2 \right) \right] \end{aligned} \quad (4.2)$$

$$\sigma_{zx} = -\frac{b}{\pi\Delta} \left[z^2\phi_2 + \beta \left((b^2 + 2x^2 + 2z^2)\frac{z}{b}\phi_1 - 2\pi\frac{z}{b} - 3xz\phi_2 \right) \right] \quad (4.3)$$

The terms ϕ_1 and ϕ_2 are given by the following

$$\phi_1 = \frac{\pi(M + N)}{MN\sqrt{2MN + 2x^2 + 2z^2 - 2b^2}} \quad \phi_2 = \frac{\pi(M - N)}{MN\sqrt{2MN + 2x^2 + 2z^2 - 2b^2}}$$

$$M = \sqrt{(b + x)^2 + z^2} \quad N = \sqrt{(b - x)^2 + z^2}$$

The term Δ is a parameter that is dependant on the material elastic properties, E and ν , and the radii of curvature of the two objects in contact, and is given in equation (4.4).

$$\Delta = \frac{1}{\left(\frac{1}{2R_1}\right) + \left(\frac{1}{2R_2}\right)} \left(\frac{1-\nu_1^2}{E_1} + \frac{1-\nu_2^2}{E_2} \right) \quad (4.4)$$

These expressions for the stress field are combined with the stress optic law which is shown as equation (4.5),

$$\sigma_1 - \sigma_2 = \frac{Nf_\sigma}{h} \quad (4.5)$$

where N is the fringe number, f_σ is the stress optic coefficient for the material, and h is the thickness of the specimen.

Twenty data points are used to determine the two unknowns, b and β . Once the two unknowns have been found, the half contact width and the friction factor, β , are used to back calculate the normal and tangential contact loads.

4.3 Experimental Procedures and Results

Due to the nature of the cemented contact, static experiments were conducted to determine whether or not the Hertz contact theory would be valid for cemented particles. As mentioned previously, the analysis technique utilized by this laboratory is an overdeterministic least square technique in conjunction with the Newton-Raphson method

to determine contact parameters such as normal load, half contact width, b , friction factor, β , and tangential load, based on Hertz contact theory. The theory relates the contact load to the contact width. Unlike two particles in contact without cementation where the contact width can vary with the load, cemented particles have a fixed contact width.

Static photoelastic experiments were conducted using two circular particles, made of Homalite-100, that were cemented together with a cyanoacrylate based adhesive. The disks were then loaded in an Instron testing machine and photographs were taken through a circular polariscope and a monochromatic lens, at various load levels. Fig. 4.1 shows typical isochromatic fringes for two disks with a cemented contact, under diametral compression. The top and bottom contacts are Hertz contacts and the disk to disk contact is the cemented contact.

Looking at the fringes very close to the cemented contact, the fringes show the effect of the cementation. Further away from the contact the fringes are very similar to the Hertz fringes. It is this similarity that was hoped to be utilized in later dynamic experiments.

The disturbance to the fringes at the contact point seems to agree well with the numerical calculations made by Dvorkin *et. al.* (1991). The numerical work predicted that for very stiff cements (stiffness of the cement is expressed with respect to the particle stiffness) the profile of the force distribution would result in the maximum normal forces at the edges of the cemented zone. Dvorkin also calculated the normal force distribution for soft cements. For this case the force distribution was just the opposite, the maximum normal force would fall in the center of the cemented zone. Fig. 4.2 shows the force distributions, on the vertical axis, as predicted by Dvorkin. The parameter, m , is the ratio

of the cement stiffness to the grain, or particle, stiffness. The horizontal axis represents distance along the particle surface from the center of the contact to the edge of the cemented region, ie. $0 \rightarrow b$.

Static photoelastic experiments were designed to verify these predictions. The disks were machined of PSM-1, a photoelastic plastic, which has a low stress optic coefficient, f_{σ} . The stress optic coefficient determines the order of the fringes produced by a given load. The higher the stress optic coefficient, the lower the fringe order seen for a given load. (The lower the stress optic coefficient, the higher the fringe order for the same load.) The PSM-1 was chosen so that under very small loads, an appreciable number of fringes would still be seen.

The experiment called for a uniform loading conditions on both sides of a disk so three disks were used. The center disk would experience a distributed load on both sides, while the two outer disks experience a point loading on one side and a distributed loading on the other. To fabricate the specimens, the cement materials were either cast from a liquid into the gap between the disks, in the case of the soft cement, or machined from a solid piece and 'glued' into the gap, for the stiff cement. The procedures will be described below.

The soft cements were Hexcel urethanes of varying stiffness that were mixed from two liquid components and poured between the two disks. The disks were adhered, face down, to a sheet of plastic with the desired gap between them and the width of the cementation zone was fixed by placing two blocks against the disk edges. The area was sealed with silicone caulk and the urethane was cast into the resulting cavity.

For the stiff cements, a piece of aluminum was machined into the same shape as

the cast urethane. The aluminum 'cement' was then bonded to the PSM-1 disks using a photoelastic adhesive. The adhesive cures to the same mechanical properties as the PSM-1 and is also optically clear.

Fig. 4.3 and 4.4 show the typical isochromatic fringes obtained for static experiments involving large cementation zones and for different cement stiffness. Fig. 4.3 shows the fringes that result when the cement stiffness is very low compared to the disk stiffness. Notice that the fringes develop from the center of the cemented region. Just the opposite is seen for the case of the very stiff cement, Fig. 4.4. The fringes develop from the edges of the cemented region. Both cases confirm the numerical prediction made by Dvorkin. These fringes, however, are very different from Hertz fringes. It was seen that for cementation zones that were large, 20% of the particle diameter, and 3 mm wide, the fringe patterns deviated more from the Hertz patterns and Hertz analysis would not be appropriate.

The photographs from the static experiments using the Homalite-100 disks were analyzed for both the known Hertz contact and the cemented contact. These experiments involved a very thin cement layer and also the cemented region was not wide compared to the particle diameter (the cemented region was 10% of the particle diameter). It was hoped that the Hertz equations might be valid for some region and analysis could be performed using the previously mentioned scheme.

Typical plots showing the results of the analysis are shown in Fig. 4.5. The plots show the experimentally determined load, normalized by the Instron load cell data, vs. the normalized distance from the contact. The normalizing parameter for the distance from the contact was the half contact width, b , as taken from the Hertz contact. The data from

the Hertz contact is shown as solid circles and the dashed lines are the allowable experimental error. The Hertz data shows acceptable values within a region from about 2b to 8b. This agrees well with previous work (Shukla and Damania, 1988).

The data from the cemented contact shows some agreement with the Hertz data but the band at which acceptable values can be obtained is very narrow. At the highest load, 2220 N, the data falls within the acceptable error between approximately 5b and 7b. For lower loads, however, the acceptable region shifts to higher multiples of the half contact width, b.

The narrowness of the band, as compared to the Hertz data, also raises some concern. If the valid region for analysis is too narrow and shifts with the applied load, the usefulness of the analysis technique may be in question. However, it should be noted that the data presented does not represent a complete study and further work will be done in this area. An acceptable region may be found that will allow analysis of the isochromatic fringes.

Following the static experiments, dynamic experiments were begun. A single chain of cemented particles was placed in the camera and an explosive charge was detonated to initiate the stress wave. Fig. 4.6 shows typical photographs of the disk chain as the dynamic wave propagates. From the photographs, the pulse length can be directly measured and the group wave velocity can be determined. The pulse length is marked in the figure.

The pulse length, shown in Fig. 4.6, can be seen to be approximately four and one half particle diameters. This differs from findings reported in earlier work (for example: Shukla and Damania, 1987) where the pulse length consistently stabilized at four particle

diameters.

The group wave velocity was determined by measuring the position of the wave front at various times and plotting the distance propagated vs. time. Fig. 4.7 shows the plot for a number of single chain experiments of cemented particles in a vertical arrangement. The average velocity was determined to be 1240 m/s. This is higher than the reported velocity for a single chain of particles without cementation by approximately 20%. The velocity for particles without cementation was found to be approximately 1050 m/s.

Fig. 4.8 shows the normalized contact load vs. time for the single chain of cemented particles. Hertz analysis was used to acquire the load data presented and identical methodology was used for analyzing each of the contacts. The normalization removes the quantitative aspects and therefore the plot shows, qualitatively, the effect of the cementation on the contact load. The plot shows that across four particle contacts, there is no significant attenuation of the contact load. This matches the results for a single chain of particles without cementation.

Experiments were also conducted with the particles staggered from the vertical, by some angle, α . Fig. 4.9 shows the particle arrangement for the staggered configuration. To date, only two different angles, $\alpha = 15^\circ$ and $\alpha = 40^\circ$, have been used in the experiments. Fig. 4.10 and 4.11 show the typical isochromatic fringes obtained using these particle arrangements.

The wave speeds have been determined and are shown in Fig. 4.12. These velocity measurements represent the vertical velocity of the wave front as it propagates in the chain. Since the data only represents a few experiments, the reported velocities are still

considered estimates. The trend however would lead one to believe that the greater the angle, the lower the wave velocity. It is difficult to discuss pulse length in terms of particle diameters but it is easy to see that the pulse is loading approximately 6 particles in Fig. 4.10, the 15° angle case, and 5 particles in Fig. 4.11, the 40° angle case.

Notice that there was energy still propagating in the particles (this is most noticeable for the 40° angle case) after the main pulse had passed. This energy is due to reflections taking place in the particles and presumably would lead to greater attenuation of the pulse. Evidence of this can be seen in Fig. 4.11. The magnitude of the fringe orders seen in the photographs decreases dramatically as the loading pulse travels down the chain. As complete confidence in the current analysis technique has not yet been established, no load data will be presented at this time.

Another set of experiments, still in the preliminary stages, is the investigation of stress wave propagation at angles of 90° and greater from the incident wave direction. The particles in these experiments were cemented together. Fig. 4.13 shows typical isochromatic fringes from such an experiment. Note that in previous work by members of this laboratory (Shukla et. al., 1988) the wave would not propagate at angles of 90° or greater using uncemented particles.

Fig. 4.13 shows that energy does indeed transfer to the particle chain that is at a right angle to the incident pulse. A careful look at these photographs reveals that damage growth has begun in the first disk in the right angle chain. The stress on the contact is almost entirely shear stress and the damage originates at the edge of the cementation zone. The origin of the damage coincides well with the numerical predictions made by Dvorkin (1991) with regard to the maximum stress location for a cemented contact.

Velocity measurements were also made for the pulse propagating in the near vertical straight chain and it was found that the ratio of cementation width to particle radius, w/r , also has an effect on the velocity of the pulse. The velocity was found to be higher in this straight chain ($w/r = 0.12$), approximately 1330 m/sec, than that of the previous straight chain ($w/r = 0.10$), 1240 m/sec. The difference between the two chains was that the ratio, w/r , was higher in the chain with the higher velocity. Further experimentation will be done to explore this phenomenon.

4.4 Conclusion

Cementation proved to have an impact on the nature of wave propagation phenomenon. The velocity of the group wave as compared to uncemented contacts increased by approximately 20%, for vertical chains of particles. This preliminary work shows that although the group wave velocity and the pulse length seem to be affected, the contact load does not seem to show any appreciable attenuation in the straight particle chains.

The effect seen on the group wave velocity would seem to be consistent with the physical changes made to the medium. The cementation is bringing the particulate medium closer to a continuous medium and the wave velocity is increasing accordingly.

The change in the pulse length, when compared to uncemented particles, needs to be explored further. Long chain experiments with strain gages will be conducted to determine the entire effect.

The effect of contact angle, while not complete, would seem to indicate that the angle affects the velocity, the pulse length, and the load attenuation. One possible

explanation for the changes to the velocity and attenuation is that the pulse undergoes more scattering and dispersion upon encountering particle boundaries.

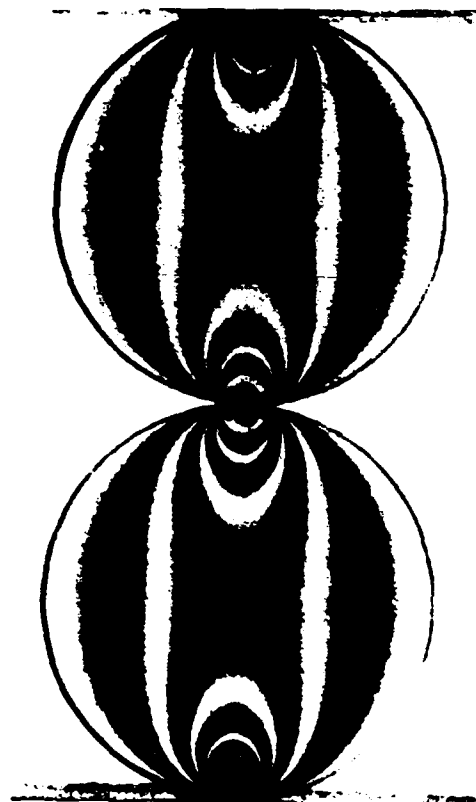


Figure 4.1. Typical isochromatic fringes for two cemented Homalite-100 disks under diametral compression.

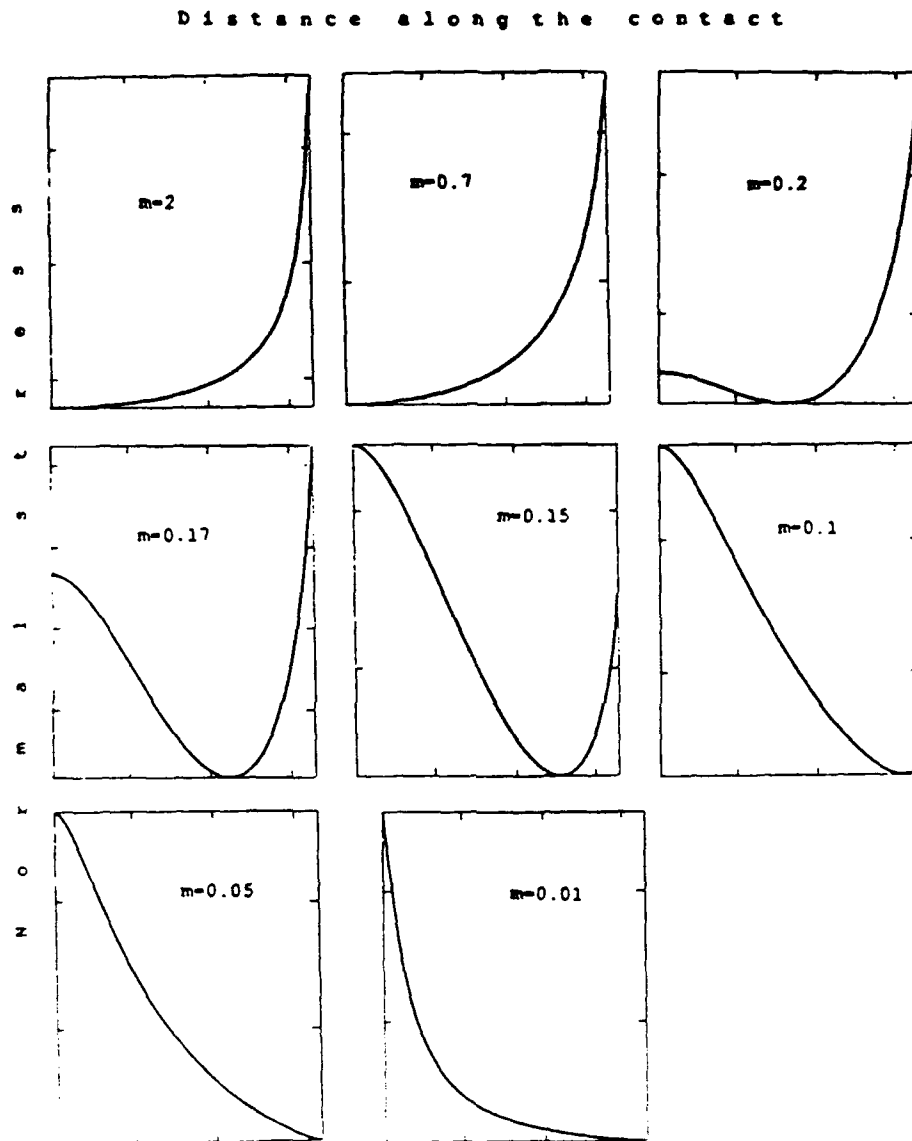


Figure 4.2. Plots of normal stress along the cement region as a function of the ratio of cement stiffness to particle stiffness. (from Dvorkin, 1991)

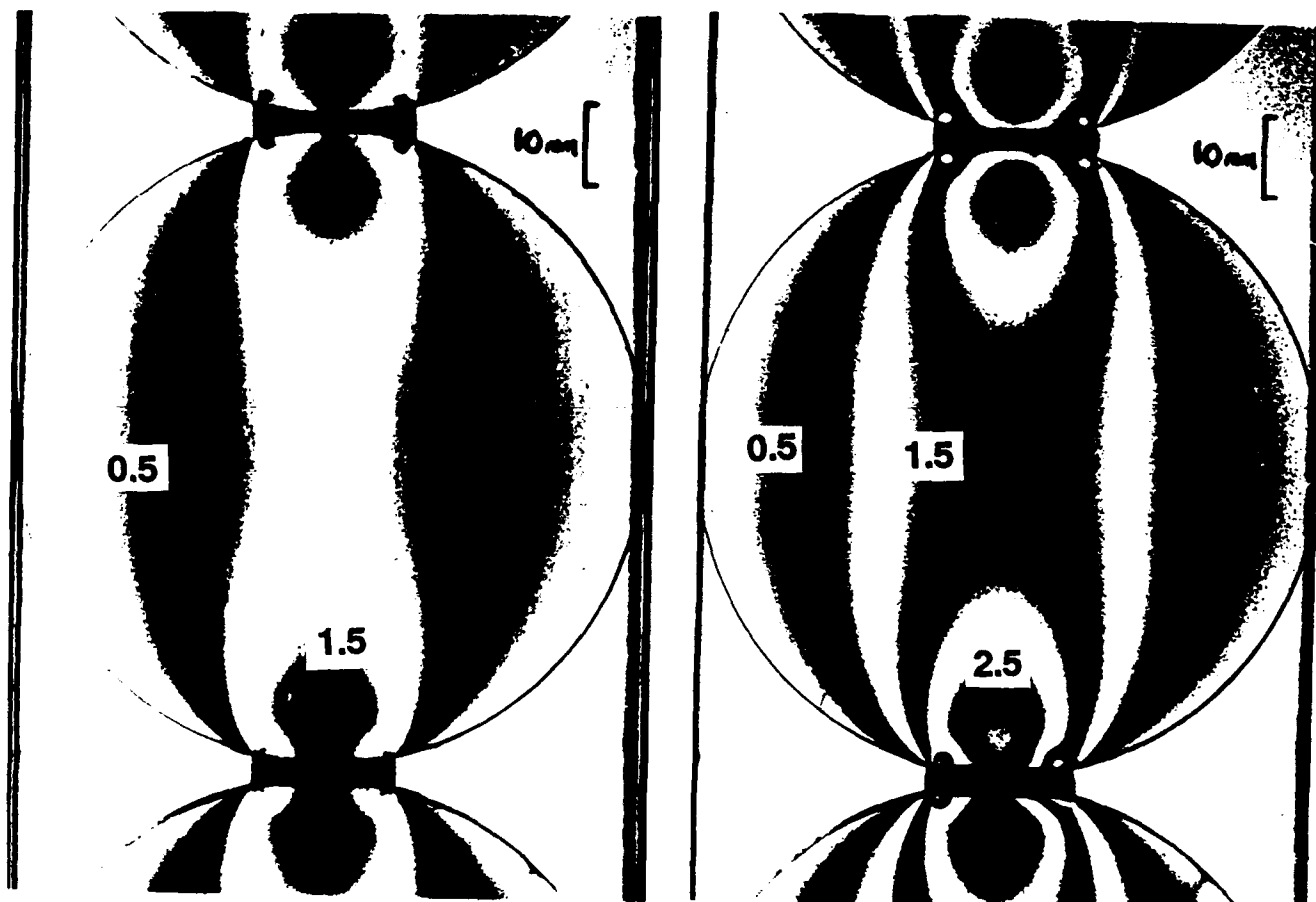


Figure 4.3. Typical isochromatic fringes for a PSM-1 disk under diametral compression with 'soft' cementation.

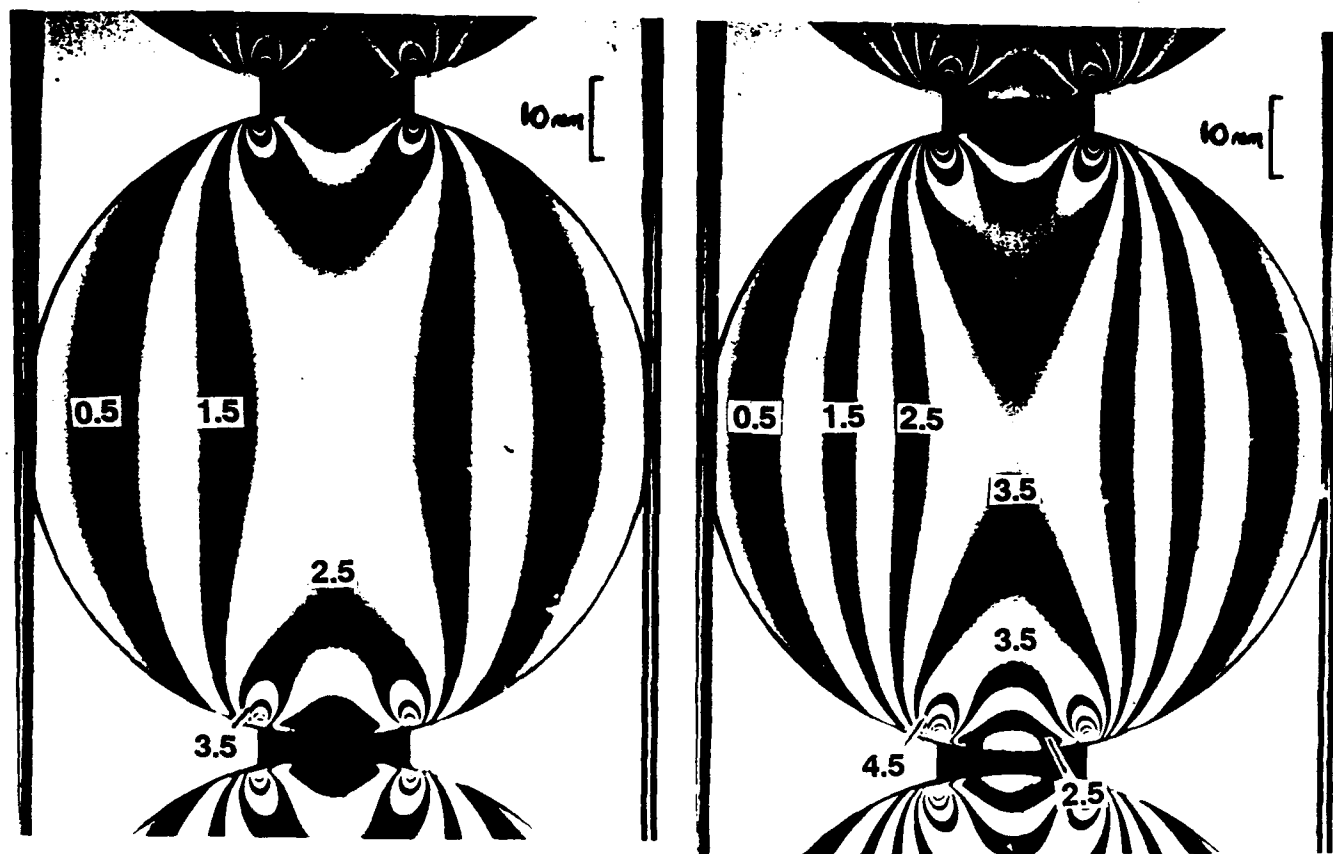


Figure 4.4. Typical isochromatic fringes for a PSM-1 disk under diametral compression with 'stiff' cementation.

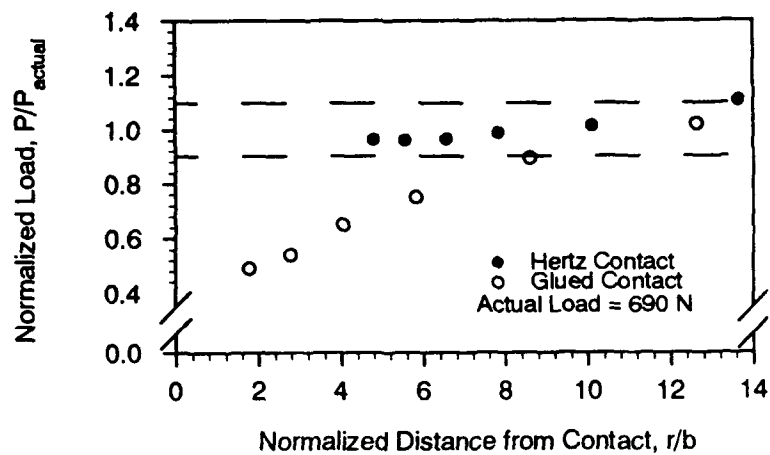
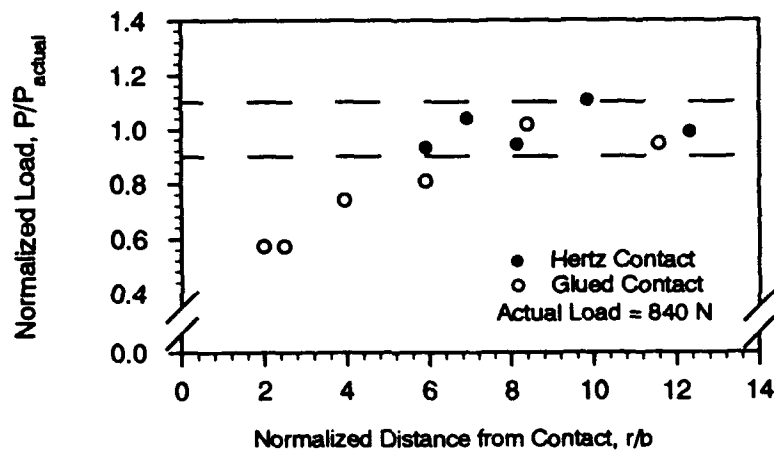
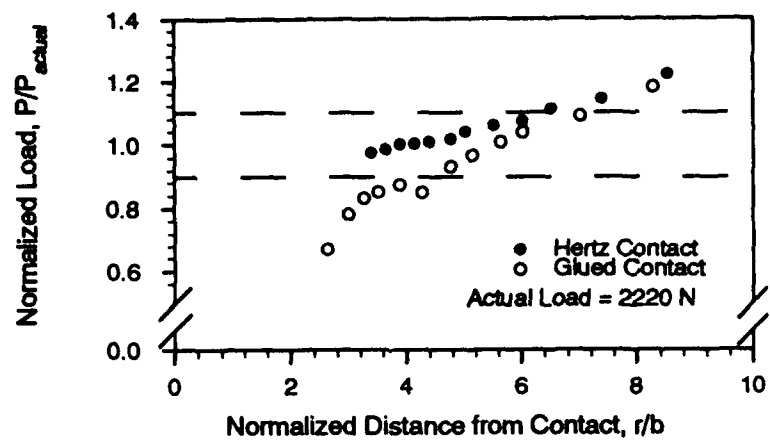


Figure 4.5. Plots of normalized load vs. normalized distance from the contact for static experiments.

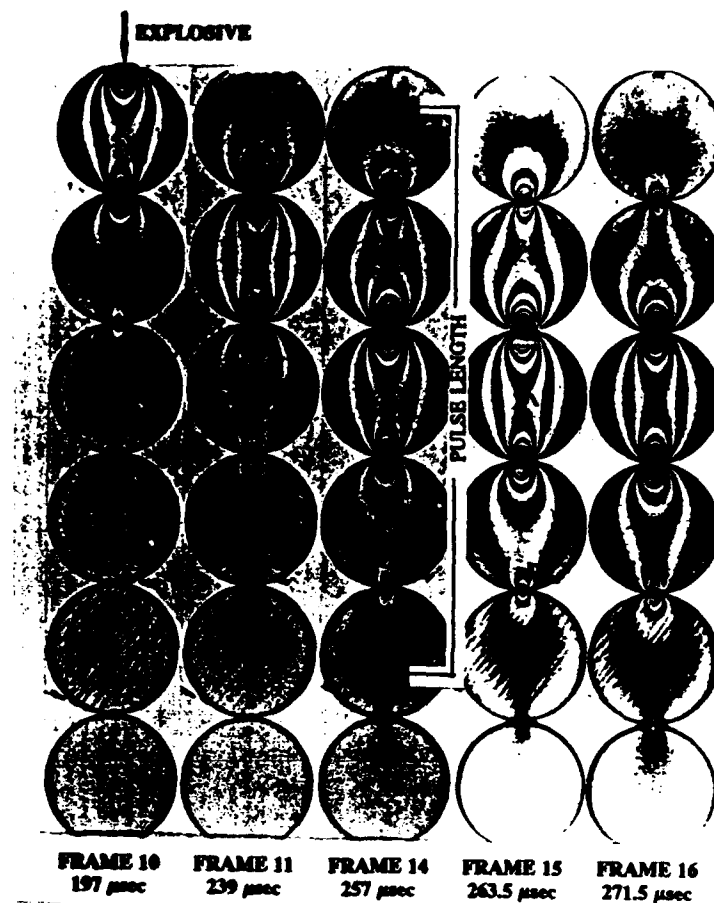


Figure 4.6. Typical isochromatic fringes obtained from a single, verticle chain of cemented particles.

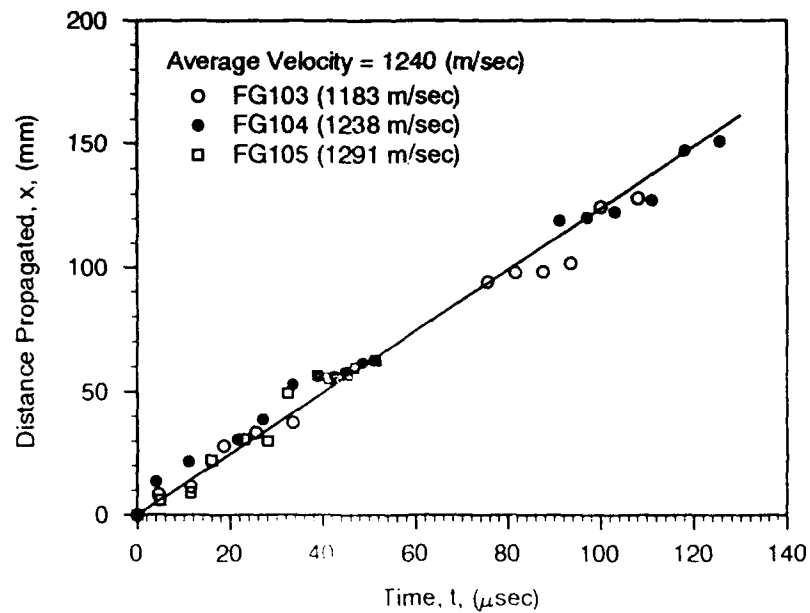


Figure 4.7. Distance vs. time plot for determination of group wave velocity.

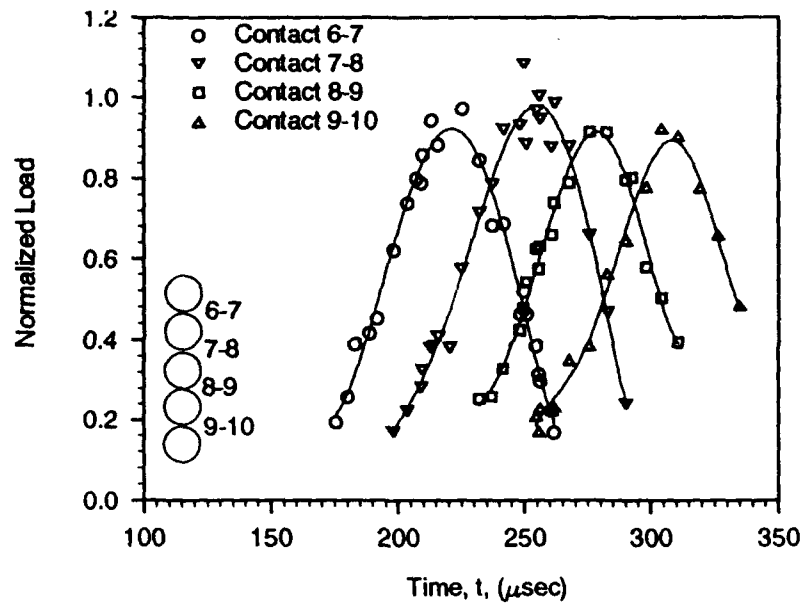


Figure 4.8. Plot of normalized contact load vs. time for the single, verticle chain of particles.

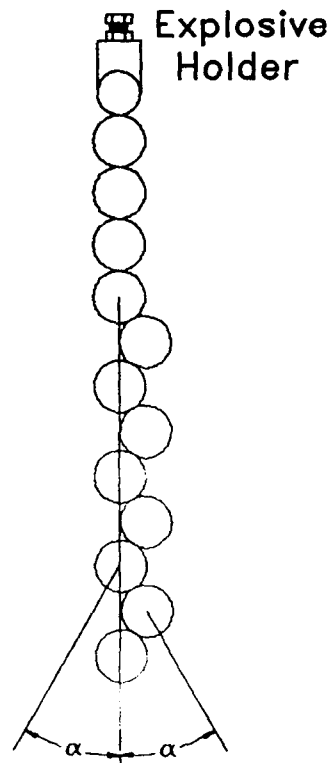


Figure 4.9. Schematic of the disk chain used for the cemented, angled contact experiments.

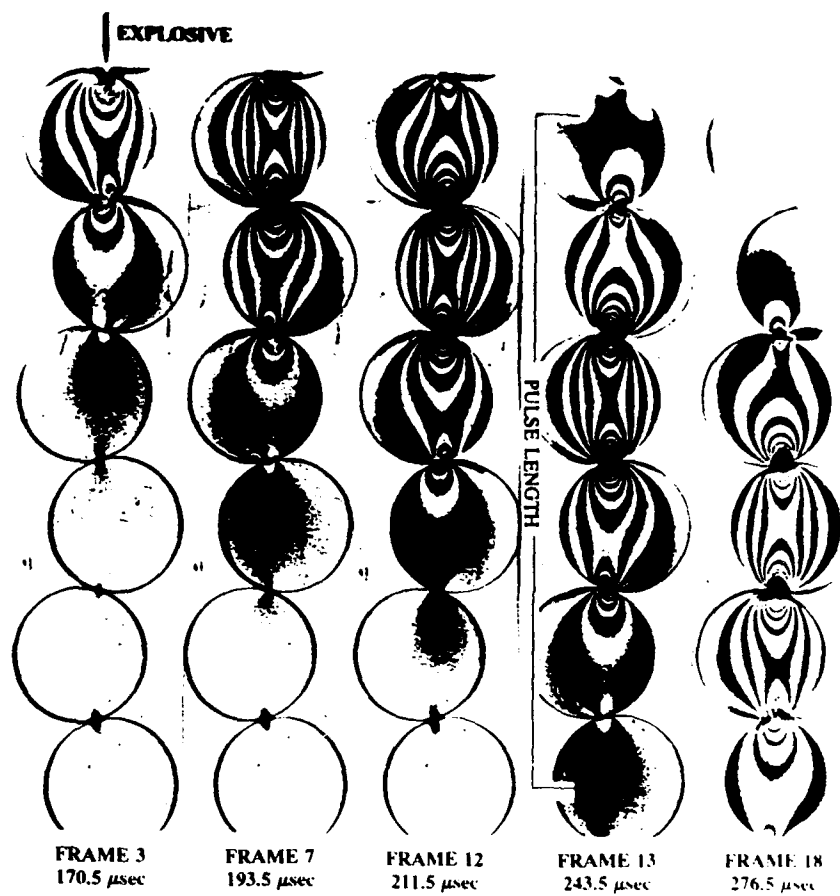


Figure 4.10. Typical isochromatic fringes obtained from a single, 15° angle chain of particles.

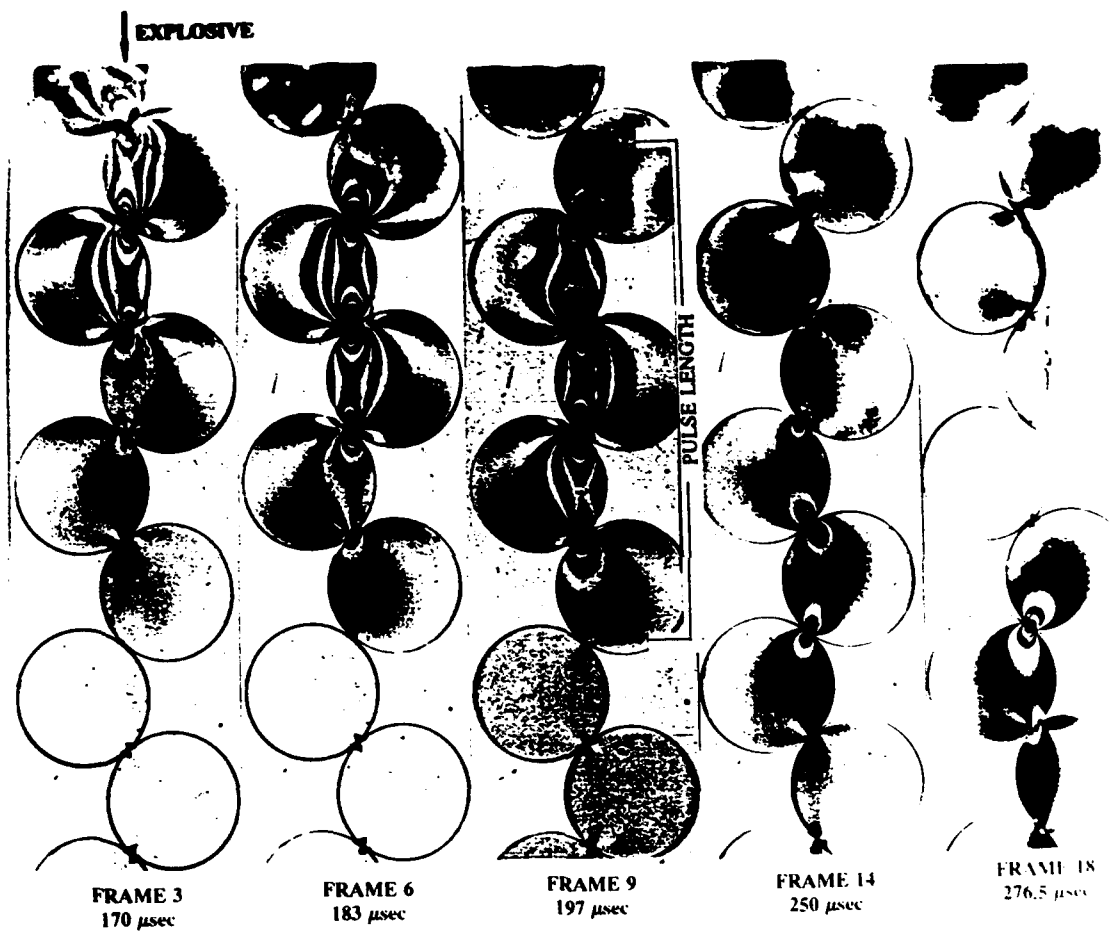


Figure 4.11. Typical isochromatic fringes obtained from a single, 40° angle chain of particles.

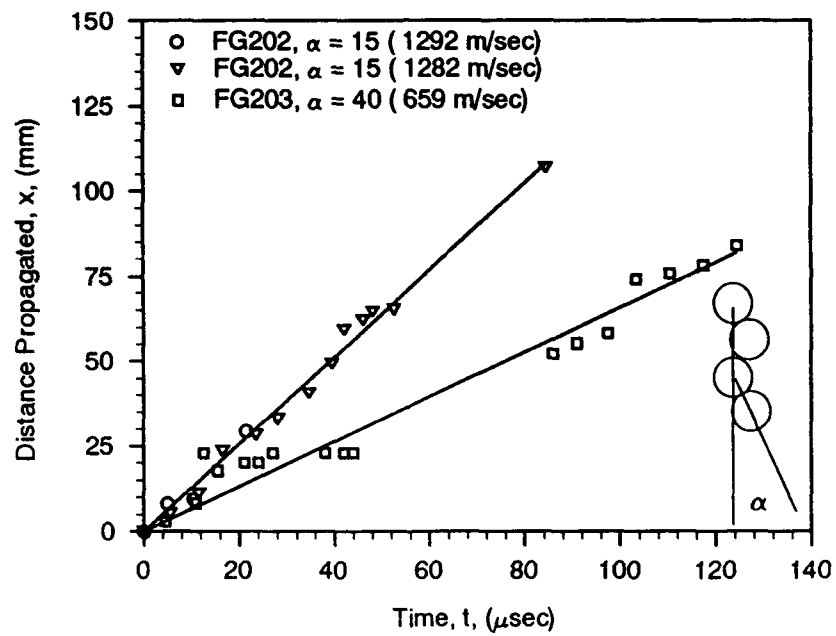


Figure 4.12. Distance vs. time plot for determination of group wave velocity for the angled particles.

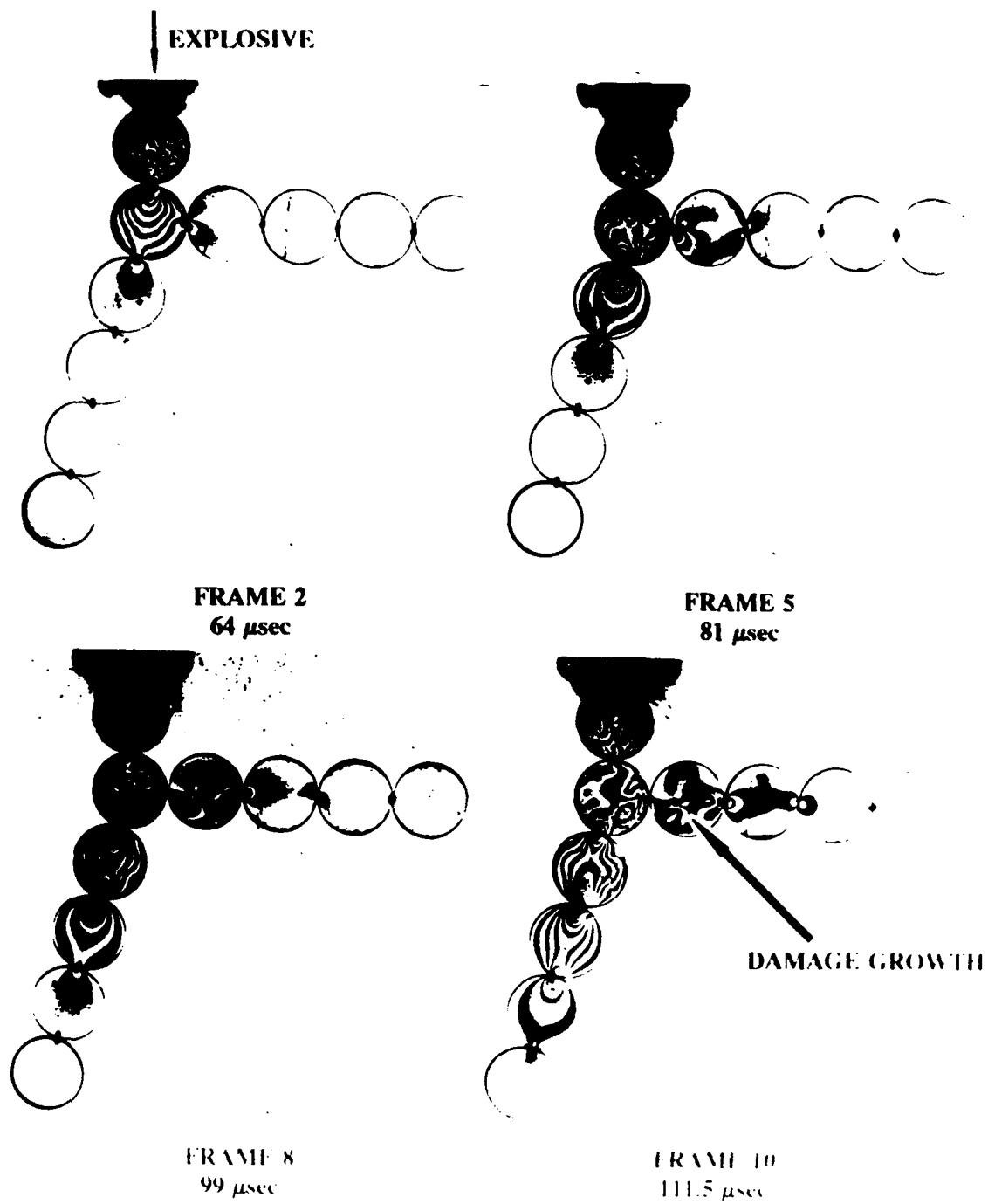


Figure 4.13. Typical isochromatic fringes obtained for two cemented disk chains showing energy transfer into the 90° disk chain.

CHAPTER 5

HYBRID THEORETICAL/EXPERIMENTAL DETERMINATION OF CONTACT LOADINGS BETWEEN CEMENTED DISK PARTICLES

5.1 Introduction

The determination of the correct contact law is a key problem in understanding the dynamic response and wave propagational behaviors of granular materials. In this regard, our previous research (Shukla, et.al. 1985, 1987, 1988) using dynamic photoelasticity has been very useful to determine the transient contact stress field inside model disk particles, and has provided fundamental information to help develop appropriate interparticle contact laws that have been used in computational models (Sadd, et.al. 1993). To date our studies have focused on particulate systems with dry and uncemented contacts. Interest has now developed into the dynamic behavior of cemented particulate materials, and the purpose of this chapter is to outline our initial research in establishing a hybrid experimental/theoretical scheme to determine the dynamic load transfer through such cemented systems.

Our photoelastic observations indicate that the local contact stress distributions between cemented disk particles are different from that of Hertzian contacts. This fact follows from photoelastic experiments, where it is found that the distribution of local fringe patterns of cemented and dry disks are different. Qualitatively, for high modulus cements, the maximum order fringe grows from the two ends of the contacting surface, while soft cements produce an evolving maximum order fringe interiorly located near the center of the contacting surface, see Figs, 5.1(a) and (b). For the dry case with no cementation (presumed to be Hertzian contact), the maximum order fringe grows from the center of the contacting surface

as shown in Fig. 5.1(c). Thus the local stress distributions close to the contact surface are clearly different between these cases. For Hertzian contact, an elliptical contact stress distribution is assumed, and the evaluation of the stress field within the cemented disks can be obtained from classical elasticity theory, (e.g. Timoshenko, and Goodier, 1970). Results of such a calculation (see Fig. 5.2) indicate that the predicted maximum shear stresses using Hertz theory are much higher than the photoelastic data for the case of disks cemented by a stiff material (super glue). As shown in the figure, the difference reaches 50% at the maximum shear stress point for the contact loading of 312lb.(1389N).

Dvorkin *et al.* (1991) proposed an analytical model to predict the influence of the cementation on the interparticle load transfer between . Using elasticity theory along with particular assumptions of the displacement distribution in the cement layer, an integral equation for the stress distribution on the contacting surface was determined. This solution was not in the explicit form and required considerable numerical calculations to determine the resultant forces between the cemented disks. Dvorkin *et al.* determined the stress distributions on the contacting surface for a special case in which the two cemented disks touch only at the center point of the contact line. These results show that the contact stress distribution profile changed significantly when the cement material modulus varied from soft to hard. When the cement layer is softer than the disk material, the maximum stress in the contact distribution lies in the center of the contact zone. On the other hand, if the cement material has a higher modulus than the disk particle, the maximum stress occurs at the edges of the contact area. Unfortunately, this scheme would not be very useful to be used with photoelastic data to develop a hybrid method to process dynamic fringe data to calculate interparticle load transfer.

In an effort to develop such a hybrid scheme, and guided by Dvorkin's results, various trial normal stress distributions on the contacting surface have been used to

calculate the maximum shearing stresses within contacting disks. The assumed contact loading distributions included convex parabolic, elliptical, uniform and concave parabolic profiles. Comparing the results of these trial contact loadings with photoelastic experimental data, it was found that the concave parabolic profile produced an acceptable comparison with the particular data set, see Fig. 5.2. This contact stress distribution was then used to compute the interior stress field within the disk, and this information was used to generate contour plots of the maximum shear stress (identical to photoelastic fringe patterns) as shown in Fig. 5.3. It can be seen that the numerical results closely match the experimental fringe patterns shown in Fig. 5.2(b). These preliminary trial results indicate that particular contact stress distributions on the cemented contacting surface could be used to determine the correct stress field within the disk particle. Thus an inverse problem solution strategy could be established whereby the resultant force between pairs of cemented disks could be determined from photoelastic experimental data. The present study uses such an approach to calculate the contact force between two cemented circular disks using a polynomial family of stress distributions on the contacting surface. The advantage of this method is computational efficiency and the fact that characteristics of the cementation need not be known. The information needed are the positions and the fringe orders of the photoelastic fringes within a contacting disk particle, the material and geometrical properties of the disk, and the cemented contact width. Several examples are given to verify the accuracy of this hybrid theoretical/experimental approach.

5.2 Basic Theory and Methodology

5.2.1 Classic Theory

From classical elasticity theory (Timoshenko and Goodier, 1970), the stress field for the plane problem of a circular disk loaded with a pair of equal and opposite forces as shown in Fig. 5.4, is given by

$$\begin{aligned}
\sigma_x &= -\frac{2P}{\pi} \left\{ \frac{\sin^2 \theta_1 \cos \theta_1}{r_1} + \frac{\sin^2 \theta_2 \cos \theta_2}{r_2} \right\} + \frac{P}{\pi R} \cos \varphi \\
\sigma_y &= -\frac{2P}{\pi} \left\{ \frac{\cos^3 \theta_1}{r_1} + \frac{\cos^3 \theta_2}{r_2} \right\} + \frac{P}{\pi R} \cos \varphi \\
\tau_{xy} &= \frac{2P}{\pi} \left\{ \frac{\sin \theta_1 \cos^2 \theta_1}{r_1} - \frac{\sin \theta_2 \cos^2 \theta_2}{r_2} \right\}
\end{aligned} \tag{5.1}$$

where the coordinates are indicated in Fig. 5.4.

The solution for a distributed boundary loading $f(\varphi)$, as shown in figure 5.5, can be obtained by integrating the fields specified by equations (5.1) to get

$$\begin{aligned}
\sigma_x &= \int_{-\alpha}^{\alpha} \left\{ -\frac{2f(\varphi)}{\pi} \left\{ \frac{\sin^2 \theta_1 \cos \theta_1}{r_1} + \frac{\sin^2 \theta_2 \cos \theta_2}{r_2} \right\} + \frac{f(\varphi)}{\pi R} \cos \varphi \right\} R d\varphi \\
\sigma_y &= \int_{-\alpha}^{\alpha} \left\{ -\frac{2f(\varphi)}{\pi} \left\{ \frac{\cos^3 \theta_1}{r_1} + \frac{\cos^3 \theta_2}{r_2} \right\} + \frac{f(\varphi)}{\pi R} \cos \varphi \right\} R d\varphi \\
\tau_{xy} &= \int_{-\alpha}^{\alpha} \frac{2f(\varphi)}{\pi} \left\{ \frac{\sin \theta_1 \cos^2 \theta_1}{r_1} - \frac{\sin \theta_2 \cos^2 \theta_2}{r_2} \right\} R d\varphi
\end{aligned} \tag{5.2}$$

The maximum shear stress is given by the well-known result

$$\tau_m = \sqrt{\left(\frac{\sigma_x - \sigma_y}{2} \right)^2 + \tau_{xy}^2} \tag{5.3}$$

Equations (5.2) and (5.3) indicate that τ_m can be calculated if the boundary loading distribution function $f(\varphi)$ and angle α are known. These parameters are directly related to the stresses transmitted to the disk particle from the cement layer.

5.2.2 Contact Stress Distribution

Dvorkin *et al.* (1991) studied the stress distributions at the surface of two cemented circular grains for the case with different ratios of cement to grain moduli. When the cement is soft relative to the particle, the maximum shear stress takes place in the center of the contacting surface, but when the cement is stiff the maximum shear stresses occur at the ends of the contact surface. Based on these results, it is assumed that all contact stress distributions could be represented by a family of

polynomials containing several parameters to provide the appropriate shape for the cement/particle moduli under study. Such a stress distribution polynomial can be written in the following form

$$f(\varphi) = P \left[1 + (m-1) \left(\frac{|\varphi|}{\alpha} \right)^n \right] \quad (5.4)$$

where P is the stress at the center of the contacting surface, m is the ratio of the center to the edge stresses, and n is the power of the polynomials.

If the parameters n and α are fixed, and the resultant force between the disks is held constant, the parameter m will dominate the appropriate shape of the curve (see Fig. 5.6). If $m = 1$, the distribution is uniform; for $m > 1$, the curve is concave; and $m < 1$, the curve is convex. Therefore, the loading shapes available with this $f(\varphi)$ -family approximately coincide with the results obtained by Dvorkin for various cement/particle moduli. The stresses within the disk particle that are determined by using the above contact stress distributions are very close to the experimental data. If all the parameters in the polynomial are given, the resultant force on the surface is determined by integrating the polynomial over the surface, i.e.

$$F_r = 2 \int_0^\alpha f(\varphi) R d\varphi = 2P\alpha R \frac{m+n}{n+1} \quad (5.5)$$

5.2.3 Numerical Scheme

Substituting the equation (5.4) into (5.2) and (5.3), produces the general form

$$\tau_m = \Re(P, m, n) \quad (5.6)$$

which is an implicit expression in terms of p , m and n .

According to photoelasticity theory, an isochromatic fringe pattern corresponds to a line of constant maximum shear stress which is specified by

$$\tau_{m_2} = \frac{f_\sigma \cdot N}{2h} \quad (5.7)$$

where f_o is the material fringe value, N is the fringe order number, and h is the thickness of the disk particle.

Using these results, an error function g can be defined as

$$g_k = \tau_{m_1} - \tau_{m_2} = \tau_{m_1} - \frac{f_o \cdot N}{2h} \quad (5.8)$$

where the subscript k refers to k -th data point. It is desired for this error function to be reduced to zero; however, applying this equation to actual data and using approximate analytical models for the calculated stress distributions will yield non-zero values for g_k . In order to reduce this error function to acceptable levels, numerical schemes have been developed. It has been established (Shukla and Nigam, 1985; McCalla, 1967; Singer, 1964) that by using Gauss-Legendre quadrature, along with a Newton-Raphson iteration method, a numerical procedure can be constructed to reduce g_k .

Applying these techniques to the current problem involving equations (5.6) - (5.8), it is first noted that initial estimates of the parameters P , m and n usually will not make $g_k=0$, and an iterative scheme is required. Equation (5.8) can be written in the form of a first order Taylor series expansion of g_k , i.e.

$$\left(\frac{\partial g_k}{\partial P} \right)_i \cdot \Delta P + \left(\frac{\partial g_k}{\partial m} \right)_i \cdot \Delta m + \left(\frac{\partial g_k}{\partial n} \right)_i \cdot \Delta n = -(g_k)_i \quad (5.9)$$

where the subscript i refers to an i -th iteration.

Applying this result to numerous photoelastic data points produces an over-determined system of equations. Solving this over-determined set produces corrections ΔP_i , Δm_i and Δn_i , which are used to improve the parameters through the relations

$$P_{i+1} = P_i + \Delta P_i, \quad m_{i+1} = m_i + \Delta m_i, \quad n_{i+1} = n_i + \Delta n_i \quad (5.10)$$

for the next iteration step. This procedure continues until the error difference between iterations is smaller than a specified controlling value.

5.3 Numerical Results

A computer code implementing the above procedures has been developed, and a preliminary numerical investigation has been conducted. Results from the code indicated that the determination of the resultant cementation forces was not very sensitive to the n parameter, and in fact values of n from 2 to 6 do not produce any significant changes in the results. Because of this fact, the n parameter was set at a constant value of 4, and only the parameter p and m were varied in the iterative scheme.

Data from several sets of photoelastic experiments were used to verify the hybrid approach previously described. The cement materials that were used in the experiments included urethane, super-glue, plexiglas and aluminum, which provided a variety of stiffnesses. All the model disks were made of polycarbonate. The data collection was completed by a digitizer that gives the position and fringe order of each photographic data point. The choice of the data points will affect the accuracy of the results. Generally one should take more data near the maximum shear stress points because the variation of these fringe positions with load is more sensitive than those of other fringes. For the urethane case (soft cement), the fringes were very thick, see Fig. 5.1(a), and it was difficult to determine the exact fringe orders. However, estimates were made of the approximate order number and the results proved to be satisfactory. The resultant forces between the disks were evaluated by the developed program, and these results are shown in the Table 5.1. Comparisons of the computed contact load transfer are made with the experimentally measured values, and the relative errors for all cases are less than 10%.

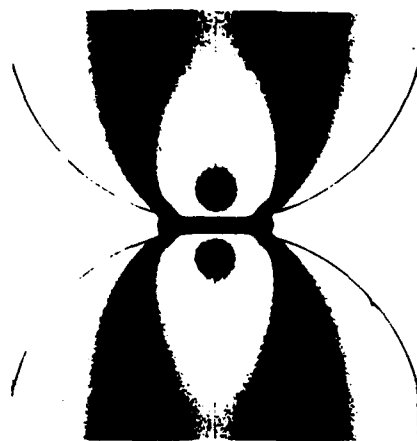
5.4 Summary

According to the theoretical results and experimental data, there are local differences between the contact stress fields of cemented disks and those under Hertzian dry-contact. In the neighborhood near the contacting surface, the Hertzian contact does not accurately predict the proper internal stress distribution. Because of *this a new hybrid scheme has been developed using non-Hertzian contact mechanics.* This technique uses a family of contact loading polynomials to approximate the actual load transfer between cemented particles. It has been demonstrated that these loading polynomials produce reasonably accurate stress fields which match with experimental photoelastic data, and can be incorporated into an inverse hybrid scheme whereby photoelastic fringe data can be used as input to a computer code in order to determine the interparticle load transfer. The polynomial family of contact stress distributions can cover a broad variety of cement types of various moduli ranging from soft to hard. The accuracy of the calculations appeared to be satisfactory as differences between numerical and experimental load transfers were all less than 10%. Further verification of this technique will be done on additional data.

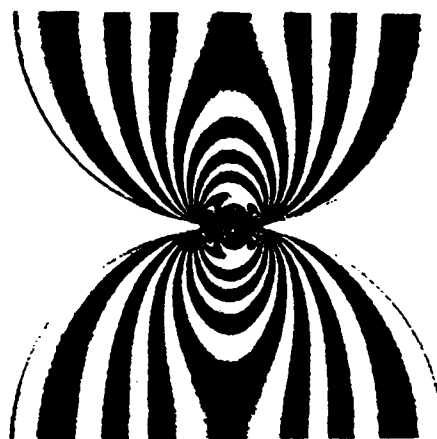
TABLE 5.1 Comparison of the Experimental and Numerical Results

Case 1 Urethane			Case 2 Super-Glue			Case 3 Plexiglas			Case 4 Aluminum		
Exp.*	Num*	Err.	Exp.*	Num*	Err.	Exp.*	Num*	Err.	Exp.*	Num*	Err.
200	192	4.0%	267	268	0.3%	95	100	4.3%	91	97	6.0%
222	217	2.4%	690	642	7.0%	191	204	6.5%	134	138	3.0%
			1291	1293	0.2%	270	293	8.5%	181	191	5.1%
			1389	1387	0.1%	357	380	6.6%	225	221	1.7%
			1772	1811	2.2%	447	481	7.5%	270	280	3.6%
			1905	1968	3.3%	537	573	6.6%	314	332	6.0%
			2226	2367	6.3%	629	646	2.8%	359	378	5.3%
						722	751	4.1%	407	422	3.8%
						812	855	5.4%	448	453	1.2%

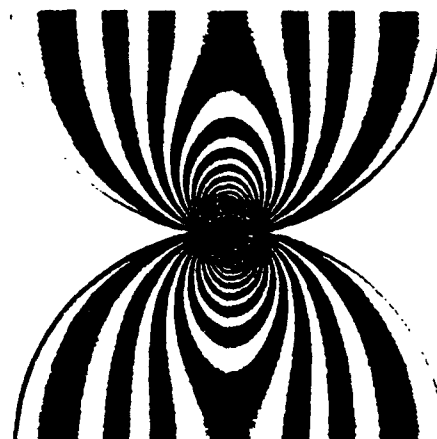
* All load units are in Newtons.



(a) Urethane Cement

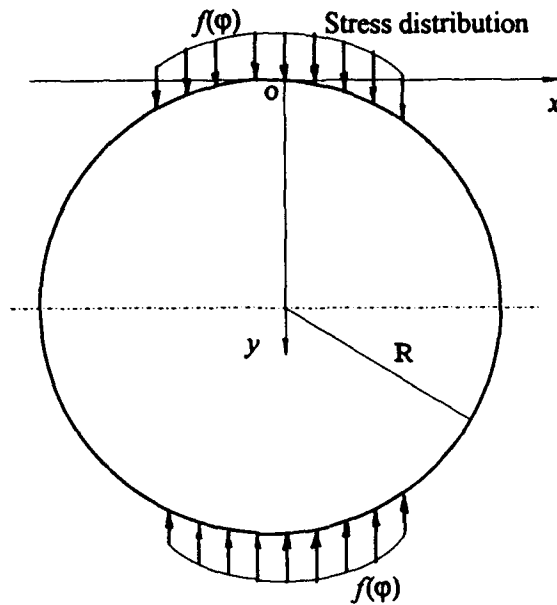


(b) Super-Glue Cement

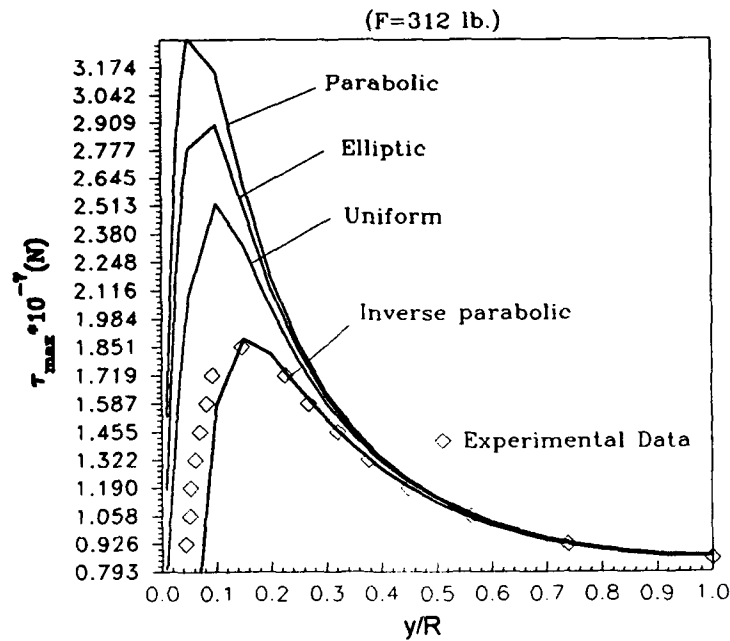


(c) No Cement (Hertzian Case)

Fig. 5.1 Photoelastic Fringe Patterns of Disks in Contact

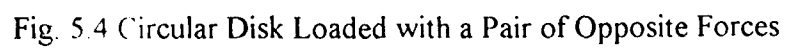


(a) Coordinate System and Loading Geometry



(b) Maximum Shear Stresses Along y -axis of the Disk Cemented by Super-Glue

Fig. 5.2 Comparison of the Maximum Shear Stresses



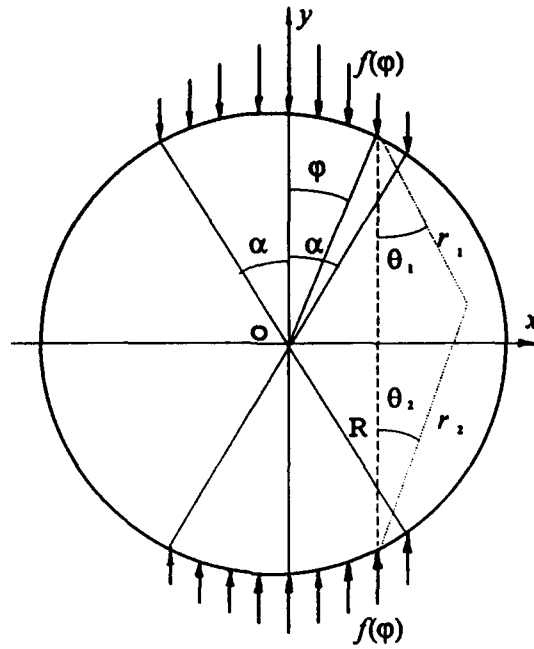


Fig. 5.5 Circular Disk Loaded with the Distributed Stresses

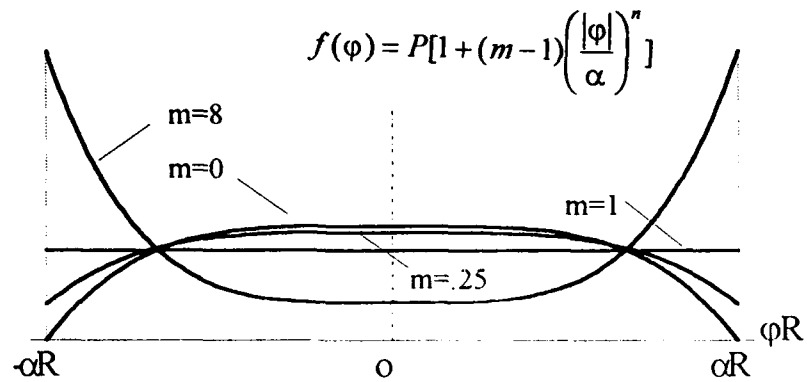


Fig. 5.6 Polynomial Family of the Stress Distributions
($n=4$ with a Common Resultant Force)

CHAPTER 6

PRELIMINARY STUDIES OF DYNAMIC LOAD TRANSFER THROUGH SATURATED GRANULAR MEDIA

6.1 Introduction

Preliminary microstructural modeling efforts have been conducted to investigate the effect of pore fluid in granular and particulate materials. The emphasis in this segment of our program is to establish reasonable models of the local microstructural interparticle contact effects associated with pore fluid, and to relate these effects to the wave propagational characteristics through model granular materials.

Our efforts in modeling the dynamic response of such fluid-saturated particulate materials have used the *discrete element method*. This computational method has shown to be very useful to model the response of discontinuous and particulate materials by studying the behavior of individual idealized particles in assembly systems. For applications to wave propagation, this scheme employs large assemblies of idealized particles to model the dynamic behavior of granular materials. Numerous studies by Sadd, et.al. (1989, 1991 and 1993) have shown that such modeling techniques can simulate granular materials and predict results which compare with experimental data. The numerical strategy uses Newtonian rigid-body dynamics to calculate the translational and rotational motion of each particle in these model assemblies. In this fashion, the dynamic/acoustic response of the model system may be determined, and parameters such as wave speed and amplitude attenuation can be calculated for specific model assemblies. Furthermore, these wave propagational characteristics can be related to the model material's *microstructure or fabric*.

Of fundamental importance for the proper application of this numerical scheme is the development of correct interparticle contact laws which predict the contact forces between adjacent particles in the assembly. These laws play a key role in determining the constitutive response at the micro-level. Much of our beginning work focussed on developing new contact models for particles interacting with each other through a fluid. The presence of pore fluid can have significant effects on the dynamic response of granular materials by adding viscous drag forces on particles and by changing the contact response between adjacent particles through *squeeze-film elastohydrodynamic action*.

6.2 The Discrete Element Method

As mentioned, the discrete or distinct element method is a modeling strategy which uses Newtonian rigid-body mechanics to model the translational and rotational motion of particles in model material assemblies (Figure 6.1). Contact laws between adjacent particles are constructed which serve to determine the contact force as a function of the relative displacement or relative velocity between the particles. Applying Newton's law to the i -th particle would yield

$$\sum_{j=1}^n F^{(ij)} + F^{(i)} = m_i \ddot{x}_i \quad (6.1)$$

where $F^{(ij)}$ are the j -contact forces on the i -th particle and $F^{(i)}$ represents any non-contacting forces (e.g. viscous drag). Equation (6.1) would then yield the particle acceleration with given contact and non-contact forces. The technique establishes a discretized time stepping numerical routine, in which granule velocities and positions are obtained from numerical integration of the computed accelerations. It is assumed that during each time step, disturbances cannot propagate from any particle further than its immediate neighbors. Under

these assumptions, the method becomes explicit, and therefore at any time increment the resultant forces on (and thus the accelerations of) any particle are determined solely by its immediate neighbor interactions. In wave propagation applications, the movements of the individual particles are a result of the propagation through the medium of disturbances originating at particular input loading points. Consequently, wave speed and amplitude attenuation (intergranular contact force) will be functions of the physical properties of the discrete medium, i.e. the microstructure. Figure 6.2 illustrates a typical flowchart of the discrete element method. In order to model particulate materials, the method is typically applied to granular systems containing large numbers of idealized particles (e.g. circular disks or spheres) in regular or random packing geometries. Such model materials can be computationally generated with varying degrees of microstructural fabric and pore fluid content.

6.3 Contact Laws for Particles in Saturated Media

Our modeling efforts began with the development of new contact laws governing particle interactions through a fluid. As mentioned, the presence of pore-fluid will create several new forces at the particulate level. For saturated conditions, capillary forces from the pore fluid would be negligible; whereas the phenomena of viscous drag and squeeze-film contact lubrication could produce sizeable particulate forces. Viscous drag effects would be predominant for large particle motions with significant inter-particle spacings where neighboring interaction forces are vanishingly small. On the other hand, squeeze-film contact forces would be the most significant for dense packings of particulate systems, and this case is the situation to be studied.

In order to model this squeeze-film effect, consider the case of two particles

(approximated as two circular disks) embedded in a viscous fluid, and approaching each other with a relative normal velocity $V(t)$, see Figure 6.3. The fluid film in the contact zone will be squeezed, and a sizeable pressure is thus built up in this contact region. The fluid pressure distribution in the gap will exert a loading on each particle surface, and this loading is sufficient in certain cases to produce significant particle deformation. In this fashion, the contact law governing particle interactions for saturated granular materials changes considerably from the contact mechanics for dry materials. The saturated case is more complicated since it involves a coupling of both fluid and solid behaviors.

The contact force for such a problem can be modeled using the theory of *elastohydrodynamics* e.g., Cameron (1967) and Gohar (1988). The schematic of the two-disk squeeze-film problem shown in Figure 6.3 describes the problem geometry. The distance between particle surfaces is denoted by $h(x,t)$, a function of coordinate x and time t , and $\delta(x,t)$ is the granule deformation. Under certain assumptions the fluid pressure $p(x,t)$ can be related to $h(x,t)$ by the *Reynolds equation of lubrication theory*

$$\frac{\partial}{\partial x} \left(h^3 \frac{\partial p}{\partial x} \right) = 12 \eta \frac{\partial h}{\partial t} \quad (6.2)$$

where η is the viscosity of the fluid.

Since $h(x,t)$ can include particle deformation $\delta(x,t)$ which is determined by elasticity theory, equation (6.2) is a *coupled relation*, and typically an iterative numerical method would be required to solve this equation for the pressure distribution $p(x,t)$. Incorporating such a numerical scheme into the discrete element method would result in a very computationally intensive procedure, and would therefore result in unreasonable amounts of CPU time to run the simulations. Therefore a simplified alternative procedure was developed in order to avoid

the numerical complexities. This simplified approach first assumes that the particle is rigid, and this allows a closed-form solution for $p(x,t)$ from equation (6.2). Once this pressure distribution is found, the particle deformation may be calculated from simple Hertz contact stress theory, and this new particle shape may be then used to calculate a new pressure distribution. Thus initially let $\delta(x,t) = 0$, and the undeformed particle surface can be approximated by the relation

$$h(x,t) \approx h(0,t) + \frac{x^2}{2R} \quad (6.3)$$

where R is the particle radius. The solution to the Reynolds equation (6.2) for this case is found to be

$$p(x,t) = -6R\eta \frac{V(t)}{h^2(x,t)} \quad (6.4)$$

With the pressure distribution known, the total contact load between the particles is given by integrating the pressure, i.e. $F = H \int p dx$, where H is the disk thickness. Carrying out the integration over the disk surface yields

$$F(t) = 3\sqrt{2}\pi\eta H \left(\frac{R}{h(0,t)} \right)^{3/2} V(t) \quad (6.5)$$

In order to include the effects of particle deformation, a combined model with two, series-connected stiffness (spring) elements may be used. One spring element represents the fluid stiffness while the other element includes the solid (particle) stiffness resulting from the elastic deformation within the particle. The pressure loading will produce deformations such that the distance between particle surfaces will change from h to $h(x,t) + \delta(x,t)$, where $\delta(x,t)$

is the contact deformation for the dry case. If the disk shape is assumed to be unchanged, then the new load $F(t)$ is still given by equation (6.5) using the modified value of $h(x,t)$, i.e.

$$F(t) = 3\sqrt{2}\pi\eta H \left(\frac{R}{h(0,t) + \delta} \right)^{3/2} V(t) \quad (6.6)$$

In dry granular materials, our previous research has indicated that the normal contact force F can be related to contact deformation by the relation $F = K\delta^{1.4}$, where K is a material constant. Obviously the forces in the fluid and solid springs should be equal, and this leads to the result

$$3\sqrt{2}\pi\eta H \left(\frac{R}{h(0,t) + \delta} \right)^{3/2} V(t) = K\delta^{1.5} \quad (6.7)$$

where on the right-hand side, the exponent on δ has been modified for convenience to the value of 1.5. Solving equation (6.7) for δ and substituting the result into equation (6.6) yields

$$F(t) = \frac{C_1 V(t)}{\left(0.5 \left(h(0,t) + \sqrt{h^2(0,t) + 4\left(\frac{C_1}{K}\right)^{2/3}} \right) \right)^{3/2}} \quad (6.8)$$

where $C_1 = 3\sqrt{2}\pi\eta R^{3/2}H$. Equation (6.8) then gives the normal contact force when two disks approach each other. For the case when the two particles move apart, contact law (6.8) is not suitable since a negative velocity V , may lead to a negative value within the square root. For this case the solid contact law will be used.

The above results address only the normal contact response between particles. For the tangential contact behavior, a simple modeling scheme based upon the simple shearing of

a Newtonian fluid is applied within the small interparticle gap as shown in Figure 6.4. If the gap is small then the fluid motion may be approximated by a linearly varying distribution (see Fig. 6.4a), and the resulting shear stress between the particles will then be given by

$$\tau = \eta \frac{\partial U}{\partial z} = \eta \frac{\Delta U}{\Delta z} = \eta \frac{V_1 - V_2}{h} \quad (6.9)$$

where U is the relative tangential velocity between particles. Thus the force between any two generic particles can be estimated by the product of this shear stress times an effective area within the gap zone. We are currently experimenting with various schemes to determine appropriate effective areas for the calculation of the tangential force.

Although this simple scheme provides reasonable estimates, it will break down if the interparticle gap becomes small. For this case, the spacing parameter h will be very small, and thus the velocity gradient and hence the predicted shear stress will become quite large. Therefore this model will predict unreasonably high values of the interparticle tangential load transfer. This situation has been studied previously by the lubrication community, and it has been found that for very small gap widths, the assumption of zero slip conditions is not satisfied. Previous studies have found that it is necessary to introduce a *slip velocity*, V_s , to account for the fact that fluid particles will not adhere to the solid particle surfaces. This situation is shown in Fig. 6.4b, and the effect of this slip velocity is to lessen the severe velocity gradient within the gap. This modeling approach will control the predicted tangential load transfer, and we intend to formulate this scheme into the wave propagation DEM code.

6.4 Results

In order to investigate the merit of the proposed modeling scheme, several one- and two-dimensional material models were created, and the discrete element computer code was

then applied to each of these models under specific dynamic loading conditions designed to simulate geoacoustic wave propagation.

6.4.1 One-Dimensional, Single Chain Simulations

The previously described contact law has now been incorporated in our basic discrete element computer code. Preliminary computer runs have been conducted in order to simulate the acoustic wave propagation in an one-dimensional granular material simulated by a single straight chain of circular disks as shown in Figure 6.5. Considering the modeling of a coarse sand, the circular particles had a diameter of 2mm, thickness of 1mm, and were assumed to be of quartz with a density of 2650 kg/m³. The simulations incorporated different gap openings (of the order of one micrometer) between each neighboring particles, and the model system was assumed to be completely saturated with water of viscosity of 0.0008 N-s/m². The input loading applied to one end of the particle chain was taken to be a triangular time dependent pulse of duration 2.5μs with a peak value of 4N to simulate a wave front acoustic pressure of 10⁶ N/m² (i.e. 10 bar).

Using these parameters, a computer simulation was run and the wave attenuation results are shown in Figure 6.6. It was found that the attenuation is quite large during the passage through the first several particles, but then the attenuation rate decreases with the propagational distance. These preliminary simulations indicated that the wave speed was approximately 840 m/s. The effects of the gap distance and viscosity on the wave speed was also investigated, and these results are shown in Figure 6.7. As expected, the wave speed decreases with the gap distance, and when the gap is small, these effects are rather pronounced. An increase of fluid viscosity also leads to a decrease of the wave speed, and again this variation was most severe for the case of small gap distances.

6.4.2 Two-Dimensional Simulations

In order to investigate the use of the model for a multi-dimensional simulation, a two-dimensional granular model assembly was generated. The assembly, shown in Figure 6.8 was created using one of our computational random media generators. These generating codes can create large random particulate assemblies with varying degrees of microstructural fabric such as porosity, coordination number, particle contact normal and branch vector distributions, void vectors, etc. Dynamic input for wave propagation was created through simultaneous loading of particles along left and bottom edges of the assembly as shown. Input loadings were applied with identical magnitude and time history as used in the one-dimensional simulations. The transmitted wave output (measured by the inter-particle contact forces) was collected among the particles along the right and top sides of the assembly, and thus this technique can provide comparisons of horizontal and vertical wave propagational behaviors.

In order to correlate material microstructure to the wave propagational behaviors, the *branch vector distribution* of the assembly in Fig. 6.8 was computed. The branch vector is a commonly used microstructural fabric measure that relates the relative positions between particles. It is defined as the vector drawn between adjacent particle mass centers, and Fig. 6.9 illustrates a polar rose diagram plot of this distribution for the assembly of Fig. 6.8. It can be observed from the distribution plot that this model material system shows preferred directions (anisotropy) with more branch vectors distributed in the horizontal direction than in the vertical. Thus we would expect more wave transmission for the horizontal loading case.

Discrete element simulation results of the wave propagation through this assembly are

shown in Figure 6.10. Normalized average wave transmission through the assembly for the horizontal and vertical loading cases are illustrated. The vertical scale represents the average of all interparticle load transfers at the output side of the assembly normalized with respect to the input. These results indicate that the wave transmission is clearly related to the anisotropic fabric of the model particulate material in that less wave attenuation occurs for the horizontal propagation case. Figures 6.11 and 6.12 show vertical and horizontal propagation results of the same model material for the case with different inter-particle gap spacing. It can be observed that with an increase of the gap spacing, attenuation will increase while propagational speed will decrease. These results are consistent with our one-dimensional simulations.

Future work with saturated systems will include improvements in the basic inter-particle modeling and we intend to conduct an extensive series of computer runs to establish more specific relationships with fabric and wave propagational behaviors.

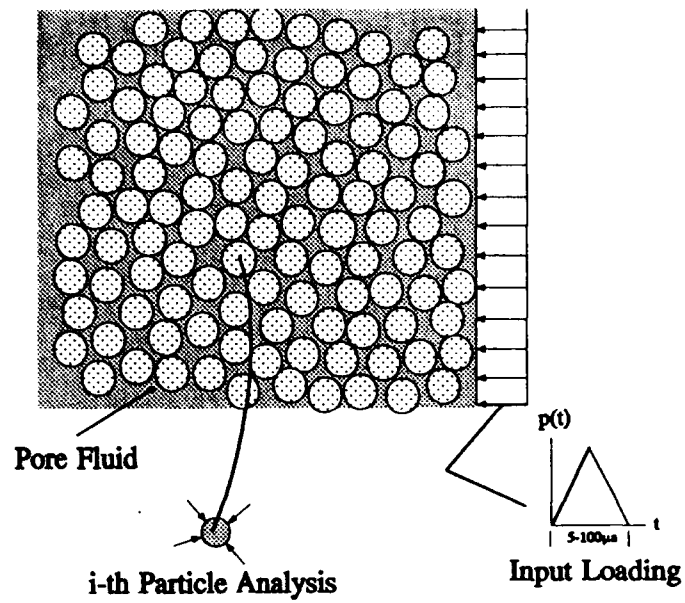


Fig. 6.1 Discrete Element Simulation

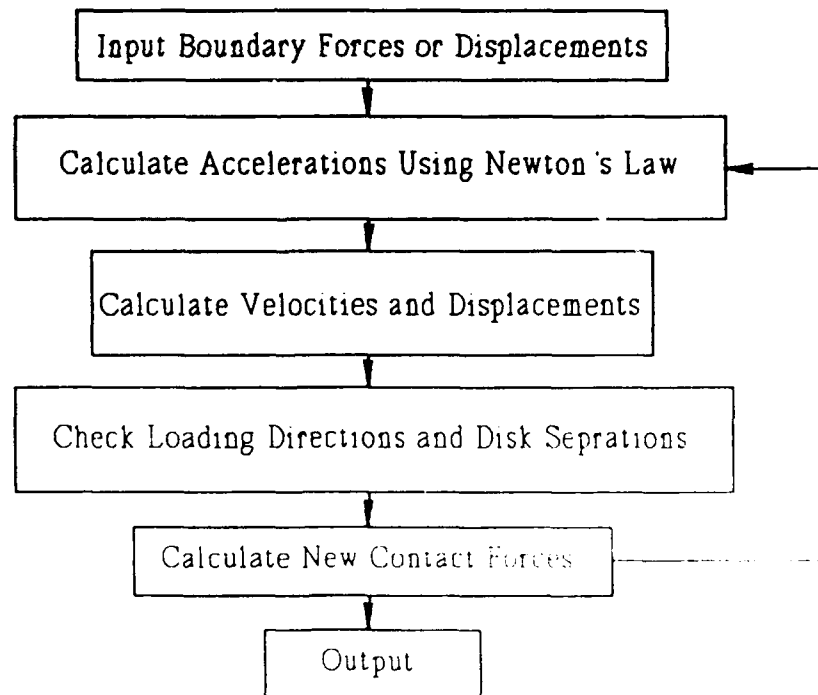


Fig. 6.2 Discrete Element Method Flow Chart

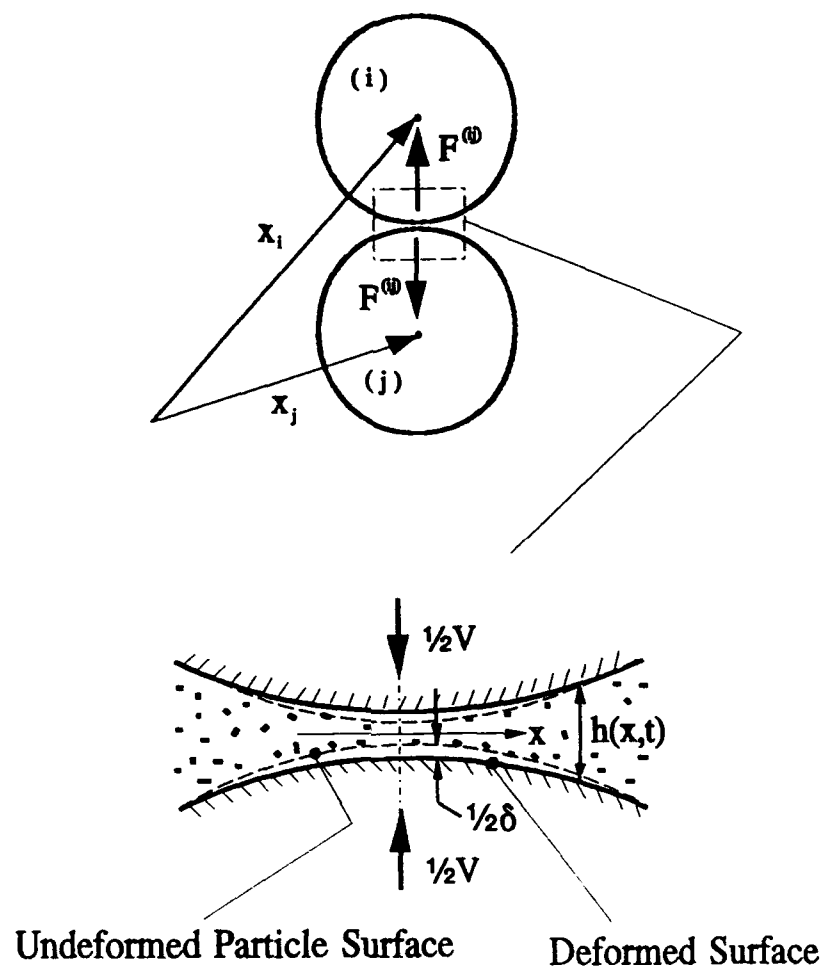
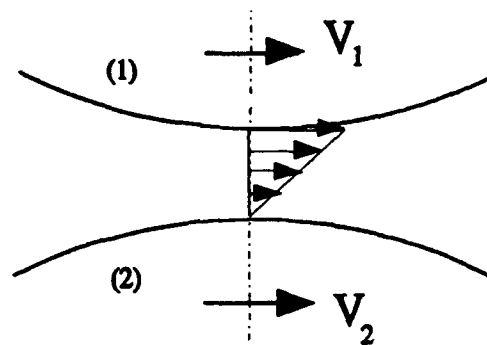
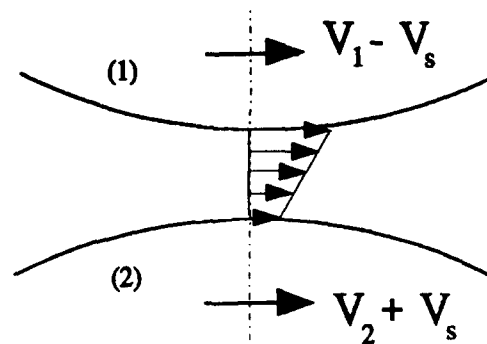


Fig. 6.3 Elastohydrodynamic Action Between Particles



(a) No Slip Conditions



(b) Slip Conditions (V_s = Slip Velocity)

Fig. 6.4 Tangential Pore Fluid Velocity Behavior



Fluid Gaps Between Each Particle

Fig. 6.5 One-Dimensional Single Chain Model

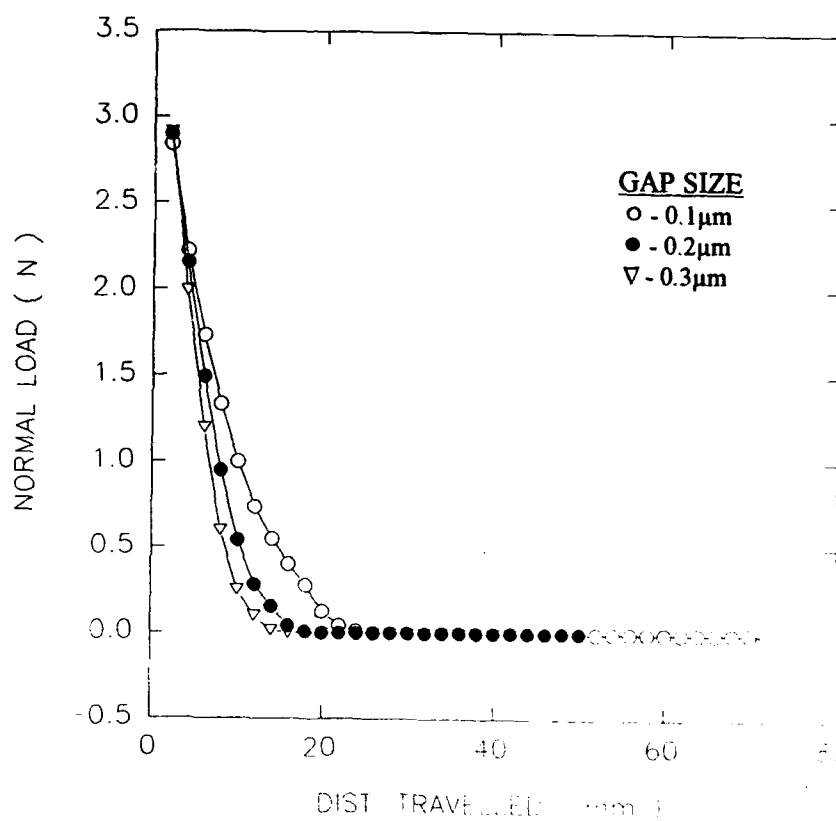


Fig. 6.6 Wave Attenuation Behavior for Single Chain Model

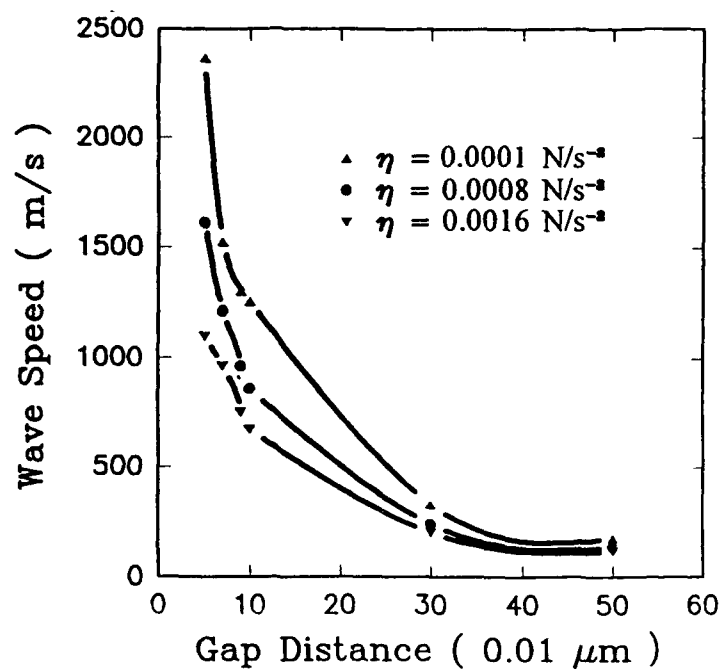


Fig. 6.7 Wave Speed as a Function of Gap Spacing
and Viscosity for Single Chain Model

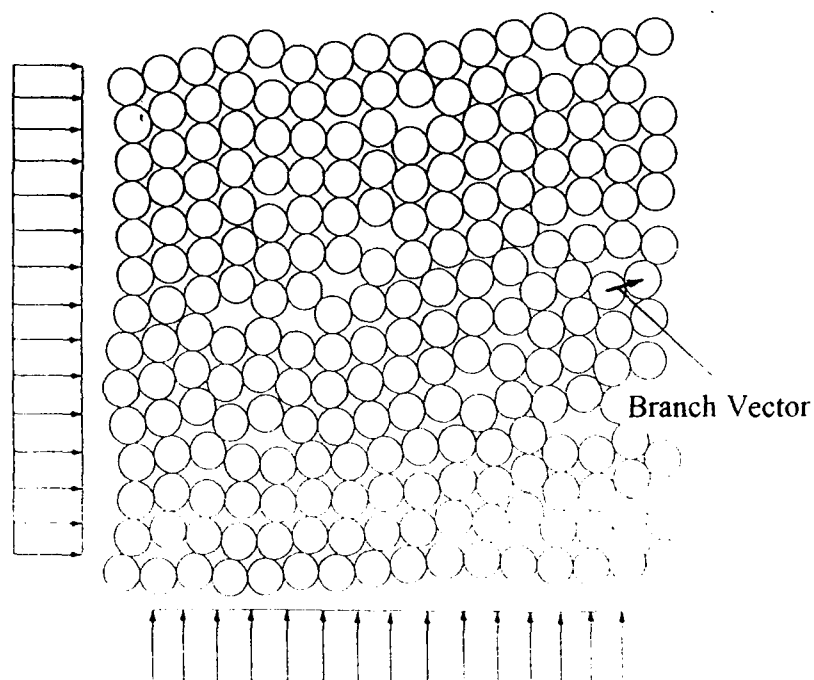


Fig. 6.8 Two-Dimensional Random Granular Model

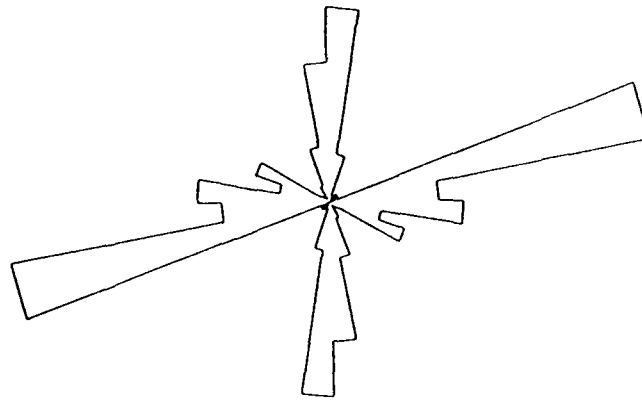


Fig. 6.9 Branch Vector Distribution Diagram of Random Model

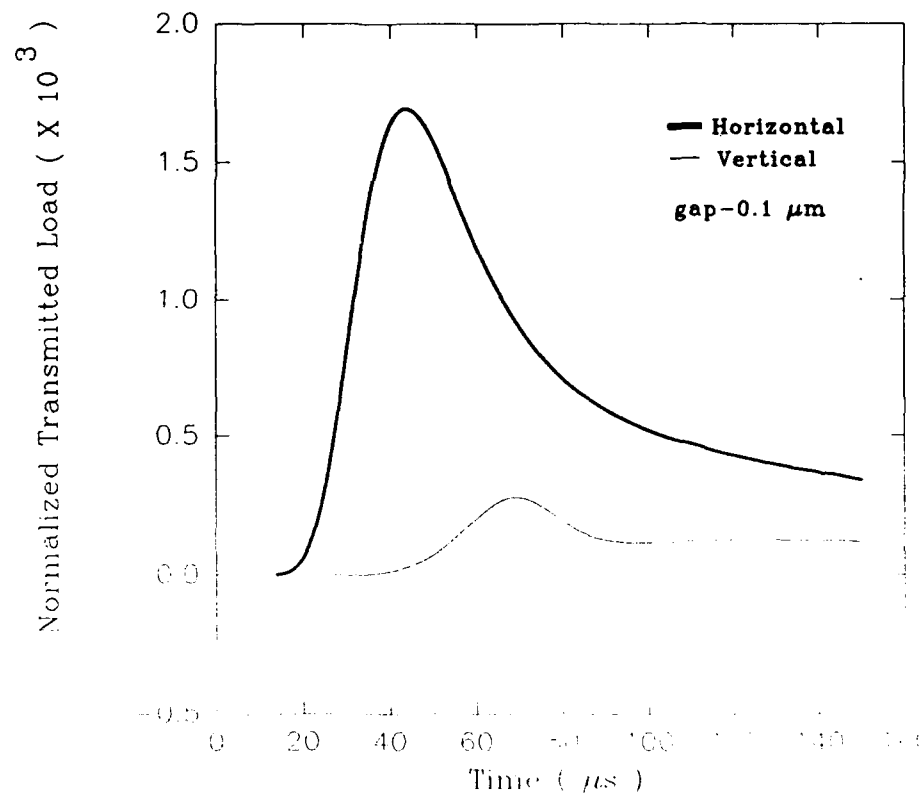


Fig. 6.10 Average Wave Amplitude Transmission Through the Random Model

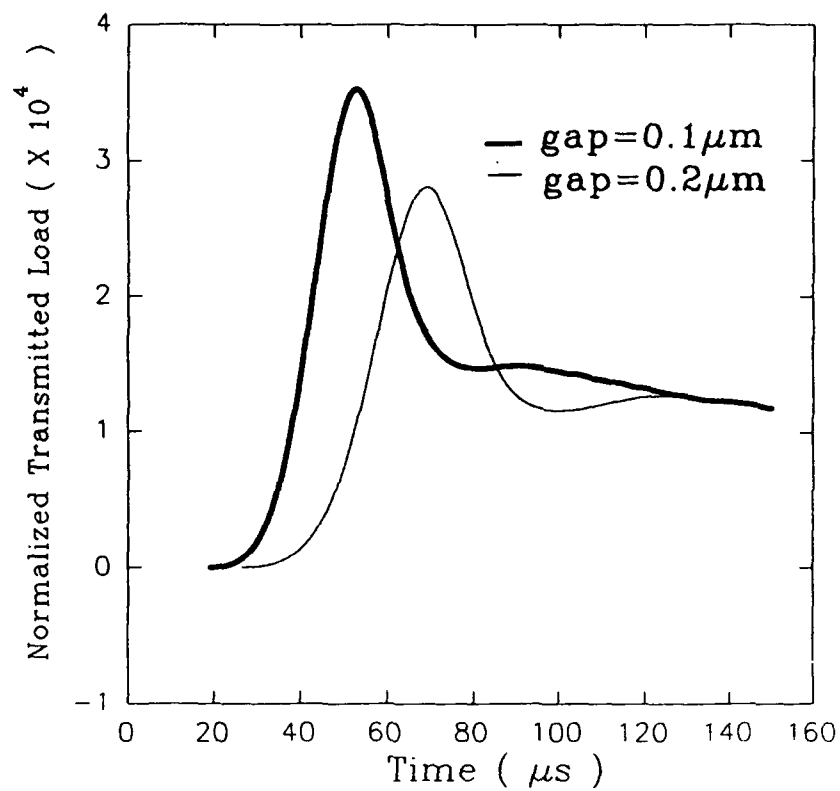


Fig. 6.11 Vertical Transmission Through the Random Model

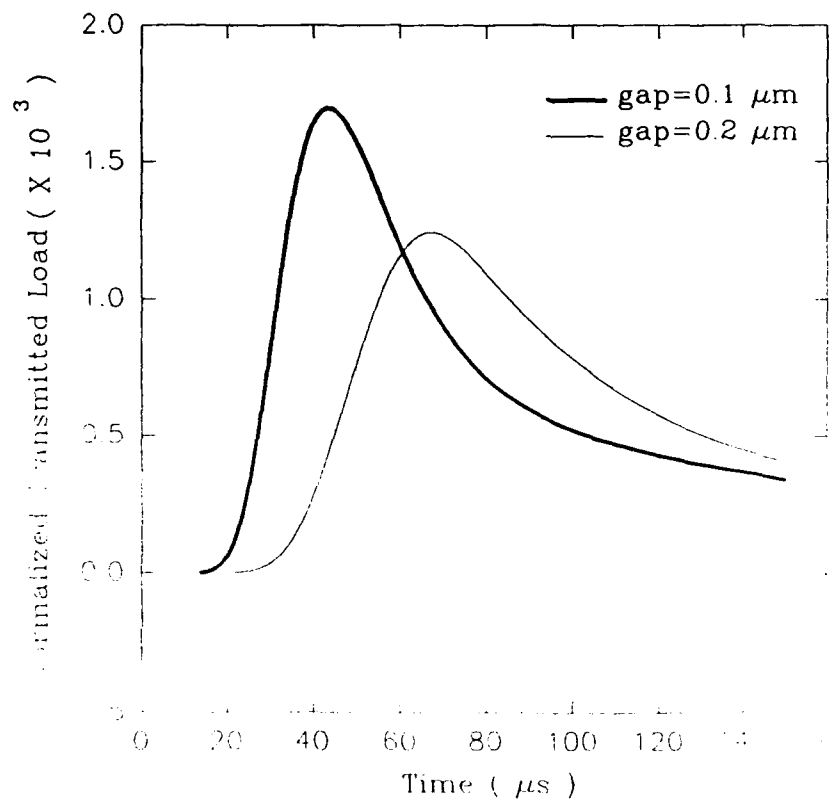


Fig. 6.12 Horizontal Transmission Through the Random Model

CHAPTER 7

INFLUENCE OF PARTICLE SHAPE ON THE DYNAMIC LOAD TRANSFER PROCESS

A preliminary investigation was conducted to study the effect of contact profile and granular media porosity on inter-granular load transfer, wave velocity, and wavelength of a stress wave propagating through the granular media subjected to explosive loading. Dynamic photoelasticity, the combination of high speed photography and photoelasticity, was used to study stress wave transmission through the granular media that were simulated by assemblies of circular or non-circular particles in contact. The photographs thus obtained were analyzed to determine contact load as a function of time, wave velocity, and wavelength. Specimens were made of Homalite-100, an optically birefringent material. Since some of the specimens were not circularly symmetric, experiments were conducted with the specimens oriented both with the major physical feature toward the incoming pulse and away from the incoming pulse. The results indicate that contact profile and media porosity have an effect on wave velocity and wavelength.

7.1 Introduction

Several investigations have previously been conducted by many researchers to study the dynamic behavior of granular media. The load transfer characteristics, wave velocity, and wave dispersion for various loading parameters and microstructure of granular media have been studied in detail. The effect of particle shape on wave propagation has been studied by Shukla et.al (1991) using elliptic particles. They showed

that the wave velocity was dependent on the particle shape. The wavelength of the stress wave pulse showed no change with the particle shape as long as the contact interval (the number of contact points per unit wavelength) is kept constant. The load transfer characteristics change with variations in particle shape. However, in most of the past work the granular media was simulated by assemblies of circular or elliptical discs. All contacts were therefore between two convex surfaces. In real life, some contacts are between concave and convex surface. The change of particle shape and thus of contact profile causes the contact stiffness to change. If the radius of curvature at the contact is increased, while keeping the contact interval constant, the contact stiffness will increase, and this would imply a higher wave velocity. This may also change the wave propagation characteristics.

In this work, four groups of disks were used to simulate the granular media. The interest lay in the investigation of the effect of a concave-convex contact and porosity of media on the load transfer characteristics, wave speed and wavelength. Specimen geometric parameters are shown in Table 7.1. The Groups 1 and 2, as shown in Fig. 7.1, were also used to study the effect of incident direction on wave propagation characteristics.

7.2 Experimental and analytical procedure

The method of dynamic photoelasticity was used as the experimental technique throughout this investigation. This method has been shown by many researchers to be very efficient in the study of dynamic wave characteristics in granular media (for example Shukla 1991). As stated earlier, Homalite-100 was chosen to make specimens. To

fabricate the various particles, one inch diameter circular disks were machined into the geometries shown in Table 7.1. A cooling system was used during machining of the specimens to avoid producing any heat related residual stresses in the specimens.

The granular media was simulated by single chain assemblies of similarly shaped particles in contact. One such setup is shown in Fig. 7.1 (a). The same shaped particles were also used in an alternative setup, as shown in Fig. 7.1 (b), to investigate the effect of incident direction of the wave pulse on the propagation characteristics. The six different single chain assemblies used in this study are shown in Fig.7.2.

The experimental models were placed in the optical bench of a high speed Cranz-Schardin type camera. The particles were loaded by exploding a small amount (10 mg) of Lead Azide in a specially designed charge holder. The camera was triggered at some prescribed delay time after *igniting the explosive* that was placed on top of the model (see Fig. 7.1). The high speed photography system operated as a series of high intensity, extremely short duration, pulses of light and provided twenty photoelastic images at discrete time during the dynamic event.

A typical sequence of six images for the single chain setup is shown in Fig. 7.7. These images of the propagation phenomenon were enlarged and digitized to facilitate analysis. The Hertz stress field equations along with the stress optic law (see Chapter 4) were used to calculate the contact load at a particular contact point and time by applying the multi-point, non-linear least square method suggested by Shukla and Nigam(1986). The wavelength of the stress wave pulse can be measured directly from the photographs of the wave propagation process (Fig. 7.7). The propagation distance is plotted as a function of time to obtain the wave velocity.

7.3 Results and discussion

To understand the effect of particle shape on wave velocity , wavelength and load transfer characteristics, a series of experiments were conducted with the experimental arrangement shown in Fig. 7.1.

Figs. 7.7 and 7.3 show typical isochromatic fringe patterns and average velocity of the stress pulse for chain 1 (see Fig. 7.2) respectively. Likewise, the fringe patterns and average velocity for chains 2, 3 and 4 are shown in Figs. 7.8, 7.9, 7.10, 7.4, 7.5, and 7.6.

The average velocities of stress pulse for chains 1 and 2 (contact between convex and flat surfaces) were determined to be approximately equal, 1010 m/s and 1020 m/s respectively (see Figs. 7.3 and 7.4). This shows that the incident direction of propagation has no effect on average pulse velocity for this particle shape. Figs. 7.5 and 7.6 show that the average velocities of stress pulse for chain 3 and 4 (contact between convex and concave surfaces) are 1140 m/s and 1100 m/s respectively. This indicates that the incident direction of propagation also has no effect on average pulse velocity for this particle shape. The stress pulse velocity in chain 3 and 4 is 10% higher than that in chain 1 and 2. This can be explained by the fact that the contact stiffness between convex and concave surfaces is higher than that between convex and flat surfaces.

Compared with the pulse velocity in one inch diameter circular disk chain, the wave velocity in chain 3 and 4 is slightly higher because of larger contact stiffness. However, the wave velocity in chain 1 and chain 2 is slightly lower than that in one inch diameter circular disk chain despite the larger contact stiffness. The reason for this is the increased number of contacts per unit length in chains 1 and 2 as compared with a one

inch diameter circular disk chain.

Typical isochromatic fringes obtained from various experiments involving single chain assemblies are shown in Figs. 7.7, 7.8, 7.9, and 7.10. The wavelengths for chains 1,2,3, and 4 were directly measured from these Figs. and are shown in Table 7.2. The pulse lengths for chains 1 and 2 were found to be equal. Chains 3 and 4 also produced equal pulse lengths. This would lead one to believe that the incident direction of propagation has no effect on the pulse length. It was also noticed that wavelengths of chains 1 and 2 were larger than those of chains 3 and 4. The pulse lengths of chains 3 and 4 were nearly four disk lengths. This difference in pulse lengths may be the effect of contact profile. Fig. 7.10 also shows that the fringe patterns tend to take the shape of the particle as the stress wave travels through it. This phenomenon also can be seen in *elliptical disk experiments.* (Shukla 1991)

Data collected from fringe patterns in Figs. 7.7, 7.8, 7.9, and 7.10. was used to calculate contact load. The contact load variations with respect to time, for different disk chains are shown in Figs. 7.11, 7.12, 7.13, and 7.14. The contact loads have been normalized with respect to the peak contact load between particles 5 and 6. This normalization allows for easy comparison between different experiments.

Normalized contact load plots provide information about load attenuation as the stress wave travels from contact to contact. They also provide information about the duration of contact. Figs. 7.11, 7.12 and Figs. 7.13, 7.14 show that load duration for flat particles was slightly longer than that for concave particles. The reason is that the concave particle chain has higher wave velocity and shorter wavelength than flat particle chain has.

Figs. 7.15 and 7.16 are the average velocity plots for chains 5 and 6. If we define the porosity, η , as in equation (7.1),

$$\eta = \frac{\text{area of hole}}{\text{area of disk}} \quad (7.1)$$

the velocity plots show that when η increases, i.e. the hole is made larger, the average velocity decreases. Compared with the wave velocity in circular disks, the average velocity changes very little for small values of η , i.e. a very small hole. It appears that there may be a threshold at which the size of the hole becomes a significant factor in the pulse velocity.

From Figs. 7.17 and 7.18, the fringe pattern becomes distorted because of the boundary effects produced by the hole. When the pulse was first entering a disk with a hole, and the contact load was still relatively small, the fringes appear Hertzian in shape(see Fig. 7.17, Frame 9). As the load increases, the fringe patterns show the boundary effects(see Fig. 7.16, Frame 13). Because of the boundary effects, Hertz contact equations cannot be used to analyze the data.

Fringe patterns in Figs. 7.17 and 7.18 show that a lot of energy remains in the disks after the main pulse has already passed through. Photoelastic experiments cannot be used to measure the wavelength exactly due to the limited field of view provided by the optical equipment.

7.4 Conclusions

The results indicate that:

- The contact profile has some effect on wave velocity and wavelength. But, the difference between the wave velocities for various geometries was only 10%. Therefore, more data are needed to make a conclusive statement.
- For the same contact profile, the incident direction of propagation does not appear to change the wavelength.
- The porosity of granular media changes the wave velocity. The wave velocity decreases as porosity increase.

Most importantly, the experiments that have been conducted in this area are in the preliminary stages and further study needs to be done to obtain any conclusive results.

Table 7.1 Geometric parameters for different particles used in the experiments.

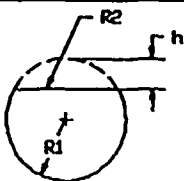
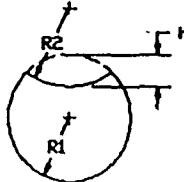
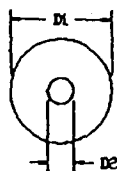
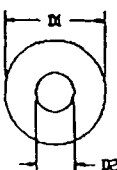
Group No.	Specimen Geometry	R1/D1 (inch)	R2/D2 (inch)	h (inch)
1		0.5	infinite	0.25
2		0.5	0.625	0.25
3		1	0.25	NA
4		1	0.365	NA

Table 7.2 Experimental result of wave velocity and wavelength for concave and flat particle

Chain NO.	1	2	3	4
Wavelength (mm)	90	88	77	78
Wave velocity (m s)	1140	1100	1010	1020

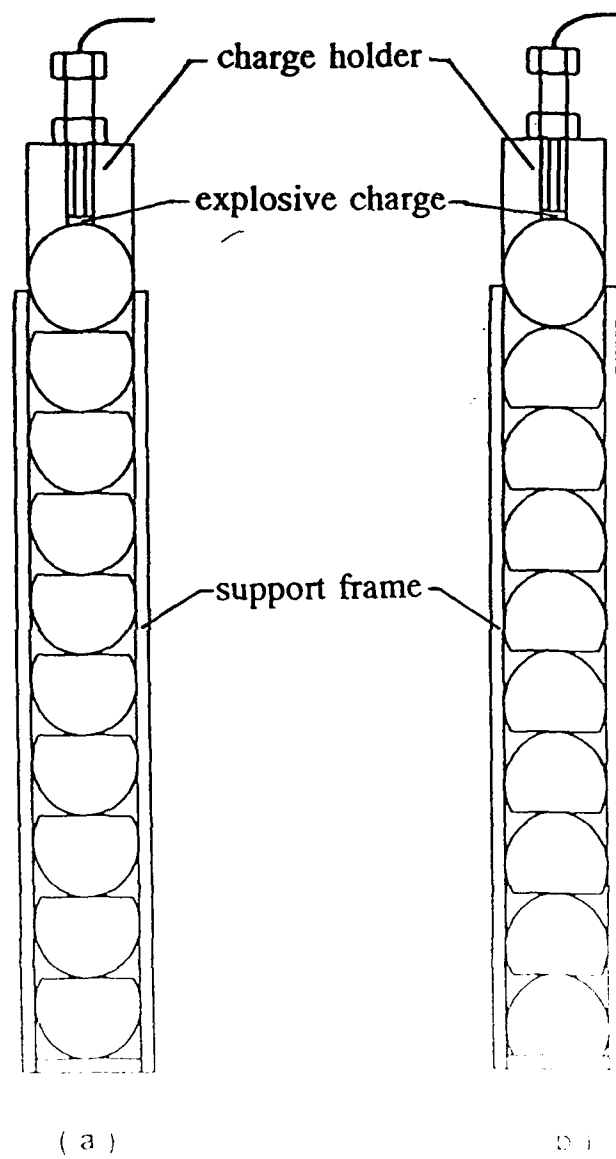


Fig 7.1 Experimental setup for angle chain assembly.

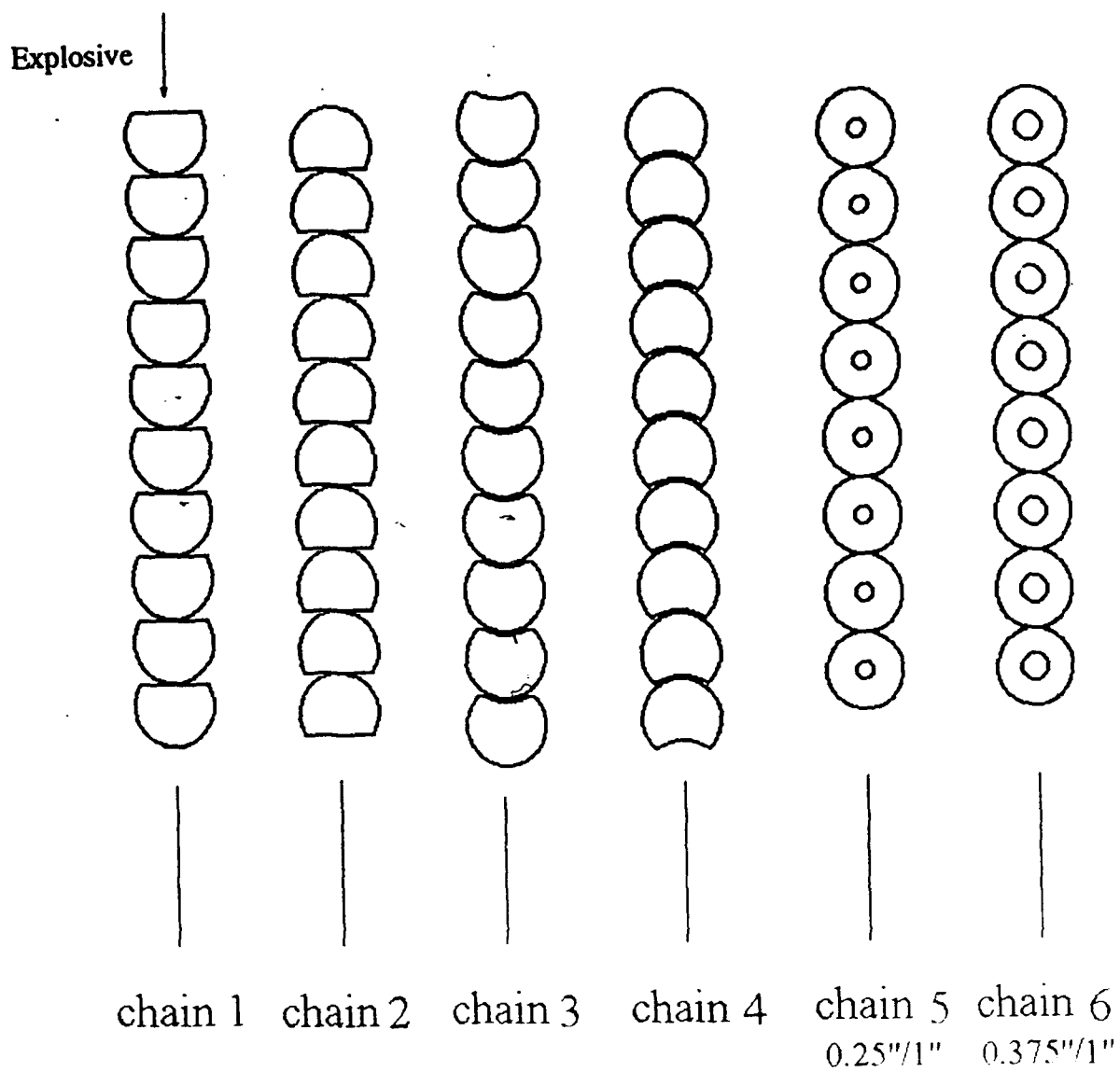


Fig.7.2 The six different single chain assemblies used in this study.

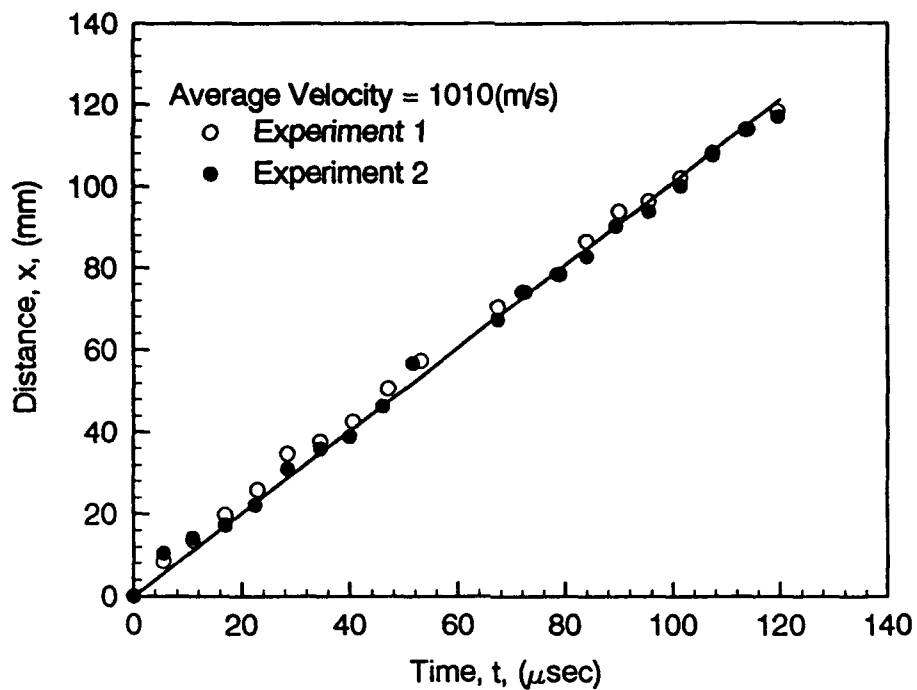


Fig.7.3 Wave propagation distance versus time for chain 1 in fig.7.2

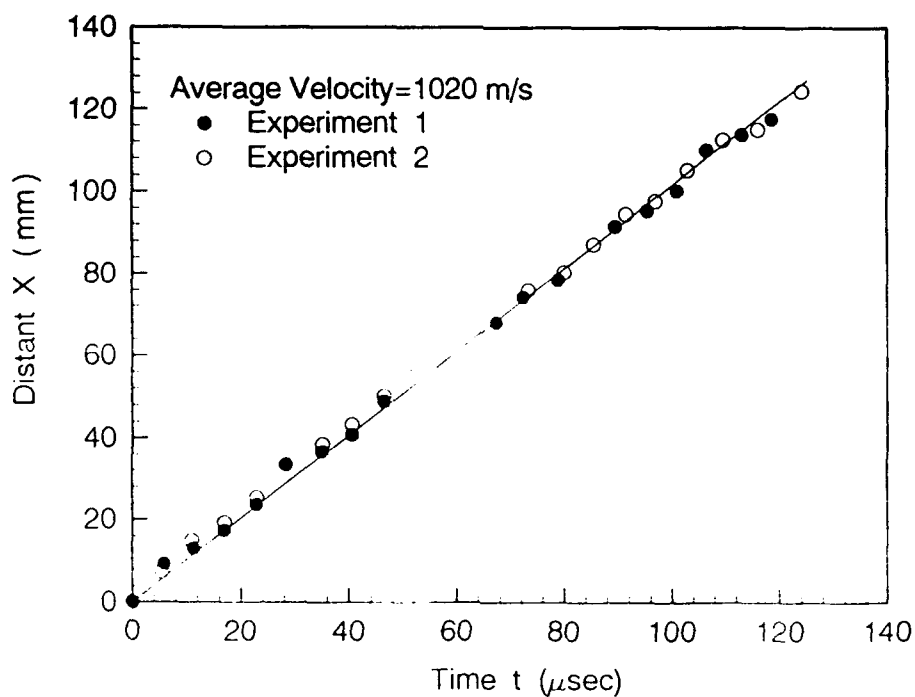


Fig.7.4 Wave propagation distance versus time for chain 2 in fig.7.2

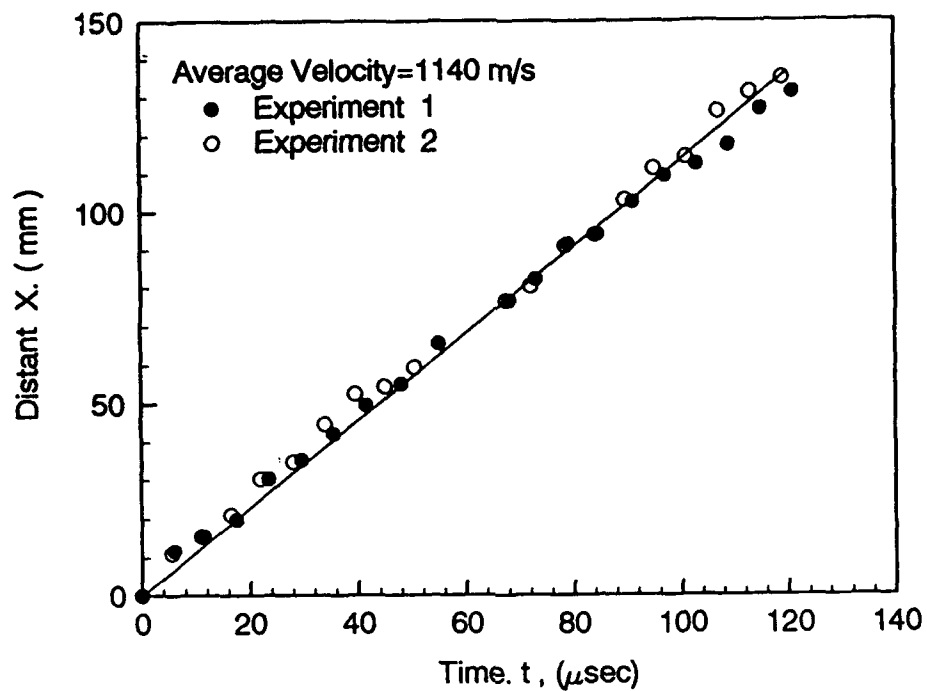


Fig.7.5 Wave propagation distance versus time for chain 3 in fig.7.2

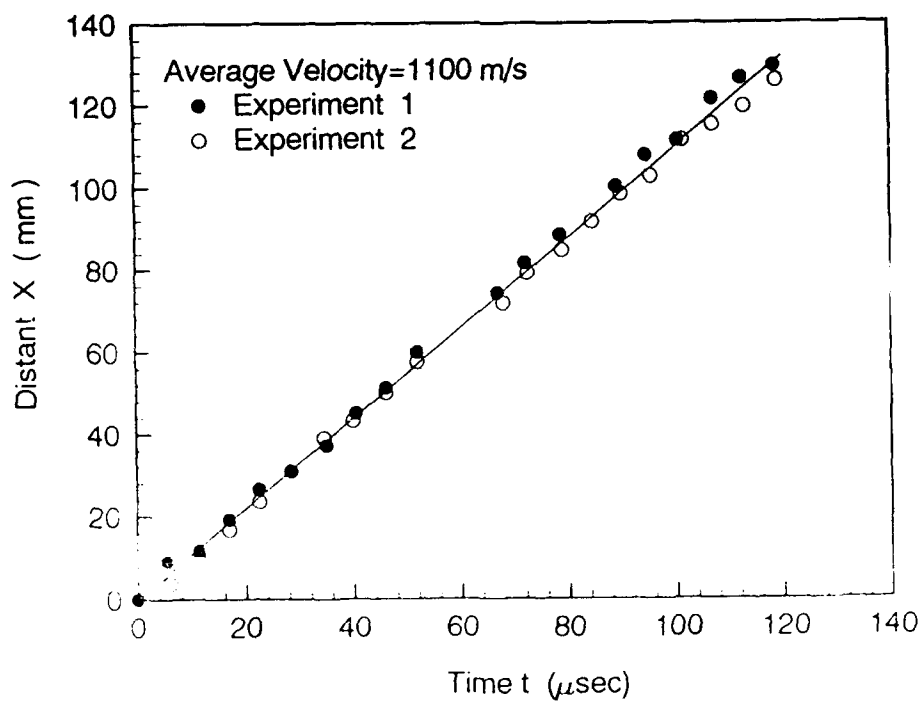


Fig.7.6 Wave propagation distance versus time for chain 4 in fig.7.2

Explosive

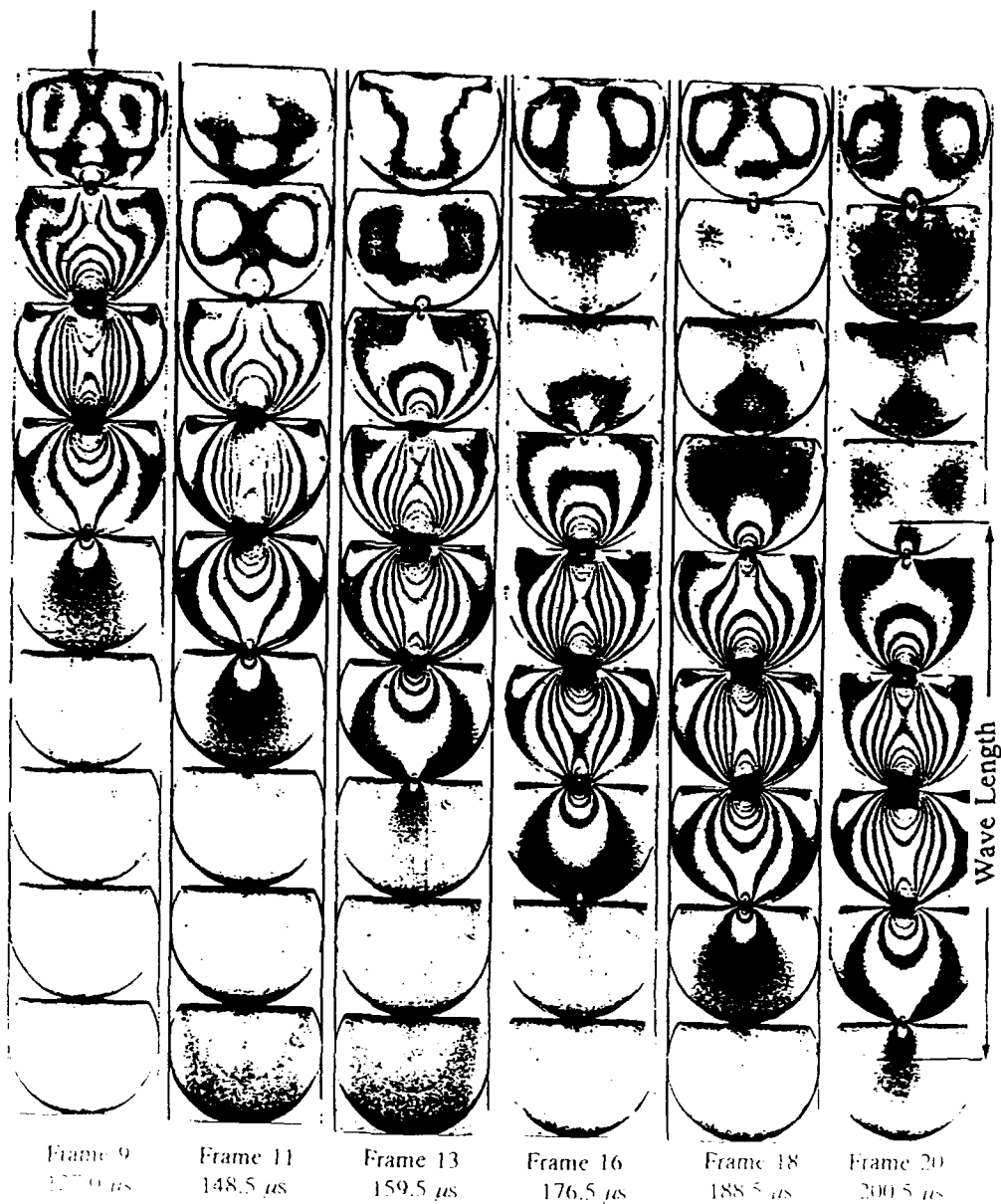


Fig 7.7 Typical schromatic fringes obtained for a single chain experiment conducted using chain 1 in fig.7.2

Explosive

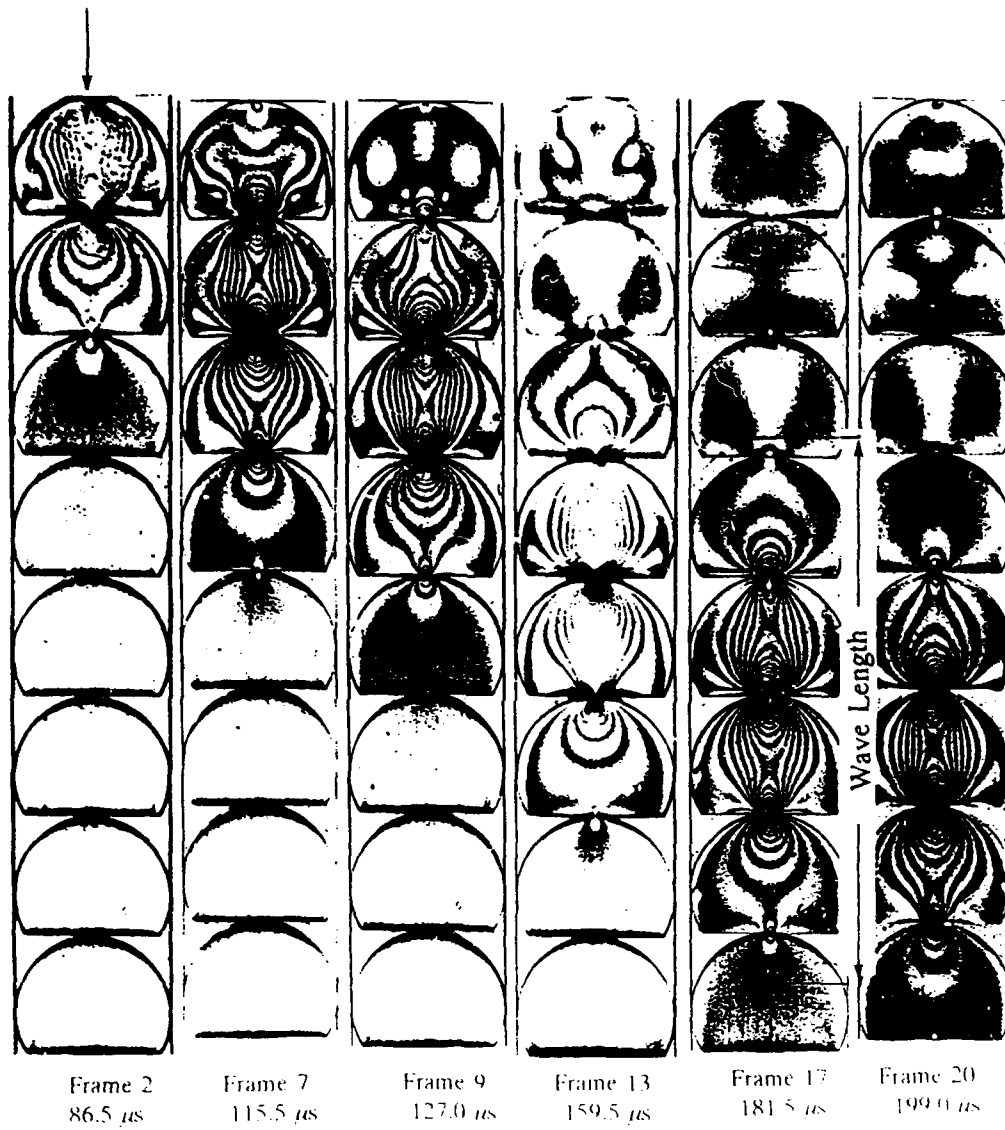


Fig.7.8 Typical isochromatic fringes obtained for a single chain experiment conducted using chain 2 fig.7.2

Explosive

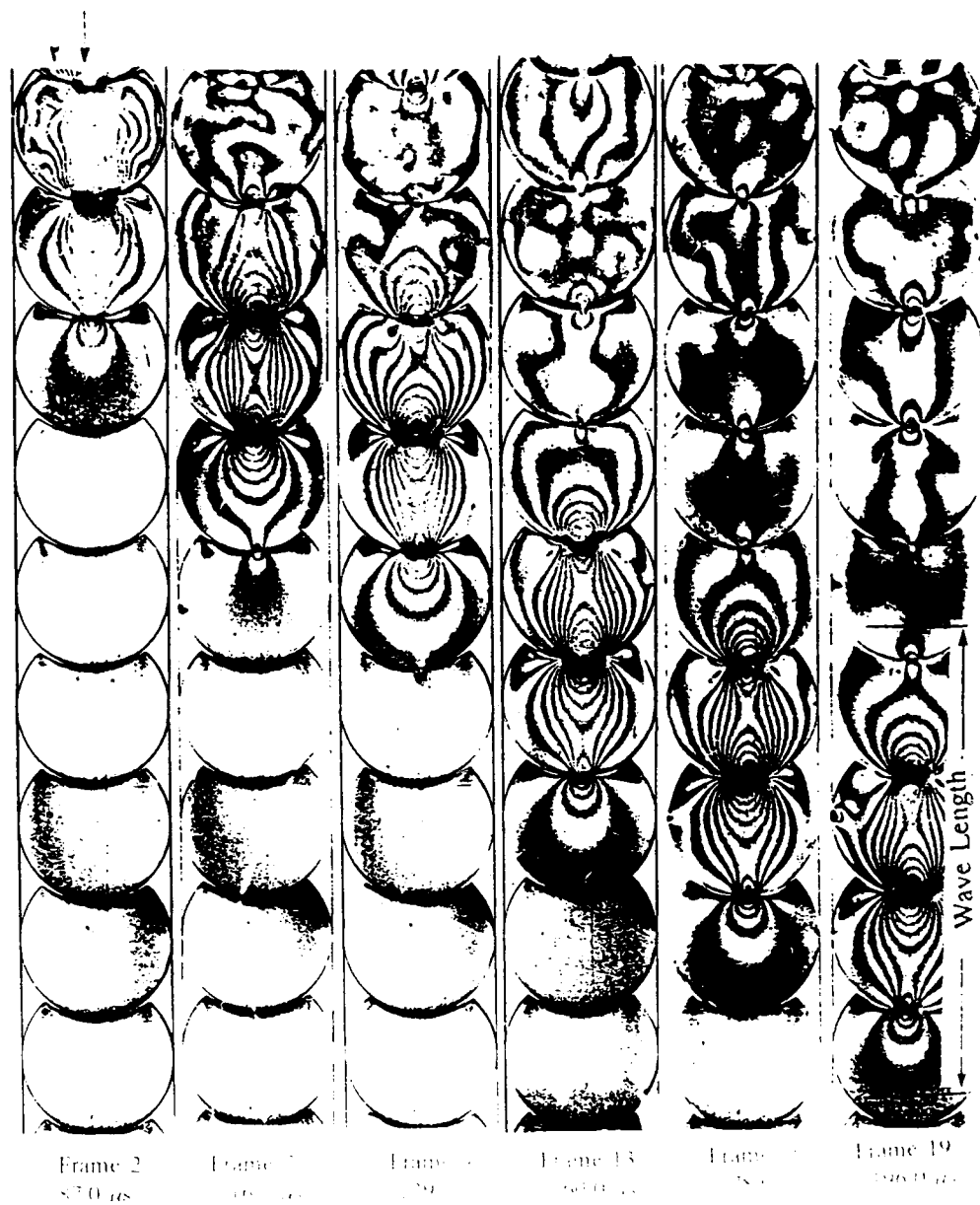


Fig.7.9 Typical isochromatic fringes obtained for a single chain experiment conducted using chain 3 fig.7.2

Explosive

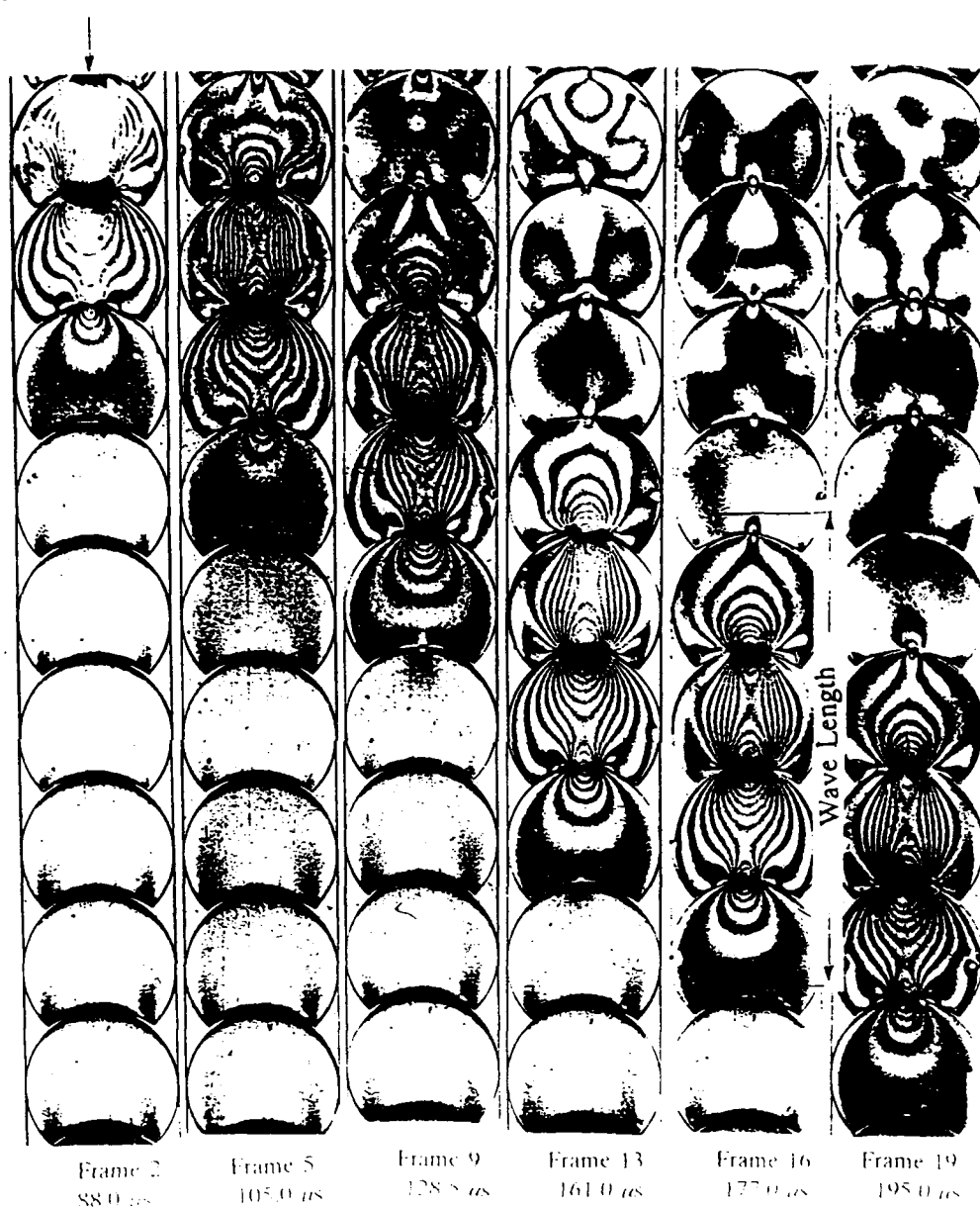


Fig.7.10 Typical isochromatic fringes obtained for a single chain experiment conducted using chain 4 fig.7.2

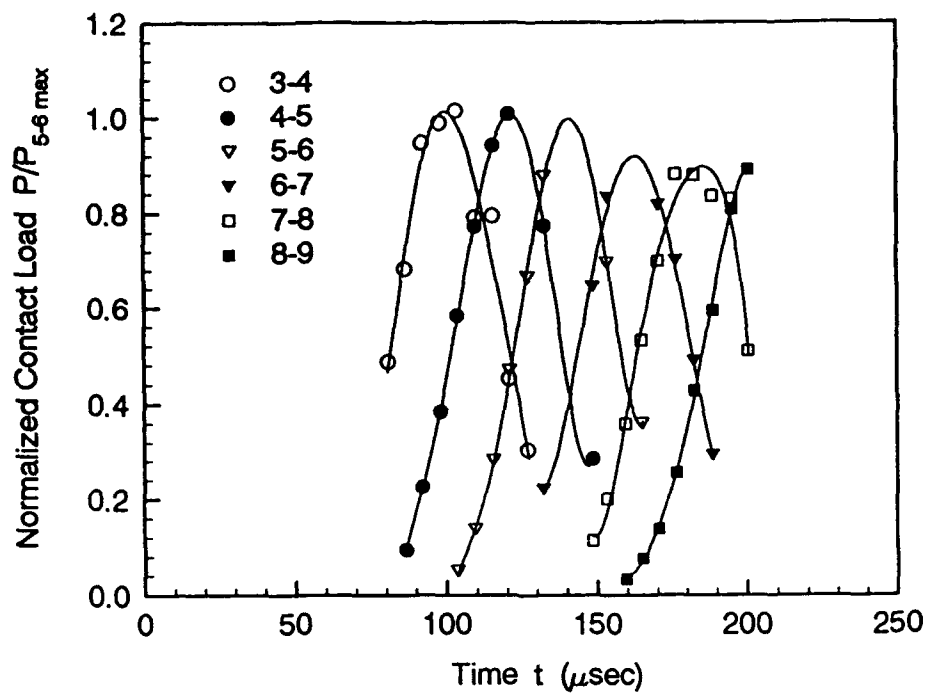


Fig.7.11 Normalized contact load as a function of time for chain 1 in fig.7.2

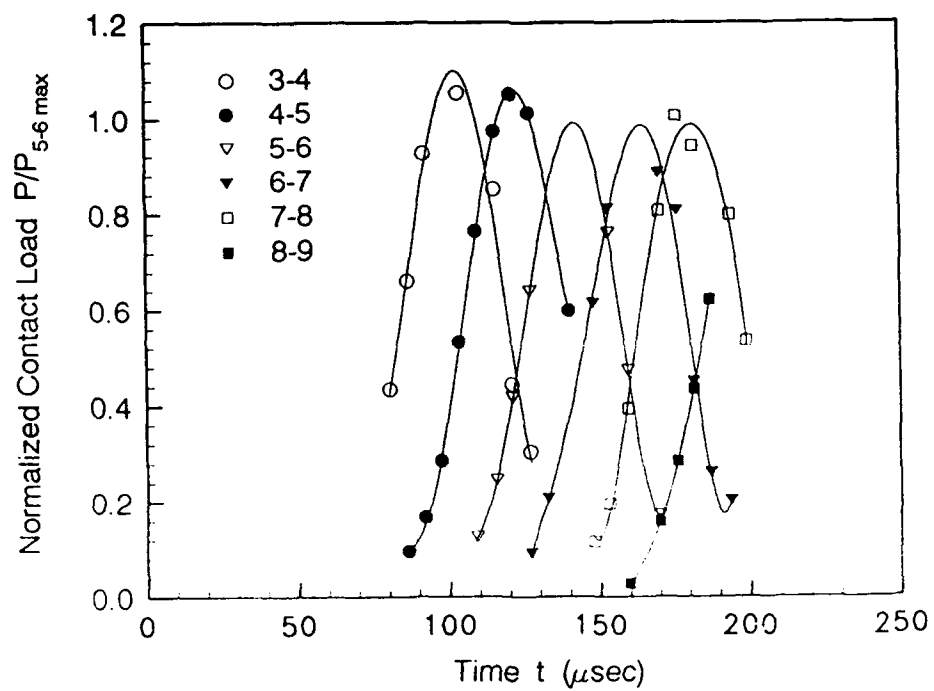


Fig.7.12 Normalized contact load as a function of time for chain 2 in fig.7.2

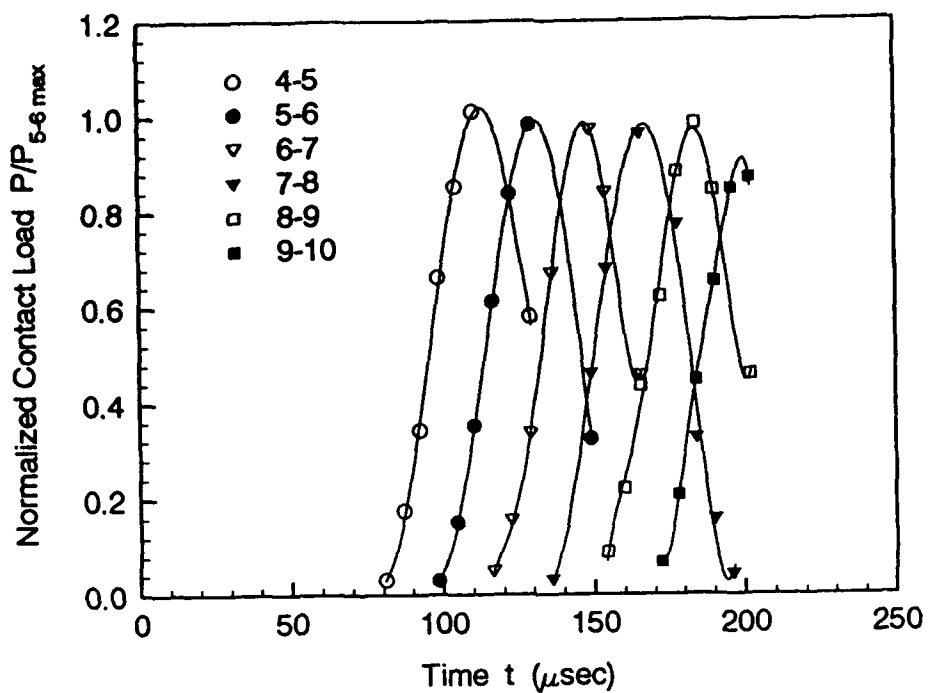


Fig.7.13 Normalized contact load as a function of time for chain 3 in fig.7.2

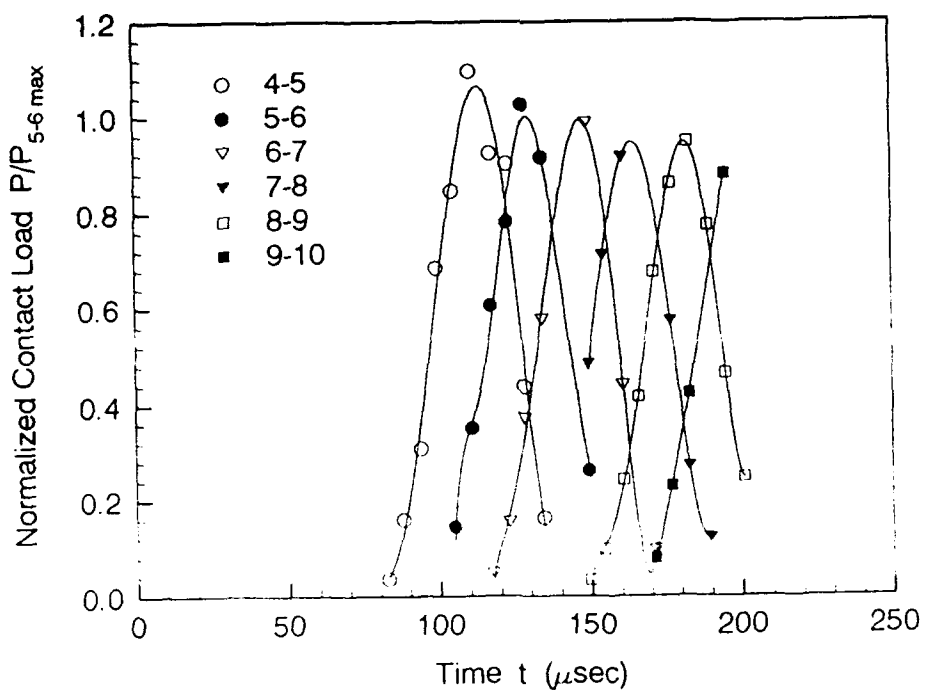


Fig.7.14 Normalized contact load as a function of time for chain 4 in fig.7.2

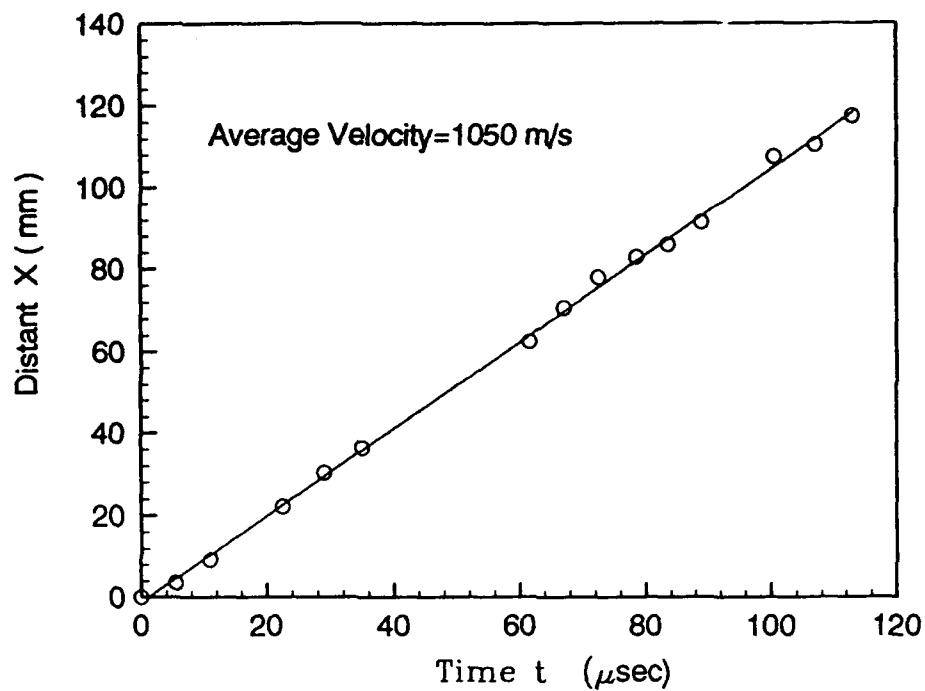


Fig.7.15 Wave propagation distance versus time for chain 5 in fig.7.2

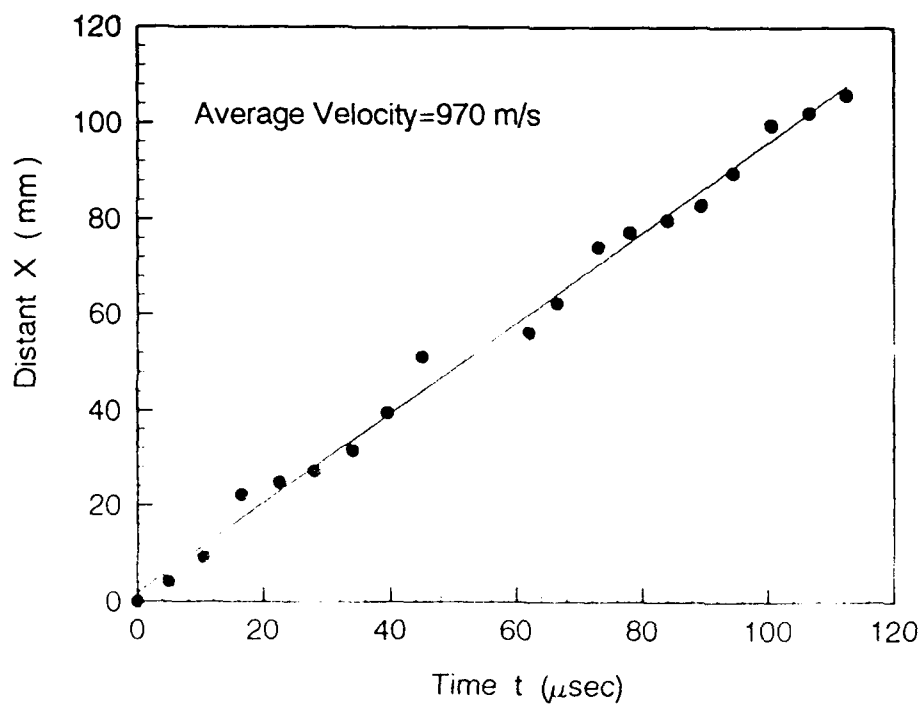


Fig.7.16 Wave propagation distance versus time for chain 6 in fig.7.2

Explosive

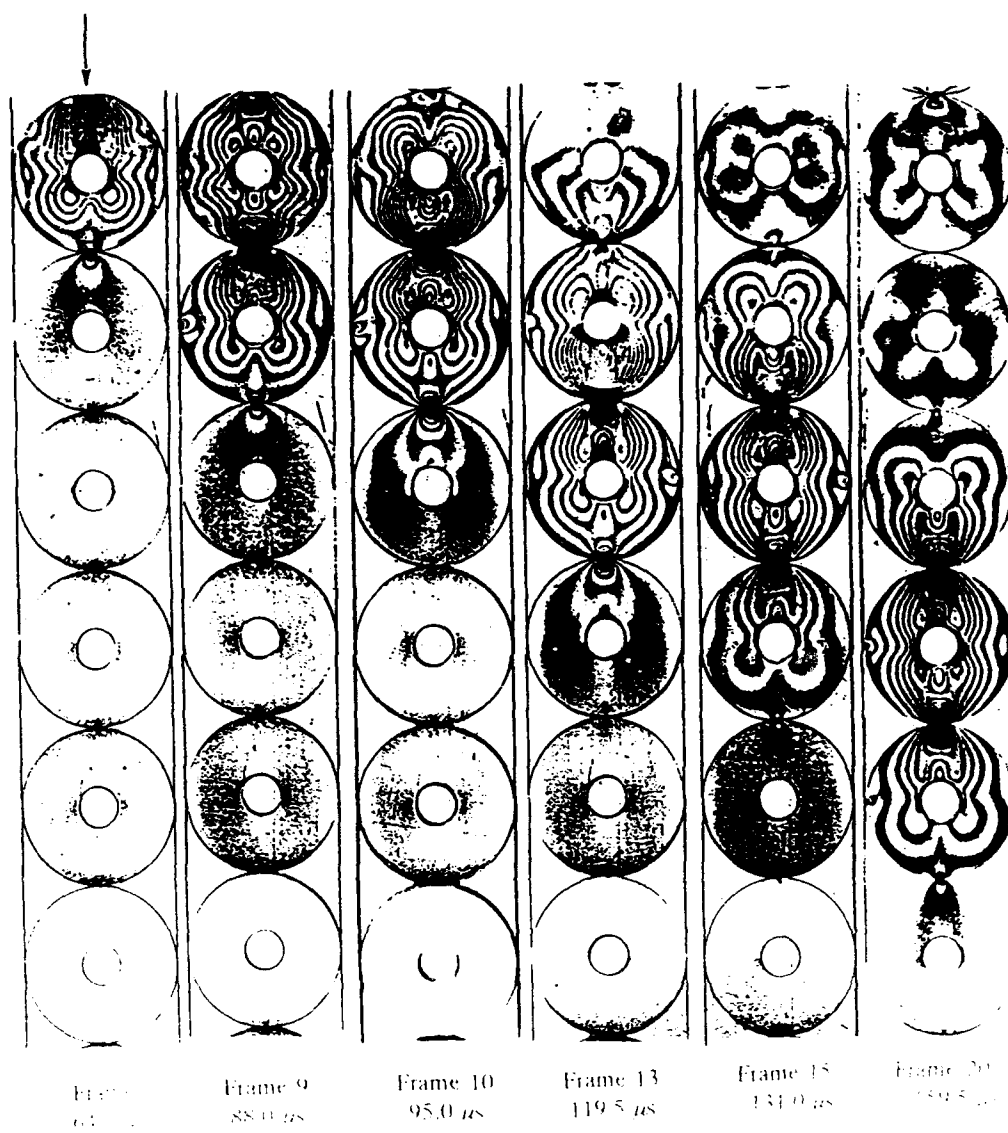


Fig 7.17 Isochromatic fringes obtained for a single chain experiment conducted using chain 5 in fig 7.2

Explosive

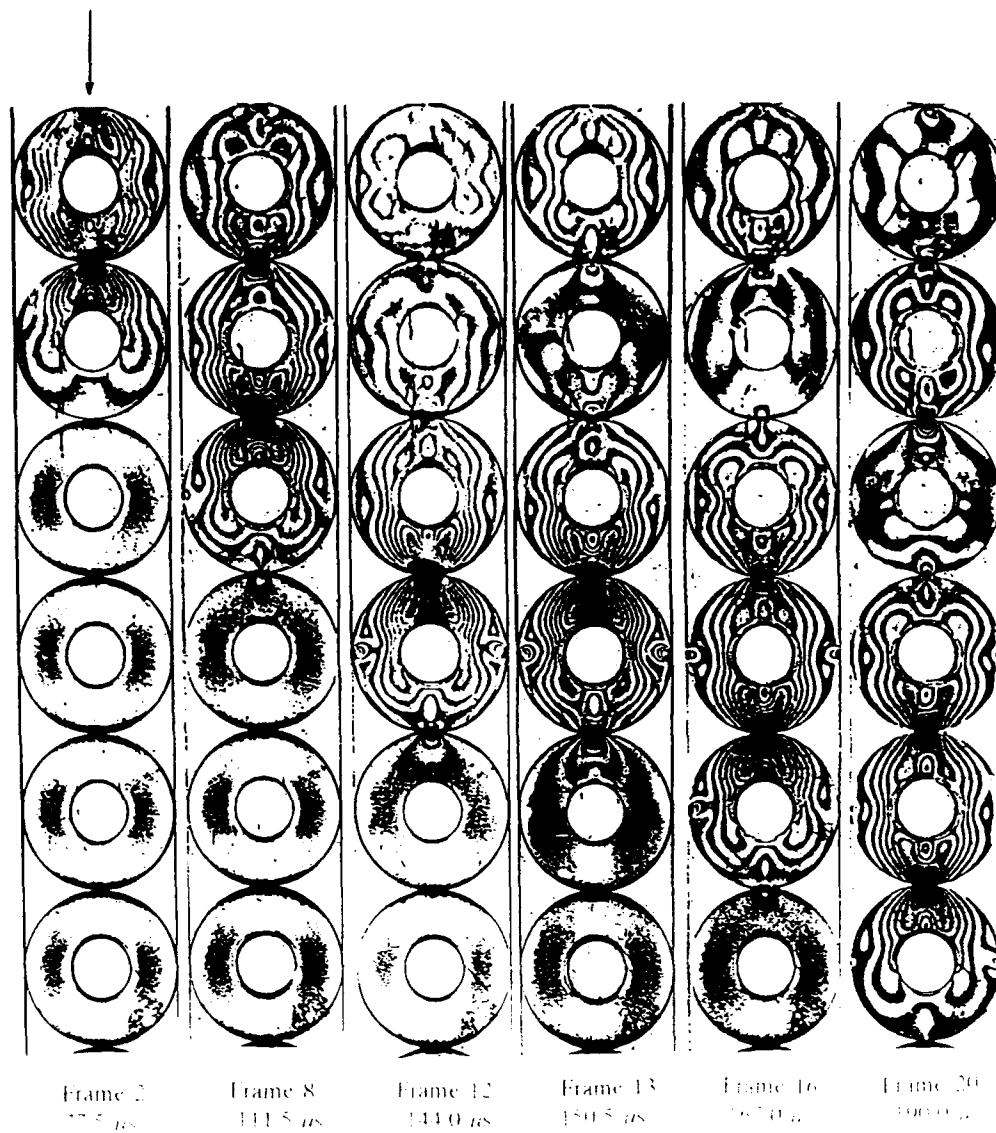


Fig 7 18 Typical isochromatic fringes obtained for a single chain experiment conducted using chain 6 in fig 7 2

Bibliography

Archbold, E and Ennos, A.E., 1972, "Displacement measurement from double exposure laser photographs", *Opt. Acta*, **19**, pp. 253-271.

Asundi, A. and Chiang, F. P., 1983, "Applications of white light speckle method to interior displacement measurement", *Journal of Strain Analysis*, **18**, pp. 23-26.

Asundi, A. and Chiang, F. P., 1982, "Theory and applications of the white light speckle method for strain analysis", *Optical Engineering*, **21**, pp. 570-580.

Barker, D. B. and Fourney, M. E., 1976, "Displacement measurements in the interior of 3-D bodies using scattered light speckle patterns", *Experimental Mechanics*, **16**, pp. 209-214.

Butter, C.D., Hocker, G.B., 1978, "Fiber optics strain gauge", *Appl. Opt.*, **17**, pp. 2867-2869.

Cameron, A., (1967) *The Principles of Lubrication*, John Wiley and Sons Inc., New York.

Chiang, F. P. and Asundi, A., 1979, "White light speckle method of experimental strain analysis", *Applied Optics*, **18**, pp. 409-411.

Chiang, F. P. and Asundi, A., 1980, "Interior displacement and strain measurement using white light speckles", *Applied Optics*, **19**, pp. 2254-2256.

Chiang, F. P. and Lu, H., 1990, "Surface and stress intensity factor measurement by a random speckle method", *International Journal of Fracture*, **43**, pp. 185-194.

Duffy, D.E., 1974, "Measurement of surface displacement normal to the line of sight", *Experimental Mechanics*, **14**, pp. 378-384.

Dvorkin, J., Mavko, G. and Nur A., 1991, The effect of cementation on the elastic properties of granular material, *Mechanics of Materials*, **12**, pp. 207 - 217.

Giallorenzi, T.G., Bucaro, J.A., Dandridge, A., Sigel, G.H., Jr., Cole, J.H., Rashleigh, S.C., and Priest, R.G., 1982, "Optical Fiber Sensor Technology", *IEEE Jour. of Quantum Elect.*, **QE-18**, no. 4, pp. 626-665.

Griffiths, R.W., 1991, "Fiber Optic Monitoring in the Electric Utility Power Plant Environment," *EPRI Conference Proceedings, Optical Sensing in Utility Applications*, San Francisco.

Gohar, R., 1988, *Elastohydrodynamics*, Ellis Horwood Limited, Chichester, England.

Kobayashi, A. S., 1987, "Handbook on experimental mechanics" Society for experimental mechanics. Inc., Prentice-Hall, Inc.

Konishi and Naruse 1988, "Microscopic model studies on the mechanical behavior of granular materials," *Proceedings of U.S.-Japan Seminar on Continuum Mechanical and Statistical Approaches in Mechanics of Granular Materials*.

Leendertz, J.A., 1970, "Interferometric displacement measurement on scattering surfaces utilizing speckle effect," *Journal of Physics, E: Sci. Instrum.*, **3**, pp. 214-218.

McCalla, T.R., 1967, *Introduction to Numerical Methods and FORTRAN Programming*, John Wiley & Sons, New York.

Murphy, K.A., Zimmerman, B.D., and Claus, R.O., 1989, "Embedded optical fiber sensors for internal material instruments", *Proc. Soc. Expt. Mech.*, pp. 752-756.

Narendran, N.A., Shukla, A., and Letcher, S.V., 1991, "Determination of Fracture Parameters Using Embedded Fiber-optic Sensors", *Exp. Mech.*, **31**, no. 4, pp. 360-365.

Narendran, N.A., Shukla, A., and Letcher, S.V., 1991, "Application of Fiber Optic Sensors to Fracture Mechanics Problems", *Eng. Fracture Mech.*, **38**, pp. 491-498.

Paikowsky, S.G., DiRocco, K.J., and Xi, F., 1993, Iterpartical Contact Force Analysis and Measurements Using Photoelastic Technology, 2nd International Conference on Discrete Element Methods (DEM), MIT, Cambridge, March 18-19, 1993.

Sadd, Martin H., *Elasticity Notes*

Sadd, M. H., Shukla, A., and Mei, H., 1989, "Computational and Experimental Modeling of Wave Propagation in Granular Materials," *Proc. of the 4th International Conference on Computational Methods and Experimental Measurements*, pp. 325-334, Capri, Italy.

Sadd, M. H., Shukla, A., Tai, Q. M., and Xu, Y., 1991, "Micromechanical Constitutive Behavior of Granular Media Under Dynamic Loading Conditions," *Proc. of the 3rd International Conference on Constitutive Laws for Engineering Materials: Theory and Application*, University of Arizona.

Sadd, M. H., Tai, Q. M., and Shukla, A., 1993, "Contact Law Effects on Wave Propagation in Particulate Media Using Distinct Element Modeling," *Intl. Journal of Nonlinear Mechanics*, Vol. 28, pp. 251-265.

Shukla, A. and Nigam, H., 1985, A numerical-Experimental Analysis of the Contact Stress Problem, *The Journal of Strain Analysis of Engineering Design*, Vol. 20, No. 4, pp. 241 - 245.

Shukla, A. and Sadd, M.H., 1992, "Wave propagation and dynamic load transfer due to

explosive loading in heterogenous granular media with microstructure", *AFOSR Final Annual Report*

Shukla, A., Zhu, C.Y. and Sadd, M., 1988, "Angular dependence of dynamic load transfer due to explosive loading in two dimensional granular aggregates," *Journal of Strain Analysis*, vol. 23, pp. 121-127.

Singer, J., 1964, *Elements of Numerical Analysis*, Academic Press, New York.

Thornton, C. and Barnes, D.J., 1982, "On the mechanics of granular material", *Proceedings of IUTAM Conference on Deformation and Failures of Granular Materials*, Delft, pp. 69-77

Timoshenko, S.P. and Goodier, J.N., 1970, *Theory of Elasticity*, McGraw-Hill, New York.

Wang, A., Murphy, K., May, R., Wang, G., Gollapudi, S., and Claus, R., 1992, "High temperature strain, temperature and damage sensors for advanced aerospace materials", *1st European Conf. on Smart Structures and Materials, Glasgow 1992*, session 4, pp. 127-130.

Xu, Y. and Shukla, A., 1993, "Evaluation of Static and Dynamic Contact Stresses in Simulated Granular Particles Using Strain Gages", *ASTM Jour. of Testing and Evaluation*, 21, no. 3, pp. 178-187.

Professional Personnel Associated with the Project

Faculty

Professor Arun Shukla

Professor Martin Sadd

Graduate Students

Raman Singh (PhD Candidate, Mechanical Engineering; non-US citizen)

Frank Sienkiewicz (PhD Student, Mechanical Engineering; US citizen)

Harry Zervas (PhD Candidate, Mechanical Engineering; US citizen)

Yan Zhu (PhD Student, Mechanical Engineering; non-US citizen)

Qiming Tai (PhD Candidate, Mechanical Engineering; non-US citizen)

Zhangmin Zhang (PhD Student, Mechanical Engineering; non-US citizen)

Adhikari Gautam (MS Student, Mechanical Engineering, non-US citizen)

Other

Tricia Evans (High School Minority Student, worked on the project in summer, under the Summer Youth Employment and Training Program)

Technical Publications

Xu, Yi and Shukla, A., "Evaluation of Static and Dynamic Contact Stresses in Simulated Granular Particles Using Strain Gages", *Journal of Testing and Evaluation*, pp 178-187, May 1993.

Shukla, A., Singh, R., and Zervas, H., "Dynamic Load Transfer in Cracked Particulate Aggregates A Dynamic Photoelastic Study", *Proceedings of Conference on Advanced Technology in Experimental Mechanics*, pp 125-130, July, 1993.

Shukla, A., Sadd, M., Singh, R., Tai, Q., and Vishwanathan, V., "Role of Particle Shape and Contact Profile on the Dynamic Response of Particulate Materials", *Journal of Lasers and Optics in Engineering*, Vol 19, pp. 99-119, 1993.

Singh, R., Shukla, A., and Zervas, H., "Dynamic Response of Damaged Particulate Media", *Proceedings SEM '93 Spring Conference*, pp 1119-1128, July, 1993.

Sadd, M., Tai, Q., and Shukla, A., "Contact Law Effects on Wave Propagation in Particulate Materials Using Distinct Element Modeling", *Int. Journal of Non-Linear Mechanics*, Vol 28, pp. 251-265, 1993.

Tai, Q.M. and Sadd, M., "On the Relationship of Fabric to Wave Propagation in Granular Materials", under preparation.

Sadd, M.H., Tai, Q.M., Silva A.J., and Veyera, G., "Discrete Element Modeling of Geoacoustic Wave Propagation in Saturated Granular Seabed Sediments", to be submitted to *Geo. Marine Letters*.

Sienkiewicz, F. and Shukla, A., "Evaluation of a Fiber Optic Sensor for Strain Measurement and an Application to Contact Mechanics," submitted to *Experimental Techniques*.

Interactions (Coupling Activities)

1. Some interaction has taken place with *Dr. C.T. Liu* of **Phillips Laboratory (AFMC)**, Edwards AFB in California regarding dynamic experiments with particulate materials and optical fiber technology in Experimental Mechanics.
2. We have interacted with the **Naval Underwater Warfare Center** at Newport, RI. *Mr. Harry Zervas*, a senior engineer at NUWC, is working on his doctorate on this project. He is a co-author on our papers on damaged particles.
3. Our work has been presented at the Fall Conference of the Society of Experimental Mechanics at Dearborn, Michigan; National Fracture Symposium at Lehigh, Pennsylvania; and International Conference on Advanced Technology in Experimental Mechanics in Japan.
4. *Dr. Jack Dvorkin* of **Stanford University's Department of Geophysics**, Stanford, California, visited our laboratory in October of 1993. During this visit, all of our students presented their work and these presentations were followed by extensive discussions. Arun Shukla met with Jack Dvorkin again in January of 1994 in California, and discussed the possibility of writing a joint paper on the dynamic response of cemented particles.
5. Arun Shukla, along with Professor A.J. Rosakis of the California Institute of Technology, organized a symposium on the Dynamic Failure of Modern Materials, in January of 1994. O. Walton from the Lawrence Livermore Lab, T. Ahrens from Caltech, W.L. Fourney from the University of Maryland, and J. Dvorkin from Stanford participated in the symposium. Several discussions on the

mechanics of particulate materials took place between A. Shukla and these researchers. The meeting was sponsored by the National Science Foundation and the Office of Naval Research.

6. Our research dealing with wave propagation in saturated granular and particulate systems has been of interest to a geomechanics research team at URI. This multi-disciplinary research group includes faculty from departments of civil, ocean and mechanical engineering. *Dr. Armand Silva* is head of the *Marine Geomechanics Laboratory*, and is the current leader of the *Geomechanics Research Group*. Current interaction activities include joint seminars and graduate student thesis committee work.
7. Some results of our preliminary studies of wave propagation in saturated granular media have been presented at the *American Geophysical Union - 1994 Ocean Sciences Meeting in San Diego*, California last February.